Methods to Assess Presence and Biological Impact of Engineered Nanoparticles

Charlie Corredor

A dissertation
submitted in partial fulfillment of the
requirements for the degree of

Doctor of Philosophy

University of Washington
2015

Reading Committee:
Jonathan D. Posner, Chair
Walter James Pfaendtner
Buddy D. Ratner

Program Authorized to Offer Degree:
Chemical Engineering

University of Washington

Abstract

Methods to Assess Presence and Biological Impact of Engineered Nanoparticles

Charlie Corredor

Chair of the Supervisory Committee:
Bryan T. McMinn Endowed Associate Professor Jonathan D. Posner
Department of Chemical Engineering

During the past two decades, the rates of development and production of engineered nanoparticles (ENPs) have rapidly increased due to their potential applications in medicine, cosmetics, energy, manufacturing, catalysis, food preservation, *etc.* However, the environmental fate and transport of ENPs remains poorly understood. This is partly due to the lack of accurate, simple and affordable methodologies for ENP detection and characterization. Scientists developing the new generation of nanotech-enabled consumer products have little information on the potential life cycle implications of their designs, leading to critical data gaps regarding possible ENPs exposures and hazards (*e.g.,* release rates, toxicity). The limitation in our current knowledge about the safety of ENPs creates tremendous uncertainty for industrial regulations and risk management. This dissertation presents a detailed description of methodologies aimed to (1) determine the biological impacts of ENPs on cell membranes, and (2) to screen for the presence of engineered nanoparticles in relevant complex biological and environmental samples.

In the first method, we use electrophysiological measurements of ENPs in suspended lipid bilayers to provide insights into the interactions of nanoparticles with cell membranes. The platform probes the responses of the lipid bilayer membranes to functionalized multi-walled carbon nanotubes, quantum dots, and a control organic compound, melittin, and shows that ENPs disrupt lipid membranes, which induces significant transmembrane current fluxes.

These findings suggest that ENPs can insert and traverse the lipid bilayer membrane, forming transmembrane channels that allow the transport of ions.

In the second method, we demonstrate a colorimetric detection assay that assesses the surface reactivity of ENPs, which can be used to detect the presence of nanoparticles in complex matrices. Current detection techniques require expensive and complex analytical instrumentation and are challenging to implement in biological fluids and environmental samples. This work addresses an emerging need for methodologies to accurately and quickly assess the presence and reactivity of nanoparticles in commercial, environmental, and biological samples. Our colorimetric assay can detect ENPs at parts per billion concentration levels by a direct measure of the ENP surface reactivity. We show that we can detect particles extracted from commercial products and show that our measurements correlate well with cellular toxicity responses. The development of sensitive, simple, and affordable techniques to detect ENPs in environmental and biological samples will ultimately aid in understanding the health risk of ENPs exposure, design of safe nanoproducts, and advancement of nanomedicine.

Research Goals. The primary goal of this dissertation is to develop and use methodologies to assess for the presence and biological impacts of ENPs. To accomplish this goal, I address the following objectives: (*i*) understand the mechanisms, physicochemical properties, and conditions under which ENPs interact with suspended phospholipid membranes, (*ii*) examine and extract quantitative values for the interaction of ENPs - lipid membranes that captures the ion migration effect induced by particles of different shapes and size as well as at particle mass concentrations, (*iii*) employ surface catalytic redox properties of ENPs as a surrogate approach to develop a colorimetric detection platform that evaluates the presence or absence of nanoparticles, (*iv*) determine the physicochemical properties of ENPs (*i.e.,* radii, surface coatings, compositions, *etc*) that enhance or impede the colorimetric detection in biological and environmental relevant matrices, and (*v*) evaluate the potential applicability of the colorimetric assay to detect nanoparticles extracted from commercial products as well as the correlation of ENP surface catalytic measurements with toxicity responses in bacterial systems.

Research Impact. Successful completion of this research resulted in the development of a sensitive, simple, and affordable methodology to accurately assess the presence/absence of ENPs as well as improve the understanding of biological impacts of ENPs in cell membranes. The experimental observations presented in this dissertation aid in the future design and commercialization of new portable methodologies for detecting ENPs in medical applications (nanomedicine), quality control technology for ENP based commercial products, toxicological studies, and sensing of ENPs in drinking waters and food products.

Acknowledgements

Throughout my academic and personal life, I have and continue to benefit from numerous interactions with family, friends, colleagues, and mentors, and it is my great pleasure to acknowledge them here.

A good advisor will go beyond the standard requirements by helping students to gain research identity, assist them to figure out where they fit in the field, and obtain the confidence that they need to move beyond graduate school. This is the reason why I feel honor to thank first my advisor and committee chair Professor Jonathan D. Posner. He has been an outstanding advisor throughout my years as a graduate student. He continuously encouraged me to not only grow as a scientist and engineer but also as an independent thinker. I am not sure many graduate students are given this opportunity to develop their own individuality and self-sufficiency by being allowed to work with such independence. For everything you have done for me, Prof. Posner, I thank you. His critical thinking, enthusiasm, and passion for science will always inspire me moving forward. Also, I would like to thank Prof. Buddy Ratner, Prof. Terrance J. Kavanagh, and Prof. Jim Pfaendtner for agreeing to be part of my graduate committee as well as for all their suggestions and insightful discussions that enhanced the quality of the work presented here.

There is no doubt in my mind that this journey would not have been near as rewarding if not for the fellowship that I received from all my labmates at the Posner Research Group, Kamil Salloum, Philip Wheat, Steven Klein, Jeffrey Moran, Nathan Marine, Wen-Che Hou, William Walker, Jay Wolfer, Kelly Connelly, Eric Mooers, Kevin Kimura, Jianzhu Yin, Karl Kerr, Andrew Bender, Amanda Levenson, Stefan Foulstone, Mark D. Borysiak, and Babak Y. Moghadam. I am deeply thankful for all your support, collaboration, discussions, and most importantly for keeping up with me during these years. I will never forget the time when Babak, Mark, and I participated in the 2015 business plan competition and we took home the grand prize–this was a great learning experience and make us see how we can translate our scientific findings into tangible applications/products. Additionally, I would like to thank

Babak, who has been an excellent friend throughout all these year of my graduate school; making this journey an incredible experience. Babak and Mark were always willing to help and provide their best possible advise–thank you guys.

There have been other people who helped and mentored me along the way during my studies, Prof. John R. Lombardi who was the first person to introduced me to the scientific method, gave me all the personal and academic guidance that I needed at the early stages of my academic career as well as provided me with the opportunity to explore my intellectual curiosity in his lab. Prof. Ilona Kretzschmar an excellent mentor and friend who always was willing to chat and gave me her unconditional support. Prof. Claude Brathwaite for his critical insights and for seeing in me a future scientist. Prof. Ron Birke for educated me in the basic principals of thermodynamics. Dr. Marco Leona for his great support and guidance during my research at the Metropolitan Museum of Art–he always made science look stylish and sophisticated, Prof. John Berg for his insightful discussions about colloidal science during lunches and Prof. Kyle Doudrick for our conversations about dyes. Christine O'brien and Pamela Tyler from the National Academy of Sciences for their unconditional support during my graduate studies. The Sanchez family for all their support and guidance during the early stages of my life.

In addition, I would like express my sincere gratitude and appreciation to Prof. Paul Westerhoff from Arizona State University for all the great support and guidance during my graduate studies. He always made time for questions, bounce ideas, and his insightful opinions without fail strengthen the overall quality of my research projects.

To my mother who has more strength than most, my sister who's passion is unchangeable, and my father for all his advise – I will always be thankful. My life in graduate school was not always an easy or smooth endeavor, but their support was energizing and motivating during these times. Mom, thank you for everything, I would not be here without your support and guidance. You are my rock and always keep me grounded.

Last but certainly not least, I must thank a certain someone who embarked on this journey with me five years ago. Keilys your love, patient, and unconditional support have been one of my strongest motivators, and for it I will always be indebted. I can not wait to see where the future will take us.

The work presented in this dissertation was generously supported by the Ford Foundation Fellowship administered by the National Academies of Sciences and by the National Science Foundation Graduate Research Fellowship under grants DGE-0718124 and DEG-1256082.

Finally, to all of them that I did not mentioned here but have impacted my life,

Thank you!.

Citations to Previously Published Work

Portions of this dissertation have appeared in the following published articles:

Chapters 2

C.Corredor, W. Hou, S. Klein, B. Moghadam, M. Goryll, K. Doudrick, P. Westerhoff, J. D. Posner. Disruption of model cell membranes by carbon nanotubes. *Carbon* 2013, Vol. 60, 67-75.

Chapters 3

C. Corredor, M. Borysiak, J. Wolfer, P. Westerhoff, J. D. Posner. Colorimetric Detection of Catalytic Reactivity of Nanoparticles in Complex Matrices. *Environ. Sci. Technol* 2015, 49 (6), pp 3611-3618

Dedication

To those who encouraged me and believed in me during this process

Contents

List of Tables

List of Figures

Chapter 1

Introduction

1.1 Abstract

Engineered nanoparticles (ENPs) can be found in over 1800 commercial products. Cosmetics, pharmaceuticals, sunscreens, energy storage devices, automobile catalysts, electronics, and food packaging are only few examples of products containing nano-sized particles. Generally, the goal of adding nanoparticles to consumer goods is to improve quality, increase durability, and reduce the manufacturing cost. Multiple research groups are developing the next generation of nanomaterials, but the environmental and human impact of these engineered materials is still unknown. Current tools to characterize ENPs are complicated, expensive, and do not work well with environmental or biological samples, which make the assessment of nanoparticles a challenging task. It is necessary to evaluate the hazards connected with the exposure of nano-sized materials and to understand the biological impacts of ENPs to prevent future side effects associated with the use of these materials. To improve the understanding of ENPs' potential side effects, it is necessary to develop reliable, sensitive, and accurate methodologies specific to nanoparticles properties using low-cost and portable instrumentation. These tools will inform human exposures assessments, monitor

ENPs in health-based research studies, and evaluate how these nanoparticles interact with biological systems.

1.2 Background

In 1974, the word "*nanotechnology*" was first used by Norio Taniguchi when he described a semiconductor process with nanometer precision.[1] Since then, the term nanotechnology has been employed to describe the manipulation of matter on a near atomic scale to produce new materials and structures. Approximately ten years later, nanotechnology obtained a refined definition that refers to the fabrication, use, manipulation, control and characterization of structures, devices, or materials with a least one dimension in the size range of 1 - 100 nanometers.[2, 3]

Nanomaterials include nanofilms and sheets (5 - 100 nm in one dimension), nanotubes and wires (5 - 100 nm in two dimensions) and nanoparticles (5 - 100 nm in three dimensions).[4, 5, 6, 7, 8] Nanoparticles can occur naturally (*e.g.,* ashes, soil particles, biomolecules–including DNA with a diameter of around 2.5 nm, viruses (10 to 60 nm) and bacteria (30 nm to 10 μm), desert sand, oil fumes, smog, and fumes originating from volcanic activity or forest fires), be produced unintentionally from byproducts of human activities (*e.g.,* diesel exhaust, paper production, mining, industrial blast furnace emissions, and welding fumes), or be intentionally manufactured as engineered nanoparticles (ENPs) that are specifically designed and deliberately synthesized by humans.[9] In this dissertation, the term ENPs will be used to describe particles having a fine nanometric-dimension structure (*e.g.,* 1 to 100 nm), synthesized intentionally with an objective of potential commercial use and manufacturing. Figure 1.1 presents a brief summary of the permutations and combinations relating to different types of nanoparticles and their potential applications.

Due to their size, nanoparticles show different physicochemical properties compared to their respective bulk material. These include changes in optical properties, material strength,

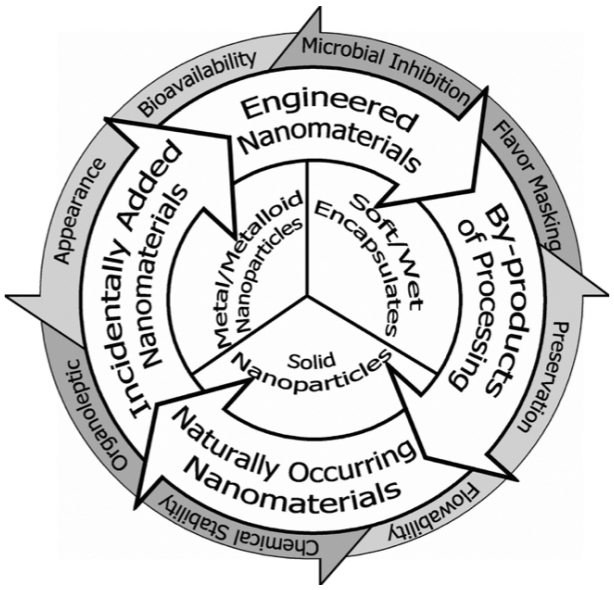

Figure 1.1: Schematic demonstrating the permutations and combinations relating the types of nanoparticles to the end applications.[10] The inner core represents the three main classifications of nanoparticles. The next wheel shows possible production schemes of nanoparticles and the outer wheel represents some potential applications of the different classes of nanoparticles.

solubility, conductivity, thermal behavior, and catalytic activity.[4, 5, 11, 12] One of the most significant properties of nanoparticles is the high surface-to-volume ratio compared to their bulk counterparts.[13] Since most chemical reactions take place at the surface of a material; the greater the surface for the same volume, the greater the number of catalytically active sites.[14] These unique properties make ENPs a potential material to improve a large number of existing consumer and industrial products.

During the past two decades, the development of ENPs have rapidly increased due to their applications ranging from medicine, cosmetics, energy, manufacturing, catalysis, to food preservation, as shown in Figure 1.2A.[15, 16, 17, 18, 19, 20, 21] Research and development of nanoscale technologies is continuously growing and it is expected that by 2025 nanotechnology applications will affect nearly every type of manufactured product, creating an industry of $2.6 trillion dollars.[22, 23, 24] Figure 1.2B shows the number of commercially available nano-enabled products in the market as a function of time. As more nanoproducts reach commercialization, there is a need to anticipate, understand, and manage both poten-

tially positive and negative side effects that might result from ENPs' consumption, exposure, or resale.[25, 26, 10]

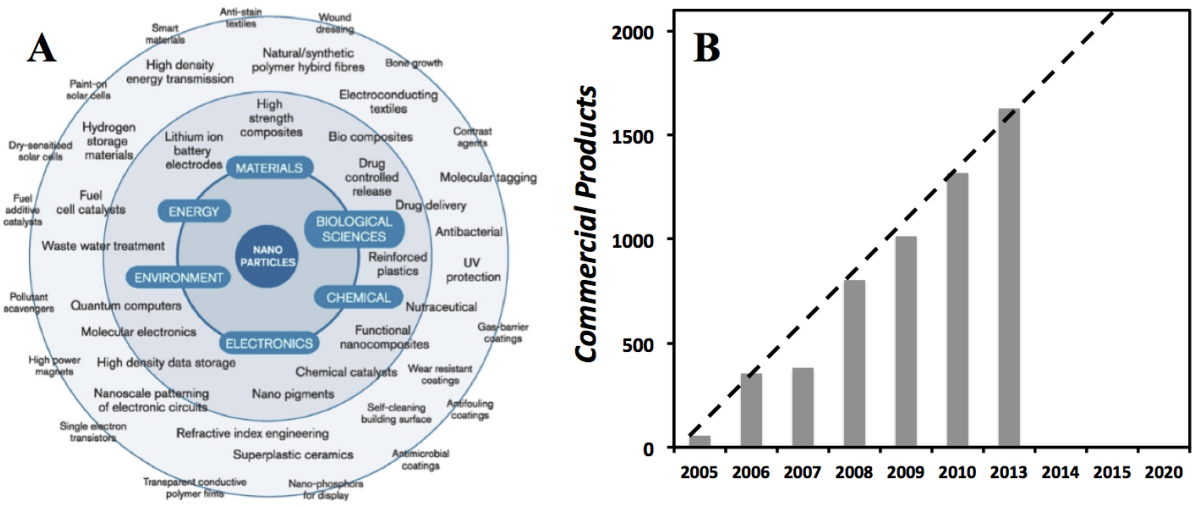

Figure 1.2: Nanotechnology applications by industrial sectors (A) [27] and number of nano-enable commercial products available in the market as a function of time (B) [28].

At the global scale, people are increasingly exposed to ENPs. For example, as ENPs enter drinking water supplies through contamination by upstream pollution sources might create a direct risk to humans. Similarly, unintentional ENP exposure can be attained through the use of nanomaterials in water remediation technologies (*e.g.,*TiO_2 photocatalyst, zerovalent iron reductants), diesel emission sources (*e.g.,* cerium additives in fuel), food additives (*e.g.,* silver as antibacterial, silica dioxide for texture), clothing (*e.g.,* TiO_2 for self cleaning, silver as antibacterial), medical treatments (*e.g.,* silica or gold for drug delivery, quantum dots or iron for imaging, gold for biosensors, zinc or TiO_2 for skin protection), industrial processes (*e.g.,* silica for polishing processes), unplan workplace exposure, among many other potential applications.[29, 30, 31, 32, 33, 34, 35, 36, 37, 38] ENPs can also be introduced to humans intravenously (usually purposefully), and through inhalation, ingestion, or absorption through the skin, as presented in Figure 1.3. Once the internalization of ENPs takes place, the blood can transport them throughout the circulatory system due to their small size where they can react or accumulate.[39] With the large number of nano-enabled technologies that will exist

in the near future, the scientific community expects that humans will be exposed to ENPs and recognizes the need to identify and manage potential hazards. As ENP production increases governmental agencies are forced to rapid develop models to understand how ENPs interact with biological systems – if we want to prevent future exposure risk.

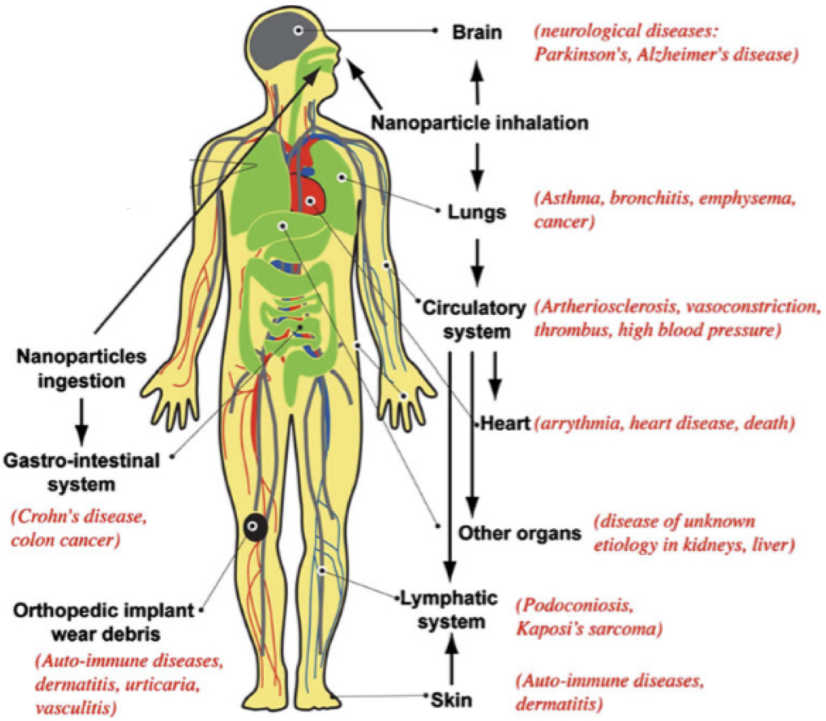

Figure 1.3: Schematics of human body with potential pathways of ENPs exposure, affected organs, and associated diseases.[40]

1.3 Motivation: Engineered Nanoparticles' Environmental and Health Risks

Due to the widespread use of ENPs, it is anticipated that nanoparticles will come into contact with humans, in manufacturing facilities (*i.e.,* the workplace) and from consumer products.[15, 41, 42, 43, 44] Several research groups showed toxicological correlations between particle physicochemical properties, such as size, shape, concentration, and capping agents,

also thier biological responses that led to cytotoxicity.[45, 46, 29] Although some studies suggest that ENPs can impact a wide variety of biological platforms, the toxicity of ENPs and their effects on human health, as well as their environmental fate and impact in water and soil, is still widely unknown.[11] Recent reports show that different types of ENPs can cause cytotoxicity, cross cellular layers, and accumulate in tissues.[43, 47, 48, 49, 50, 51, 52, 53] Further toxicity studies showed that fullerenes, Al, and TiO_2 ENPs create stress to a wide range of aquatic organisms (*e.g.,* Daphnia magna, zebra fish, large mouth bass) that lead to mortality.[54, 55, 56, 57] Table 1.1 presents a brief summary of recent ENPs toxicity investigations showing a wide range of nanomaterials interacting with biological systems, creating stress, and ultimately mortality.

Table 1.1: Engineered nanoparticle toxicity studies showing that ENPs interact with biological systems.

Study	ENP Type	Reference
In vitro cytotoxicity of oxide nanoparticles	SiO_2, Fe_2O_3, TiO_2, ZnO, $Ca_3(PO_4)_2$, CeO_2, ZrO_2	[47]
Tissue uptake of C_{60}	C_{60}	[58]
Cytotoxicity of quantum dots	CdSe quantum dots	[59, 60]
Transport of surface modified ENPs through cell membranes	peptide and amino ENP	[61]
Manufactured nanomaterials induce oxidative stress in the brain of bass	C_{60}	[54]
Daphnia magna mortality when exposed to ENPs	C_{60}, TiO_2	[57]
Deleterious effect of nanoparticles in adult zebrafish	Ag	[62]
Phytotoxicity of alumina ENPs	Al	[56]

Even in cases where ENPs do not show any acute toxicity, questions regarding the long term effects, bioaccumulation and the environmental impact remain unanswered.[4] Engineered nanoparticles may also affect the toxicity of other substances, since natural nanomaterials are known to act as vectors to common contaminants.[63, 64] For example, Zhang *et al.* showed that cadmium bioaccumulation, a common toxic pollutant, is enhanced in the presence of TiO_2 nanoparticles.[65] It is crucial that we begin to understand the behavior of ENPs in biological systems and in environmental matrices, as well as their potential toxicity to humans.

Studies have reported that nano-sized particles (but not their macro or micro counterparts) can accumulate in cells and aquatic organisms and lead to stress and mortality.[66,

67, 61, 53, 47, 48, 68, 69, 70, 71] These results highlight the need for caution during the use and disposal of such manufactured nanomaterials to prevent unintended health and environmental impacts. ENPs present new challenges to understanding, predicting, and managing potential health risks and environmental impacts. As materials with ENPs are being developed and put on the market, scientific data on the health effects is unavailable, which leads to a lack of governmental and industrial regulations. The risk of a certain new nanomaterials should be evaluated with consideration for their application, use, and final disposal. For instance, ENPs used in coatings could be virtually non-toxic due to their composition, size and morphology, but large customer exposures, might create unintentional hazards.[72, 73] The limitations in our current knowledge about the environmental fate and transport of ENPs is partly due to the lack of simple and affordable methodology for their detection and characterization in complex samples such as waste waters, lakes, oceans, foods, biological fluids, and tissues.

1.4 Characterization Methodologies and Limitations

To determine if ENPs or products manufactured with nanotechnology have any potential health or environmental effects (*e.g.,* transport, fate, interaction with living organisms) a number of physical and chemical parameters need to be determined. These include size and shape, state of dispersion, dissolution, concentration, catalytic activity, surface area, surface chemistry, among other physicochemical characteristics that can provide insights on potential health and environmental risks.[74, 75] For example, size, shape and morphology are some characteristics that correlate with cytotoxicity responses of ENPs, such as inflammation and tissue perforation.[76, 77] However, the way in which ENPs interact with the organisms or the environment depends mainly on the surface area, particle reactivity, and surface chemistry, which determine the material's dispersion and adsorption. This indicates that both physical

and chemical characteristics of ENPs, as well as suspension media should be considered when it comes to determining ENP handling and disposal.[54, 75]

Nanoparticles, when released to the environment and exposed to biological medium, undergo physical and chemical transformations which further complicate detection, characterization, and risk assessment.[78, 79, 80] Analytical techniques to characterize ENPs include microscopy, chromatography, centrifugation, mass or light spectroscopy, electrophoretic mobility measurements, and thermo analysis.[41, 36, 81, 82, 83] However, many of these current analytical methods require highly trained personnel to operate, expensive instrumentation, and require time consuming sample preparation and fixation that may disturb the state of particles as they existed in the environmental and biological samples. Furthermore, existing techniques usually measure mass concentrations and/or sizes, rather than the unique properties (*e.g.,* catalytic, optical, surface plasmon resonance, surface area) of ENPs that are often engineered into products, and which regulators or scientist believe might have adverse health or environmental impacts. Unlike dissolved inorganic and organic chemicals where a wide spectrum of analytical techniques already exist (*e.g.,* colorimetric detection assays to mass spectroscopy), few tiered analytical strategies are established for ENPs.

From a consumer prospective, it would be desirable to read on the product's label if a certain product contains ENPs or if there are any ingredients in a nano-form, especially in the case of food, pharmaceutical, cosmetic, or personal care products. In order to disclose on the label of commercial products the presence of ENPs, we need to address the following: (*i*) how to determine the presence of ENPs inside of an end product; (*ii*) how to measure the external particle size (1 - 100nm); (*iii*) how to determine the number size distribution in order to apply regulatory provisions and (*iv*) whether or not the particle interacts with biological systems.[9, 72] Although insufficient information exists to predict the potential risk associated with ENPs, the scientific community is working closely to develop platforms and protocols for these sets of materials to prevent future exposure incidents.

Currently, a major issue with nanometrology is that multiple nanomaterials are present in natural systems but only few are ENPs.[84] As a result, being able to differentiate engineered from natural occurring nanomaterials is a current issue that requires attention. Analytical tools are not yet capable of distinguishing ENPs from other nano-sized materials at concentrations that are expected in environmental and biological matrices. ENPs are relatively pure in their initial form at the time of manufacture and tend to have reproducible characteristics and physicochemical properties, including particle number size distributions, particle shape, and surface properties, that are relatively simple to measure. However, when ENPs are exposed to environmental or biological relevant complex samples, they undergo transformations, oxidation and reduction reactions, dissolution, precipitation, adsorption and desorption, combustion, abrasion, and biotransformation. Studies have tried to understand how nanomaterials change when they are released into the environment.[73] However, a large number of investigations are only testing pristine solutions, using irrelevant concentrations, rare nanomaterials that are only produced in small quantities, or employing experimental procedures that only apply for a specific setting. This creates confusion and uncertainty among the scientific community and governmental agencies intending to establish proper safety regulations.

A number of publications have described techniques suitable for characterizing ENPs and they are summarized in Table 1.2.[85, 86, 87, 9] Inorganic nanomaterials, such as silver, gold, and silica nanoparticles, have the most established detection techniques. For detection purposes, numerous techniques such as flame atomic absorption spectroscopy (AAS), surface plasmon resonance (SPR), and inductively coupled plasma technology coupled with either mass spectrometry (ICPMS), atomic emission spectroscopy (AES), or optical emission spectroscopy (OES) may be used. Alternatively, to examine if nanomaterials have changed shape or have modified porosity, then electron microscopy (EM) is advantageous. Finally, if modifications to the core material concentration or surface chemistry needs to addressed, then other, more specific techniques are required. Unfortunately, these analytical methods

require that ENPs be extracted from their native environment, or that the environment be digested, destroyed, or critically altered so that the ENP is in a state that can be measured. This introduces two issues that can compromise the value of these analytical results. Sample preparation methods, such as alkaline digestion for nanoscale particles and matrices, are generally not standardized across laboratories.[81] Comparing analytical results from one laboratory to another should be done with caution. Little is known about how the various sample preparation techniques affect acquired data on ENP characteristics.[9] It is difficult to know whether the collected data provides a realistic representation of ENPs in their native environments or if the technique affected the outcome, which further misleads data interpretation for determining the effects of these materials to humans and the environment.

Table 1.2: List of the physicochemical parameters and analytical techniques to characterized ENPs.[85, 86, 87, 9]

Parameter	Analytical Technique
Chemical composition	UV -Vis, HPLC, GC/LC -MS, AAS, ICP-MS, FTIR, NMR, XRD
Particle size and size distribution	HPLC, AUC, CPS, TEM, SEM, AFM, DLS, DMA, and centrifugation
Morphology: shape, surface area, topology, crystallinity, porosity	AFM, TEM, SEM, NMR, XRD, BET
Surface chemistry: charge, coating, functionalization, catalytic activity	LDE, SPM, XPS, MS, RS, FTIR, NMR, AUC, GE, SPM, LDE, SERS
Redox potential	Potentiometric methods, X-ray absorption spectroscopy
Stability	MS, HPLC, DLS, FTIR, NMR
UV absorption (extinction coefficient), light reflection	UV-Vis

Despite the existence of many analytical methods for ENPs, no single method is capable of fully characterizing all ENPs, especially in biological and environmental samples. Thus, it is necessary to develop sample collection/ handling protocols, as well as new methods or combinations of existing analytical methods in order to obtain conclusive results. The lack of suitable analytical methods is severely limiting the ability to link toxicological, transformational, migrational, and exposure-related studies to the ultimate effects of ENPs in the systems being studied.

Chapter 2

Interactions of Engineered Nanoparticles with Artificial Cell Membranes

2.1 Abstract

In this chapter, we probe the responses of planar suspended lipid bilayer membranes, used as model cell membranes, to functionalized multi-walled carbon nanotubes (MWCNT), CdSe/ZnS quantum dots, and a control organic compound, melittin, using an electrophysiological measurement platform. An electrophysiological methodology that measure ENP-induced ion leakage through suspended lipid bilayers can provide unique insights into the lipid bilayer-ENPs interactions as well as to understand the mechanisms and conditions under which ENPs can cause disruption of, and/or passive transport through, cell membranes. Measurements show that ENPs in a concentration range of 1.6 to 12 ppm (μg/mL) disrupt lipid membranes by inducing significant transmembrane current fluxes. Suggesting that ENPs can insert and traverse the lipid bilayer membrane, forming transmembrane channels

that allow the transport of ions. This chapter demonstrates a direct measurement of ion migration across lipid bilayers induced by ENPs.

2.2 Background

Understanding the dynamic processes at the interface between biological membranes and ENPs is still in its nascent stages.[88] Interactions of ENPs at the biological interface may aid in the understanding of potential toxicity, design of safe nanoproducts, and advancement of nanomedicine.[88, 89]

Lipid bilayers, which mimic the natural fluidity and permeability of cellular membranes, constitute a continuous barrier between cells and their environment.[90, 91] The contact of engineered nanoparticles with lipid bilayers is important because it is one of the first steps towards subsequent biological effects. Our review study and previous work have attempted to elucidate ENPs' effect on lipid membrane integrity and their relevancy to cell-ENP interaction.[48] Leroueil *et al.* used atomic force microscopy on a supported lipid bilayer to detect pore formation and thinning of lipid membranes by the exposure of cationic engineered nanoparticles.[92] Each cationic particle presented in their work, despite the shape, chemical composition, size, deformability, or charge density, disrupted the lipid membranes integrity by forming holes in the membrane. Similarly, Goodman *et al.* showed that positively charged gold nanoparticles (2 nm) increase the permeability of cell membranes and lipid vesicles (*i.e.,* liposomes) more than anionic gold nanoparticles.[93] In a similar fashion, we have detected leakage from 100 nm unilamellar liposomes, via fluorescence spectroscopy, upon their exposure to 10 nm metal and metal oxide ENPs with different surface functionalities, at concentrations down to 30 ppb.[49] We found that liposome leakage increases with the ENPs' number density. Our data shows that leakage is mediated by electrostatic interactions that are primarily governed by the ENP surface functional groups and is not dependent on the particle core composition. We found that, on average, only one particle per liposome

is required to disrupt membranes. We examined the lipid bilayer-water distribution of functionalized gold, C_{60}, and fullerene ENPs with the aim of developing quantitative methods that can be used to predict the bioaccumulation, ecotoxicology (*e.g.,* aquatic environments), transport, and fate of these materials.[50, 51] This work showed that the adsorption of ENP to bilayers is also largely governed by electrostatic forces.

Carbon nanotubes (CNTs) production and usage is rapidly growing.[94] There is concern over carbonaceous nanomaterial's toxicity and fate in the environment due to their use in biomedicine, nanocomposites, and energy conversion.[52] Previous studies have shown that CNTs can exert toxic effects on cells such as oxidative stress, inflammation, inhibition of cell growth and activity, *etc.*[91, 95, 96, 97] Recent works by Semberova *et al.* and De Paoli *et al.* have shown that CNTs induced aggregation of blood platelets as well as provoked an influx of extracellular ions through cell membranes.[98, 99] These studies demonstrated the ability of CNTs to penetrate plasma membranes without noticeable membrane damage. Similarly, Kang *et al.* showed a direct correlation between physicochemical modifications of CNTs and cytotoxic effect that this carbonaceous nanomaterial has in *Escherichia coli.* [100] This work showed a higher toxic effect in bacterial systems when the nanotubes are uncapped, debundled, short in length, and well dispersed in media. Collectively, these studies suggest that CNTs compromise cellular membranes and induce leakage of intracellular contents or influx of extracellular materials. Molecular simulation studies also indicate that CNTs can penetrate lipid bilayer [101] and transport water, biomolecules as well as ions by creating artificial biomembrane channels.[102, 103, 104, 105] However, there is no experimental evidence that CNTs can disrupt lipid bilayers and modulate a bilayers natural resistance to the flux of ions and molecules.

Electrophysiological measurements, such as patch clamp techniques, are capable of quantifying small electrical currents passing through cellular membranes as well as suspended planar lipid bilayers. The great sensitivity of electrophysiological measurements in detecting current fluctuations on the order of picoamperes (pA) across the perturbed membranes have

made these techniques widely employed to monitor the formation of ion channels,[106, 107] to measure the fusion of lipid membranes via single-channel recordings,[108] and to study electroporation.[109] These techniques have also been used to probe the interaction of ENP with cells and lipid bilayers. Chen *et al.* reported that a range of cationic polymer nanoparticles induced current fluxes across living human cell membranes and estimated the formation of nanoscale hole defects ranging from 3 to 20 nm.[110] Ramachandran *et al.* and our group have shown that water-soluble CdSe/ZnS quantum dots (QD) induce current flux across planar lipid bilayer membranes (pBLMs), which are protein free phospholipid bilayers suspended across a $\sim$150 μm diameter aperture.[111, 112] We correlated the current fluctuations induced by QDs adsorption on pBLMs with fluorescent microscopy.[112] Our measurements showed that electrical fluctuations occur when QDs adsorb and aggregate on fluid lipid bilayers. This work suggests that QD aggregates form nanoscale pore defects ($\sim$2 nm), which allow the passage of ions. However, there was not experimental evidence on how ENPs' concentration affects lipid membrane disruption and quantification methods that describe this interaction. More recently, de Planque *et al.*. used electrophysiological measurements to evaluate the ENP disruption of lipid membranes on suspended planar lipid bilayers that are formed by bringing two monolayer lipid microdroplets into contact within a microfluidic channel.[113] All these prior studies collectively demonstrate that there are significant ENP-lipid bilayer interactions (*e.g.,* adsorption, disruption, *etc.*) and suggest that these interactions may be indicative of cellular responses to ENPs and toxicity effects.

In this chapter, we report on the interaction of functionalized multi-walled carbon nanotubes (MWCNTs) with 1,2-dioleyl-sn-3-phosphatidylcholine (DOPC) lipid bilayers as model cell membranes using electrophysiological measurements on pBLM. We focus on MWCNTs, because they are carbonaceous ENPs with the highest volume manufacturing worldwide with an estimate production rate of 3400 ton/yr.[94] In this work, we use carboxyl functionalized MWCNTs, which have been characterized in a wide range of toxicity assays as part of the NIEHS NANO-GO consortium.[114, 115] Here, we compare the lipid bilayer dis-

ruption behavior of MWCNTs with that of QDs, and melittin, a well-known pore-forming peptide.[116, 117, 118] We quantify the current flux events resulting from lipid bilayer-ENP interactions by calculating the fractional event interaction (FEI) and average conductance as a function of multiple ENPs' concentrations. The results show that the MWCNT disrupt the bilayer in a different mechanism than melittin and QDs, which require aggregate complexes to cause leakage. Our data suggest that MWCNTs insert and traverse the lipid bilayer membrane, forming transmembrane carbon nanotubes channels that transport ions. Current fluxes patterns, FEI, and average conductance calculations of ENPs are used to shed light on the possible interaction mechanism of lipid membrane disruptions.

2.3 Experimental Methodology

2.3.1 Materials and Methods

We examined the interactions of ENPs with suspended planar lipid bilayers using electrophysiological measurements. We used functionalized carboxyl MWCNTs obtained as a consortium material from NIEHS NANO-GO where their fabrication and characterization have been documented in a previous reports.[114, 115] MWCNTs have a reported outer diameter of 20-25 nm, an inner diameter of 5-10 nm, and a length of 10-30 μm, as confirmed by TEM, shown in Figure.2.1. The MWCNTs have a reported purity greater than 99% by weight as carbon nanotubes with no metal catalyst impurity measured by thermogravimetric analyses.[115] The carboxyl functionalized MWCNT stock solution was prepared by dispersing dry powder (10 mg/10 mL) in ultrapure water (18.3 MΩ-cm, Nanopure) followed by mild sonication for 1 h (40 Hz, 2510DTH Branson, Ultrasonic Corp., Danbury, CT). We compared the MWCNT results with carboxyl CdSe/ZnS QDs (Q21341MP - Invitrogen, Eugene, OR) and melittin (CAS: 20449-79-0 Sigma Aldrich St. Louis, MO), a peptide well known to disrupt lipid membranes. We dissolved 5 mg/mL of the dry melittin powder in 20 mM N-(2-hydroxyethyl)piperazine-N'-(2-ethanesulfonic acid) (HEPES) buffer (CAS: 7365-

45-9 Sigma Aldrich St. Louis, MO) at pH = 7.4 and kept frozen at -20°C. The melittin sample was thawed at 23°C prior to use.

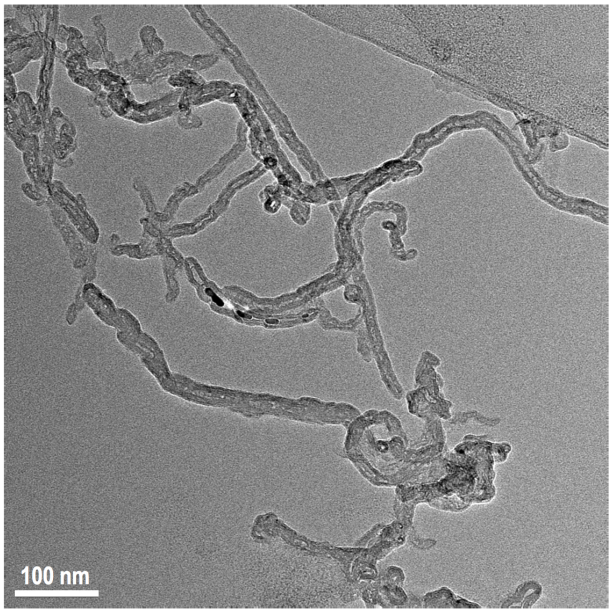

Figure 2.1: Transmission electron micrograph of multiwall carbon nanotubes suspended in 20 mM HEPES at 20 ppm concentration.

Our suspended lipid bilayers were constituted by 1,2-dioleyl-sn-3-phosphatidylcholine (DOPC) lipids (CAS: 4235-95-4 Avanti Polar Lipids, Alabaster, AL). 20 mM HEPES and 20 mM KCl at pH = 7.4 were used in all experiments, prepared using purified water (Milli-Q Advantage A10 system, Millipore Corp., Billerica, MA). We chose this electrolyte to keep the electrophysiological measurement signal-to-noise ratio as large as possible (*i.e.,* higher conductivity results in larger signal-to-noise) without sacrificing particle stability (*i.e.,* aggregation due to reduction in electric double layer thickness or surface charge). We did not use any surfactants or dispersion stabilizing chemicals so as to avoid any other perturbation of the suspended lipid membrane.

We measured the hydrodynamic size and zeta potential of the particles and lipids membranes using dynamic light scattering (DLS) (NICOMP 380 ZLS, Particle Sizing Systems, Santa Barbara, CA) over a 60 min time period, during which typical interaction experiments were performed. The relationship between the size of particles and their Brownian motion

is described by the Stokes-Einstein equation.[119] The zeta potentials of particles influence their electrophoretic mobility, as describe by the Henry equation and the Smoluchowski approximation.[120] DOPC lipids zeta potential were measured using liposomes that were prepared using the extrusion method.[121] Briefly, dry DOPC lipid powder was dissolved in chloroform and then dried with N_2. The resulting lipid film was hydrated with the same buffer electrolyte solution (20 mM HEPES with 20 mM KCl) under vortex mixing to form multilamellar liposome suspensions. The suspensions were passed through polycarbonate membrane filters with a pore size of 100 nm using a commercial extruder (LIPEX, Northern Lipids Inc., BC, Canada) 11 times to obtain ∼100 nm unilamellar liposomes.

2.3.2 Electrophysiological Measurement Platform

We examined the interactions of ENPs with suspended lipid bilayer membranes using electrophysiological measurements by continuously monitoring the current across the suspended pBLM (Figure.2.2). 3 ml polystyrene reservoirs (*i.e.,* cis and trans) (Warner Instruments LLC., Hamden, CT) are separated by a 150 μm diameter aperture over which the lipid bilayer is suspended. The reservoir chamber is mounted in a Faraday cage on a vibration isolation table to achieve optimal shielding from spurious electromagnetic radiation and reduction of mechanical noise. A low-noise extracellular patch clamp amplifier (EPC8, HEKA Instruments Inc., Bellmore, NY) with Ag/AgCl electrodes immersed into each reservoir measured the current that migrates across the bilayer. The current passing through the bilayer is amplified, filtered with a low-pass, 8-pole Bessel filter at 1 kHz, sampled at 10 kHz (National Instrument, PCIe-6251 DAQ board), recorded using a custom LabView script, and processed with an in-house Matlab code (refer to Appendix). A positive ion migration flux from the cis to the trans compartment is measured as positive current. All experiments presented in this paper were conducted at 20°C.

The suspended lipid bilayer was painted across the 150 μm aperture using the conventional Montal-Mueller technique.[122] First, a DOPC (0.4 mL at 10 mg/mL) solution in

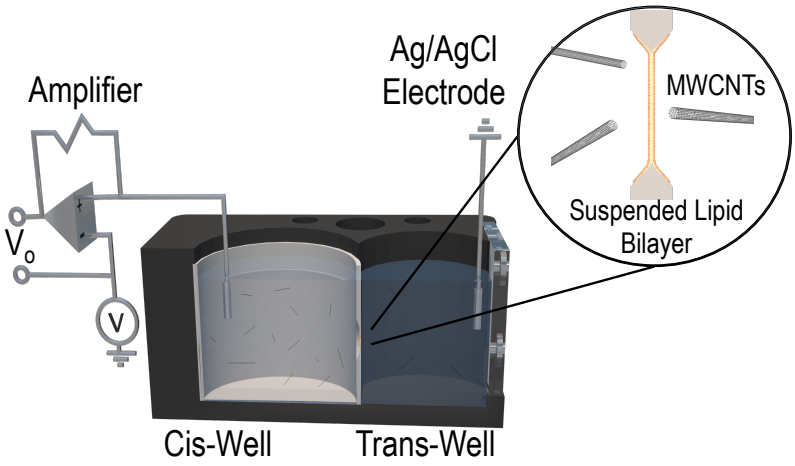

Figure 2.2: Schematic of the experimental setup for electrophysiological measurements on pBLM. The ion migration across the bilayer is monitored using a low-noise amplifier and Ag/AgCl electrodes. A lipid bilayer is suspended across a 150 μm polystyrene aperture that separates the cis and trans well. ENPs (shown here as MWCNT) are added to the cis-well and disrupt the bilayer and results in an increase in the measured electrical current.

chloroform was placed in a test tube and dried by a gentle stream of pure N_2 gas and left in a desiccator overnight. The dry lipid film was reconstituted in 1 mL of decane. The DOPC lipid solution was freshly prepared immediately prior to every use to minimize potential variability in the lipid membrane permeability. Next, we primed the 150 μm aperture with a small quantity of lipids prior to adding electrolyte. Then 3 mL HEPES-KCl buffer electrolyte was added to each reservoir in an effort to minimize the differential hydrostatic pressure across the reservoirs. We painted the membrane by immersing a pipette in the DOPC lipid solution and gently spreading it on the working aperture using the Montal-Mueller technique.[122] A true bilayer exhibits a high resistance of $\sim$10 GΩ and the ability to be ruptured with a voltage pulse.[111, 112, 123] We examined the existence of proper pBLM by applying a 500 mV voltage pulse to rupture the bilayer. This experimental step is repeated three times to confirm of a proper bilayer membrane formation before initiating experiments by adding nanoparticles to the cis reservoir. For the case of MWCNTs experiments, we mixed the particle suspension in situ with a stirring bar for 5 s prior to recording

the current flux, which is a standard practice in pBLM measurements when studying ion channels.[117, 124, 125]

We performed experiments to ensure that adsorption of the particles to the bilayer and subsequent disruption was not induced by the applied electric field. In some experiments we reversed the field and still measured similar disruptions. We conducted experiments where the applied voltage was set to zero for several minutes to allow the particles to interact. When turning the voltage back up to 100 mV we observed electrical currents that were consistent with the time that had transpired with the amplifier off. These experiments provide confidence that the electric field generated by the amplifier does not significantly contribute the observed ENP interaction with the bilayer.

2.3.3 Transmission Electron Microscopy

TEM images of MWCNTs were obtained using a TF20 transmission electron microscope (TEM) (FEI) with a 200 kV accelerating voltage and a CCD camera (Gatan, Inc, CA) with a chip that was cooled to 25.6°C. A 400 mesh C-flatTM Holey Carbon Grid (Protochips, Inc., NC) that was firstly glow discharged for 20 sec at 20 mA with Pelco Easiglow Glow Discharge Cleaning System (Ted Pella, Inc., CA). TEM samples were prepared by drop casting $\sim$5 μL aliquot of MWCNT suspended in 20 mM HEPES and 20 mM KCl that was added onto a grid at a concentration of 10 ppm, followed by solution removal with Whatman filter paper after 2 min of exposure.

2.4 Results and Discussion

2.4.1 Lipid bilayer and ENPs Characterization

We measured the zeta potential and particle sizes every 15 minutes for a total time of 60 min period. Over this time, the measured size and charge remained relatively constant, suggesting that the particles do not aggregate in HEPES-KCl buffer (pH 7.4, 20 mM).

Hydrodynamic sizes and zeta potentials of particles are reported herein as means of triplicate measurements. The MWCNTs had an average hydrodynamic diameter of 112.0 ± 0.46 nm (one standard deviation) and an average zeta potential of -16.0 ± 0.7 mV. Although the use of DLS is not appropriate for non-spherical particles or for long-aspect ratio materials, we obtained semi-quantative data to show the lack of aggregation in our buffer solution. This measured size correlates with the size revealed by TEM micrographs of MWCNTs (Figure.2.1). The QDs had an average hydrodynamic diameter of 12.7 ± 0.79 nm and an average zeta potential of -9.8 ± 1.1 mV. The melittin and DOPC lipids revealed an average zeta potential of 13.4 ± 1.1 and -12.1 ± 1.5 mV, respectively (Table2.1)

Table 2.1: Zeta potential of nanoparticles and lipid bilayers used in the study. The solution chemistry is the same as that used in the electrophysiological measurements (*i.e.,* pH = 7.4, 20 mM HEPES and 20 mM KCl).

Materials	Zeta potential (mV)
MWCNTs	-16.0 ± 0.7
QDs	-9.8 ± 1.1
Melittin	13.4 ± 1.1
DOPC lipid bilayer	-12.1 ± 1.5

2.4.2 Lipid Bilayer and ENPs Interactions

A set of representative nanoparticle and suspended lipid bilayer interactions are shown on Figure.2.3. In the absence of nanoparticles (Figure.2.3A), the current passing through the lipid bilayer was very low at ∼8 pA at an applied voltage of 100 mV and remained steady for a period of ∼600 s. The lipid membrane created a good ion flux seal with a resistance of ∼8 GΩ, as measured by applying a ramp voltage and determining the slope of the resulting current-voltage curve. The low bilayer current flux is consistent with the fact that bilayers serve as an effective barrier to the flux of ions as shown in prior studies.[111, 112, 113] The low current flux and the ability of facile disruption after the application of a 500 mV voltage pulse confirms the formation of a suspended lipid bilayer. Our bilayers were typically stable

for ∼20 h. To the right of Figure.2.3A, we report normalized histograms of current flux events.

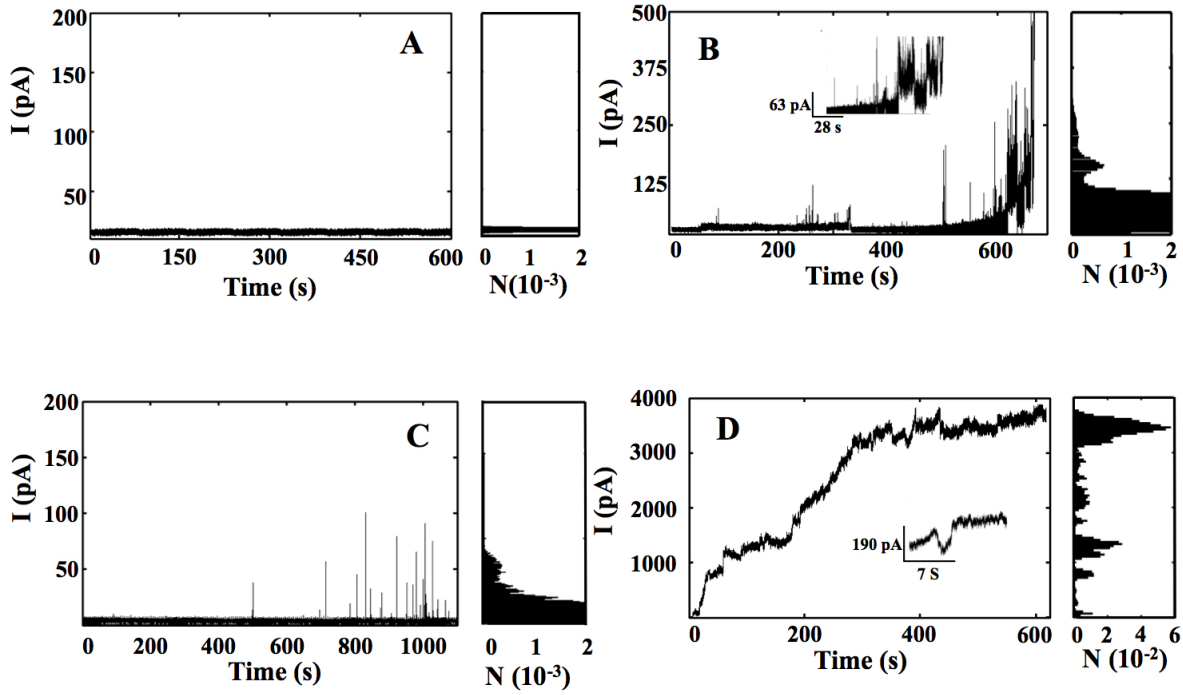

Figure 2.3: Current-time traces of DOPC lipid bilayers at pH = 7.4 (20 mM HEPES and 20 mM KCl) and normalized current histograms with (A) Absence of nanoparticles; (B) melittin, a well-known pore forming peptide on lipid bilayers, at 6 ppm; (C) carboxyl quantum dots at 6 ppm; (D) functionalized multi-walled carbon nanotubes at 6 ppm.

The normalized histograms are discrete estimates of probability density functions defined as,

$$H_j = \frac{N_j}{\Sigma_j N_j} \tag{2.1}$$

where N_j is number of events in bin j at a given current. Figure.2.3A displays a single peak spanning from 4.5 to 10.5 pA and a mean of 8 pA, which represents the baseline current due to the intrinsic ion permeability of the lipid bilayer and instrument noise under the applied electric field.

Figure.2.3B shows the current flux across the suspended lipid bilayer induced by 6 ppm melittin, our reference organic compound that is well know to generate pores in lipid membranes. After 10s of melittin exposure, we observe an initial sharp current burst (∼50 pA)

that lasts for 90 ms. Next, a current step of ∼80 pA occurred at 83.5 s that lasts for ∼300 ms. The current bursts became more intense and frequent, eventually resulting in total membrane failure after 600 s. This disruption of the membrane was consistently observed at all studied concentrations, shown in Figure.2.4A and B. The histogram shows a distinctive current peak at 147 pA or 1.47 nS, corresponding to the multiple bursts shown in the inset on Figure.2.3B. The spontaneous formation and temporal instability of the current signatures are thought to be influenced by the peptide's Brownian motion. These results are consistent with previous studies that also reported burst-like current traces due to defined nanopores formed from four or more melittin molecules.[117, 124] Melittin incorporates into lipid membranes and induces sporadic disruption and current signals (*i.e.,* pore formation) due to Brownian rearrangement and conformational changes of the peptides in the membrane association.

Upon the addition of carboxyl QDs at 6 ppm we observe similar current-time traces to melittin, as shown in Figure 2.3C. Initially, the current flux remained steady at the baseline level, similar to what is observed in the control and melittin experiments, suggesting that there is no interaction of the QDs with the bilayer. A first set of current bursts is later observed at 500 s with an event time duration of ∼200 ms and maximum current amplitude of 40 pA. The current bursts in the presence of QDs occur intermittently with peak currents varying from 10 to 105 pA. 210 s after the first interaction event, we observe larger and more frequent current fluctuations at amplitudes between 15 to 105 pA with an average current of 60 pA. The QDs do not cause a complete lipid bilayer failure at this concentration or at 60 ppm (see Figure 2.4C). The histogram of Figure 2.3C presents a broadened primary peak at 7 pA and a second broad peak centered at 60 pA. The primary peak at 7 pA, which represents the baseline signal, has an extended tail into higher currents because of low magnitude current spikes induced by QDs. The secondary peak in the histogram at 60 pA or 0.6 nS represents an increase in the membranes permeability due to QDs. These current fluctuations have been attributed to the oligomeric aggregation of QDs onto the bilayer that

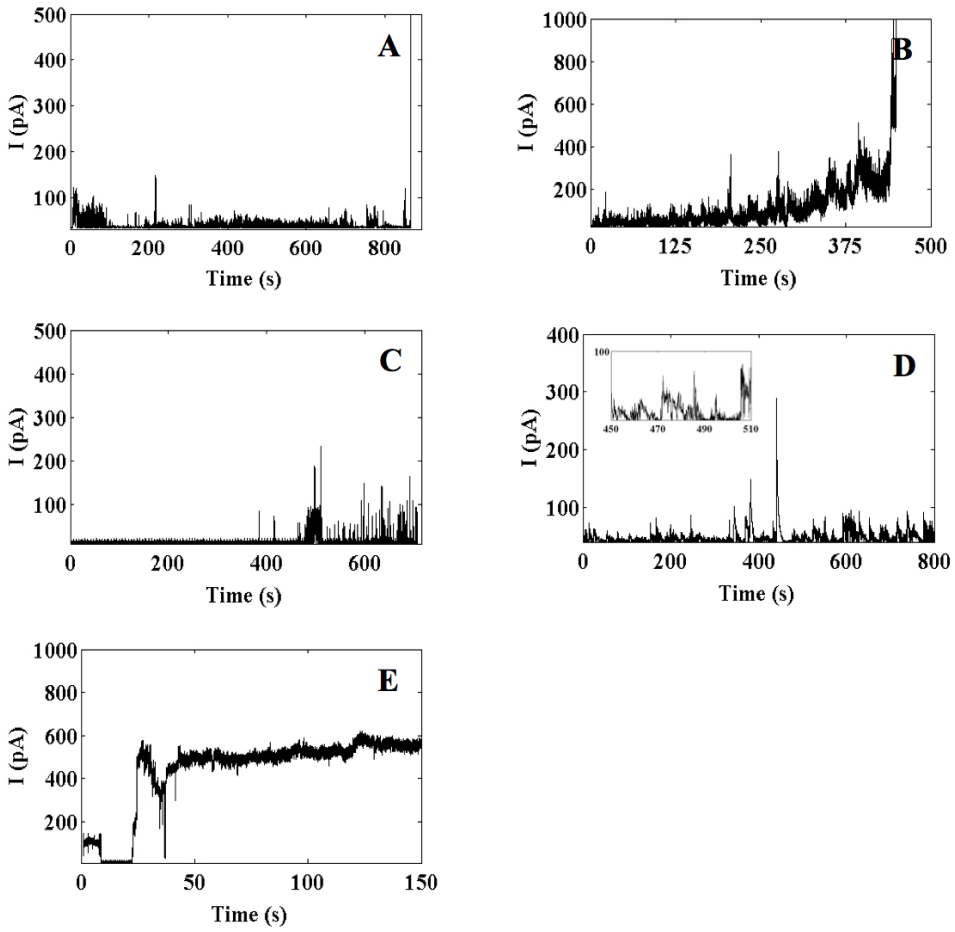

Figure 2.4: Representative current traces with DOPC lipid bilayers at pH = 7.4 (20 mM HEPES and 20 mM KCl). (A) melittin at 0.06 ppm and (B) 12 ppm; (C) carboxyl quantum dots at 60 ppm; (D) functionalized multi-walled carbon nanotubes at 1.6 ppm and (E) 12 ppm.

creates nanopore defects on the lipid bilayer, through which ion transport occurs.[111, 112] We previously showed that QDs aggregate on membranes and diffuse freely allowing the passage of ions.[112] This current signature of QDs is similar to melittin, which suggests that they too require an aggregate of particles to induce ion leakage. Spherical, carboxyl polymeric nanoparticles have also been shown to create pores on supported lipid bilayers.[126] The sporadic current bursts in the data suggest that the defects induced by QDs open and close intermittently, similar to melittin.

Figure 2.3D reports the current flux across the suspended lipid bilayer induced by MWCNTs at 6 ppm. In contrast to melittin and QDs, MWCNTs interacted with the suspended

lipid membrane more rapidly (typically within ~5 s) and in a stepwise manner. MWCNTs induced a rapid increase in trans-membrane current of ~50 pA followed by a short plateau lasting for 4 s. We then observe a drastic escalation of current to 950 pA during an 11 s time lapse. The current then remained constant for 20 s and then rapidly increased to 1200 pA. The current flux increased in steps, with each step possessing a different magnitude. For example, the first current step was at 50 pA followed by 950, 1200, 1400, 1800, 2150, and 3200 pA. Eventually, the current flux reached 3650 pA and then a complete lipid bilayer failure occurred after 600 s of exposure. The normalized histogram shows multiple current peaks ranging from 26 pA to 3650 pA (0.26 nS to 36.5 nS) corresponding to the current steps recorded in Figure 2.3D. We observe similar behavior at lower (1.6 ppm) and higher (12 ppm) MWCNT concentrations as shown in Figure 2.4D and E.

We believe that melittin and QDs disrupt the bilayer by similar mechanisms. They both show sporadic current spikes and both require several particles/molecules assembled to generate leakage. In contrast, MWCNTs show step-like currents that increase with time, suggesting that a different mechanism may be at work. We hypothesize that MWCNTs insert and traverse the lipid bilayer membrane, forming transmembrane channels that transport ions through the tubes core, as shown in Figure 2.5. The current steps increase as individual nanotubes span the bilayer, creating additional channels for ion transport.

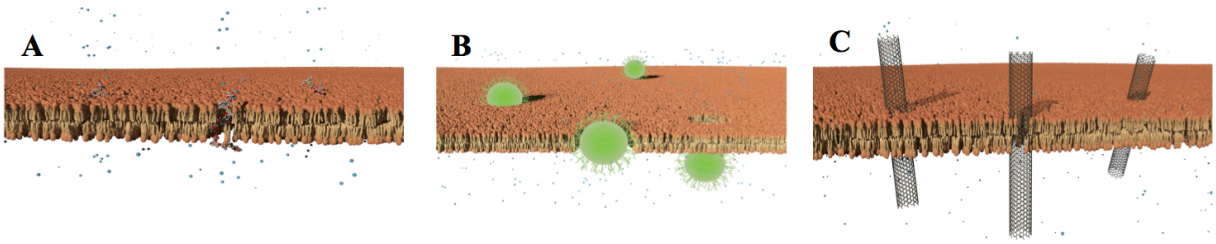

Figure 2.5: Schematic showing some potential ENP interactions with suspended lipid membranes in the form of melittin (A), quantum dots (B), and multi-wall carbon nanotubes (C). The small blue dots emanating from the pores represent the leakage of molecules or organelles across the lipid bilayer.

Our hypothesis is supported by previous experimental and computational studies which have shown than CNTs can insert into or passively diffuse (*i.e.,* endocytosis independent)

across cell membranes.[103, 101, 97] These molecular dynamic simulations show that the insertion of CNTs into a biomembrane can occur in a spontaneous fashion. The CNT - lipid mechanism involves a two-step process, first the tubular particle adheres onto the membrane surface, and then reorients to adopt a transmembrane configuration. In a similar fashion, ions in an electrolyte have been shown to electromigrate through cores of CNT,[104, 127, 128] suggesting that our observed current flux may be made up of ions electromigrating through the core of CNTs that are inserted and span the suspended lipid bilayer. Lee *et al.* and Choi *et al.* measured ion transport through cores of CNT embedded within resins, which strongly supports our hypothesis.[129, 130] They showed that current flux through the cores occurred with quantized current steps with stark similarity to our measurements shown in Figure 2.3D and Figure 2.4D and E. A definitive investigation of the mechanism in causing the bilayer current flux is ongoing work in our lab.

2.4.3 Quantification of ENP - Lipid Bilayer Interactions

Our results suggest that different particles can induce significantly different current signatures (*e.g.,* time to create a disturbance, current level, current burst length, *etc*) which presents a challenge to quantitatively compare their interaction with the bilayer. Because the leakage caused by the ENP is a dynamic phenomenon, there are not obvious single-valued quantitative measures that can be used to assess the relative potential for ENP to disrupt a bilayer. Historically, current-time traces and histograms have been used to quantify electrophysiology measurements, yet these measures do not lend themselves well to comparison with varying particle properties or concentration. Here, we provide single-value, quantitative measures that can be potentially used to compare ENP against each other and other toxicity assays.

In this chapter, we present the average conductance and the fraction event interaction (FEI) measure. The average conductance represents the average magnitude of all the lipid bilayer - nanoparticle interaction events integrated over a current-time trace plot, excluding

the background noise events at $I < 10$ pA, which corresponds to ∼2 standards deviation from the mean current background noise. The FEI describes the fraction of time the bilayer is disrupted, defined as,

$$FEI = \sum_{j=j_{noise}}^{\infty} \frac{N_j}{\sum_j N_j} \tag{2.2}$$

where j_{noise} is the bin associated with the background noise current at $I = 10$ pA. This is equal to the area under the normalized histograms (*e.g.,* Figure 2.3) excluding the area under the curves due to background nose, $I = 0$ - 10 pA. The FEI is a measure of the fraction of time (0 - 1) that the particles disrupt the bilayer significantly from the background levels. A larger FEI for a particular particle indicates that the lipid membrane spends more time interacting over the recorded experiment duration. The average conductance and FEI values reported are averages of triplicate experiments at a fixed ENP mass concentration.

Figure 2.6 compares the fractional event interaction (FEI) of MWCNTs, QDs and melittin at several mass concentrations. The FEI increases with ENP number density (number of particles / per volume). Number density should directly correlate with the particle-membrane collision frequency, which should result in greater nanoparticle adsorption and subsequent leakage. Figure 2.7 shows the average conductance across the bilayer. The MWCNTs induced the largest average conductance ranging from 0.5 to 3.3 nS for mass concentrations of 1.6 to 12 ppm, respectively. QDs exhibited the lowest average conductance, which ranged from 0.20 to 0.45 nS for mass concentration of 6 to 60 ppm. We calculated the number density of the particles at 12 ppm as 2.5 E^{15}, 2 E^{10}, and 1.3 E^{12} ml^{-1} for the melittin, MWCNT, and QDs, respectively. These results show that MWCNT exhibit stronger interactions with the bilayer with less than two orders of magnitude number density, consistent with the argument that the tube's interaction with the bilayer are distinct from the spherical particles and melittin.

Collectively, the average conductance and FEI measures show that the membrane disruption increases with mass concentration. The dose dependency can be attributed to a larger

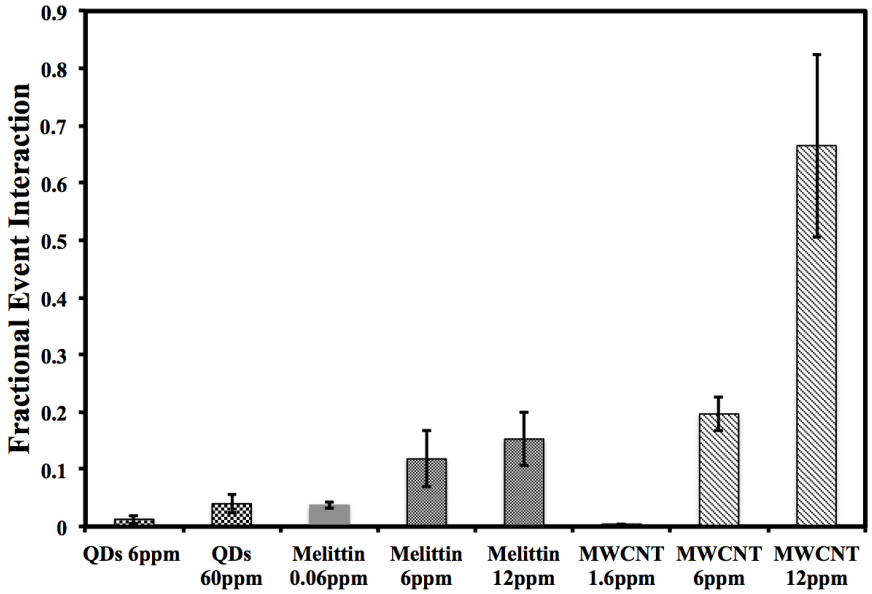

Figure 2.6: Fractional event interaction of QD, MWCNT, and melittin with DOPC lipid bilayers at pH = 7.4 (20 mM HEPES and 20 mM KCl) at several nanoparticle concentrations. The fraction event interaction is a quantitative measure of the fraction of time that the nanomaterials disrupt the bilayer. The FEI increases with concentration and varies with particle composition and shape.

number of particles present, which results in a greater probability of particle contact with the lipid membrane. Although the average conductance and FEI combined allow a quantitative analysis that captures the average interaction behavior of nanoparticle and lipid bilayers, it does not reflect the specific interaction patterns (*i.e.,* sporadic spikes versus stepwise current increase) and the eventual breakdown of lipid bilayer, which varies from particle to particle and can only be observed in the current-time traces. Thus, for a comprehensive and unbiased assessment of lipid bilayer-nanoparticle interactions, an analysis including the three pieces of information may be necessary.

2.5 Summary

In this chapter we report a direct measurement of ion migration across lipid bilayers induced by CNTs. Our results suggest that the distinctive current flux behavior for MWCNTs

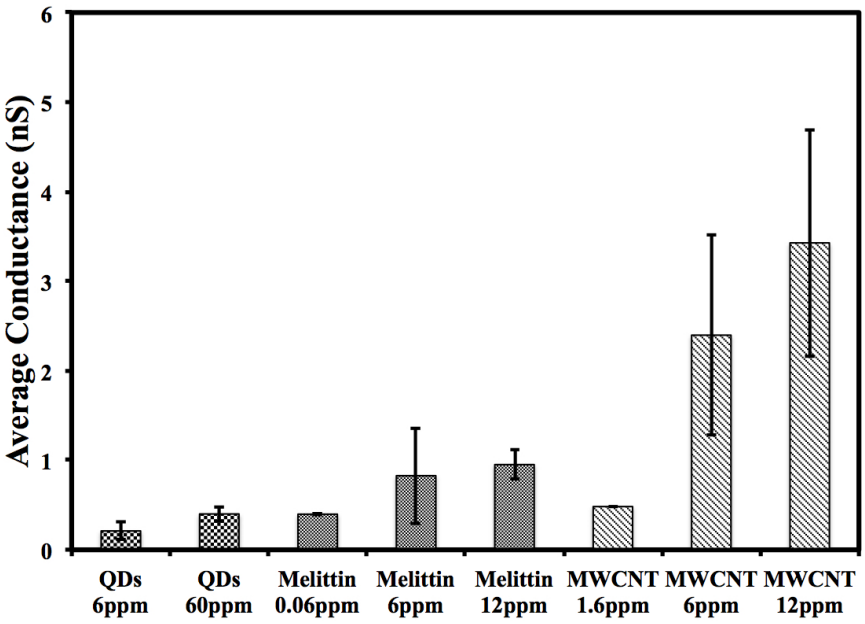

Figure 2.7: Average conductance induced by QD, MWCNT, and melittin on DOPC lipid bilayers at pH = 7.4 (20 mM HEPES and 20 mM KCl) at several particle mass concentrations. The average conductance is calculated excluding the background signal.

may be attributed to ions electromigrating through the core of CNTs that are inserted and span into the suspended lipid bilayer. Electrophysiological measurements enabled monitoring of ENP-lipid bilayer interaction dynamics in real time with millisecond temporal sensitivity. The diverse set of current traces suggests that the mode of bilayer disruption is dependent on the shape and concentration of particles. Furthermore, we presented a quantitative analysis (*e.g.,* FEI and average conductance) of the interaction of ENPs-lipid membranes that captures the ion migration effect induced by particle shape, size and concentration. Given that cellular membrane disruption is one of the potential mechanisms leading to nanotoxicity, probing the lipid bilayer disruption may provide insight into the nontoxicity mechanisms as well as a potential predictor of cytotoxicity studies for preliminarily screening of ENPs.

Chapter 3

Colorimetric Assay to Detect Engineered Nanoparticles (CADE) Catalytic Reactivity

3.1 Abstract

There is a need for new methodologies to quickly assess the presence and reactivity of engineered nanoparticles (ENPs) in commercial, environmental, and biological samples since current detection techniques require expensive and complex analytical instrumentation. In this chapter, we investigate a sensitive, simple and portable colorimetric assay that assesses the surface reactivity of ENPs in complex matrices (*e.g.,* environmental waters, serum, urine, and in dissolved organic matter) at concentration levels as low as part per billion (ppb) or ng/mL . Surface redox reactivity is a key emerging property related to potential toxicity of ENPs with living cells, and is used in our assays as a key surrogate property for the presence of ENPs and a first tier analytical strategy towards assessing nanoparticle exposures. We detect a wide range of metal (*e.g.,* Ag and Au) and oxide (*e.g.,* CeO_2, SiO_2, VO_2) ENPs with a diameter range of 5 to 400 nm and multiple capping agents (tannic acid

(TA), polyvinylpyrrolidone (PVP), branched polyethyleneimine (BPEI), polyethylene glycol (PEG)), ENPs extracted from commercial products, and correlate the surface reactivity of particles with potential biological effects (*e.g.,* bacterial cytotoxicity). This method is sufficiently sensitive (ppb levels) to measure concentrations typically used in toxicological studies, and uses inexpensive, commercially available reagents.

3.2 Background

In this chapter, we report a colorimetric assay to detect engineered nanoparticles (CADE) that can be used to screen for ENP catalytic surface activity in biological and environmental relevant samples. Surface reactivity of nanoparticles is a key emerging property related to potential toxicity of materials with living organisms. We leverage the surface catalytic redox properties of ENPs to provide a simple colorimetric detection assay. Potential applications of the catalytic CADE assay are: (*i*) monitoring known nanoparticles in complex media over time during lab or field studies, (*ii*) industrial hygiene settings where known nanoparticles are being used, and (*iii*) screening for the presence of unknown surface reactive nanomaterials that would be complimented later by more advanced analytical techniques for identification. Figure 3.1 shows a schematic representation of the catalytic electron transfer mechanism between an organic dye, methylene blue (MB), and a reducing agent, sodium borohydride (BH_4), in the presence of ENPs. When ENPs are introduced to MB – BH_4 solution, they serve as a catalyst for reducing the dye - reductant agent pair by promoting the electron transfer between the reductant and dye. Multiple studies report the mechanism on how nanoscale metals (but not their bulk counterparts) are catalytically active due to the reduction of their redox potential. [131, 132] The literature suggests that the redox potential of ENPs needs to be found between the redox potential of MB and BH_4 for it to act as a catalyst, since these reduction reactions are thermodynamically, but not kinetically, favorable.[133,

134, 135, 136] In this case, nanoparticles serve as an electron relay in the redox reaction to transfer the electron from the donor (BH_4) to the acceptor (MB).[137, 138] Reducing the dye from its oxidized state to its reduced state results in a color change from blue (oxidized state) to colorless (reduced state) due to a change in absorbance properties between the oxidized and reduced dye molecules. We plan to employ the unique surface catalytic properties of ENPs as a detection approach, demonstrating its validity across a range of ENPs compositions, surface coatings, and environmental/biological relevant fluids. CADE assay only requires a reducing agent and an organic dye for detection. Addition of ENPs to the dye-reductant solution (or addition of dye-reducing agent to a suspension containing ENPs) results in a rapid color change that can be inspected visually or a by portable UV-vis spectrophotometer for improved detection capabilities. We show that CADE assay functions in a wide range of complex matrices and does not require elaborate sample preparation, advanced instrumentation or highly trained personnel.

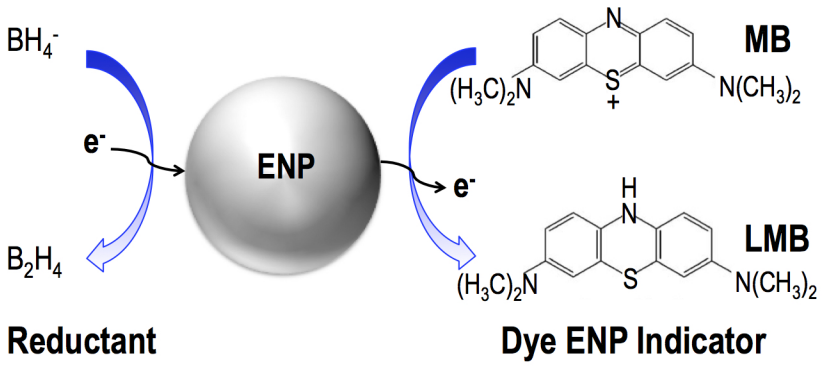

Figure 3.1: Schematic diagram of dye reduction, methylene blue (MB) to leuco-methylene blue (LMB), electron transfer mechanism in the presence of ENPs.

We have selected a dye-reductant system,CADE, that: (*i*) can be detected colorimetrically (dye has different colors in its oxidized and reduced forms); (*ii*) consists of a dye whose reduction is thermodynamically, but not kinetically, favorable; (*iii*) exhibits minimal human toxic effects, materials are not flammable, and stable at room temperature;[139] and (*iv*) is inexpensive for future potential use as a commercially available screening assay for

ENPs. We perform several experimental studies to detect commercially available ENPs with a variety of core compositions (Au, Ag, CeO2, SiO2 and VO2), surface coatings (tannic acid (TA), polyvinylpyrrolidone (PVP), branched polyethyleneimine (BPEI), polyethylene glycol (PEG)), and sizes (5 - 400 nm). We use CeO_2, SiO_2, and VO_2 particles because of their large volume use in applications such as chemical mechanical planarization in the semiconductor industry,[140] energy storage,[141] catalysis,[142] and biomedicine.[143] We primarily use Au and Ag particles because of their commercial availability in a wide range of sizes and surface functionalities. Silver nanoparticles are also commonly used as a disinfectant in commercial products.[144, 36] We examine the effect of ENPs' concentration, size, surface area, and capping agents for CADE assay in pH - buffered ultrapure water as well as in a variety of environmental and biological matrices (*e.g.,* environmental waters, serum, urine, and dissolved organic matter). The limit of detection (LOD) and limit of quantification (LOQ) are quantified at as low as part per billion (ppb) or ng/mL.

3.3 Experimental Methodology

3.3.1 Environmental and Biological Matrices

In order to assess the capabilities of our dye-reductant assay to detect the presence of ENPs in complex matrices, we used natural organic matter (NOM) and lake water as environmental samples, serum and urine as biological matrices. An aqueous solution of 8 mg NOM/L Standard Suwannee River (SR-NOM) (International Humic Substances Society CAS: 1R101N, IHSS, MN) was prepared by dissolving SR-NOM in ultrapure water. After the solution had been prepared, it was continuously shaken and placed in a horizontal, temperature-controlled (25 °C) water-bath sonicator (Branson), where it was allowed to equilibrate for ∼24 h in the dark. This solution was subsequently calibrated for NOM concentration against UV-vis absorbance at 254 nm. Calibration experiments showed that absorbance at 254 nm was directly proportional to NOM concentration (data are not shown

here). Characterization details (*e.g.,* average molecular weight and composition) of NOM are given elsewhere.[145]

Natural waters samples were collected in polycarbonate vials from Lake Union (Seattle, WA) in May 2013 and maintained at room temperature. Before every experiment, the natural water sample was continuously mixed on a rotary shaker (50 rpm) for 1 h. We used synthetic urine, prepared as described previously,[146] and serum from male and female adult mice. Our serum collection was performed by Megan M. Cartwright from UW Nanotoxicology Center and carried out as follows: we executed all animal experiments in accordance with the National Institutes of Health Guide for the Use and Care of Laboratory Animals, with the approval of the University of Washington Institutional Animal Care and Use Committee. All efforts were taken to minimize distress and suffering. We collected sera from male and female adult ($\geq$ 6 weeks old) mice on a C57Bl/6 background which were Gclm-/- or -/+ and Lep db-/- or -/+ (Jackson Labs stock #000642).[147, 148, 149] Mice had free access to Purina Standard Mouse Chow and drinking water, and were group housed in a temperature-controlled room on a 12 h light : 12 h dark cycle. We humanely euthanized the mice by CO_2 narcosis followed by immediate cervical dislocation. The peritoneal and pleural cavities were opened and blood collected in a 1 mL syringe with a 22G x $1\frac{1}{2}$" needle. Blood was allowed to clot for 20 minutes at room temperature in individual serum separator tubes (BD catalog #365956) before being placed on ice. We then separated the serum fraction from the coagulated blood by centrifuging the samples at 7,500 g for 5 minutes according to the manufacturer's protocol. Sera was pooled in a sterile microcentrifuge tube and frozen at -80 °C until used for experiments.

3.3.2 Engineered Nanoparticles

We used Au nanoparticles (5, 10, 20, 50, and 100 nm nominal diameter) coated with tannic acid (TA), 20 nm Ag coated with TA, and 20 nm Au coated with polyvinylpyrrolidone (PVP), branched polyethyleneimine (BPEI), polyethylene glycol (PEG). Au and Ag

NPs were purchased form nanoCompsix (San Diego, CA). 150 nm CeO_2 (CAS: CE-6082) and 20 nm SiO_2 ENPs (CAS: ST-20L) were obtained from AlfaAesar (MA) and Nissan Chemical (TX), respectively. VO_2 nanoparticles were prepared utilizing the solvothermal method adopted from previous work.[150] In a typical reaction, 25 mmol of V_2O_5 (CAS: 1314-62-1, AlfaAesar, MA) was combined with 15 mL of 0.1 M oxalic acid (CAS: 144-62-7, Sigma-Aldrich, MO) and stirred for 18 hours. The oxalic acid served as the reducing and chelating agent. Completion of the reaction was noted by the color of the solution transitioning from yellow to blue, signifying a reduction of the vanadium species. The solution was then transferred into a polytetrafluoroethylene (PTFE) lined, 25 mL capacity stainless steel autoclave. The solvothermal reaction was carried out at 180 °C for 12 hours, after which the final product was isolated and dried at 80 °C overnight. The phase and crystallite size of the VO_2 material was studied using X-ray diffraction (XRD, Bruker X-ray diffractometer); the sample was scanned with Cu-K_α radiation within the range of 10° to 70° (2Θ) using a step size of 0.02° and an exposure time of 10 s. The accelerating voltage and current were 40 kV and 40 mA, respectively. The surface morphology of the VO_2 was examined using scanning electron microscopy (SEM, JEOL JSM-7000F), as shown in Figure 3.2.

ENP concentrations presented in this study are based on the manufacture's reported values. In addition, we measured the total metal concentrations of NPs via ICPMS (Table 3.1). All ENPs were characterized via dynamic light scattering (DLS) using a Malvern Zetasizer Nano-ZS, Westborough, MA. We measured the zeta potential and hydrodynamic diameter of ENPs in the same buffering agent used in experiments (*i.e.,* 10 mM HEPES at pH 7.0), ultra pure water, and complex matrices every 5 min for a total time of 30 min period. Hydrodynamic sizes and zeta potentials of particles are reported herein as means of triplicate measurements. Measured hydrodynamic sizes are marginally larger than the size reported by the manufacturer (Table 3.2, 3.3). Hydrodynamic size and surface charge measurements indicate that ENPs' sizes and surface charges remained relatively constant in HEPES buffer during ∼30 min period.

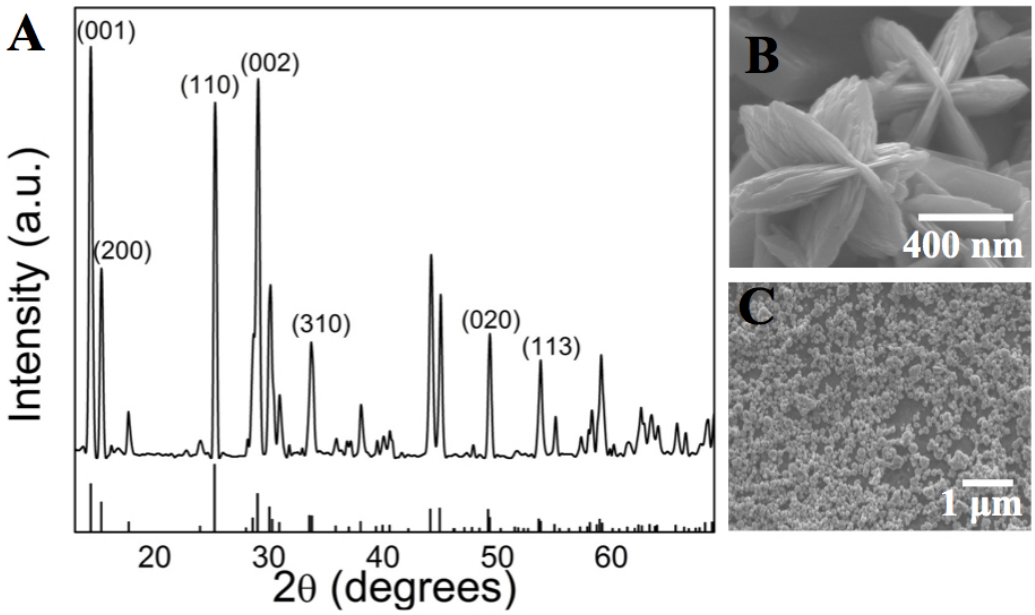

Figure 3.2: X-ray diffraction (A) and scanning electron micrographs (B - C) of VO_2 ENPs.

In order to validate the concentration values presented in this chapter, we measured the total metal concentration of nanoparticles (ENPs) via inductively coupled plasma mass spectrometry (ICMPS), as it is presented in Table 3.1. The experimental procedures of digestion for metal and metal oxide nanoparticles for ICPMS analysis were prepared utilizing previous work.[151]

To determine the element content, samples of CeO_2 were microwave digested according to standard EPA method 3030 G and then analyzed by ICPMS. Aliquots of samples (0.1 mL of CeO_2) were added to a 55 mL microwave digestion vessel separately, along with 8 mL of 70% nitric acid (HNO_3, ULTREXII Ultrapure Reagent, J.T. Baker, Avantor Materials, PA, USA), 2 mL of hydrochloric acid (HCl, 33% - 36% w/w, ULTREXII Ultrapure Reagent, J.T. Baker, Avantor Materials, PA, USA), and 2 mL of hydrofluoric acid (47 - 51% w/w, ULTREXII Ultrapure Reagent, J.T. Baker, Avantor Materials, PA, USA). The total volume of each vessel was added up to 15 mL by ultra pure water.

For SiO_2 ENPs, 0.1 mL of sample was mixed with 4 mL of tetramethylammonium hydroxide (TMAH), and the total volume was also added up to 15 mL with ultra pure water.

Negative controls without any ENPs addition were added with acid or TMAH plus water. The samples in vessels were digested in a Microwave Assisted Reaction System (MARS) Express instrument (MARS 6, CEM, NC). After cooling to room temperature, the vessels were rinsed 3 times using a total of 20 mL of a 2% nitric acid solution into a Teflon beaker. An aliquot of 2 mL of 30% hydrogen peroxide (BAKER ANALYZED A.C.S. Reagent, Avantor Materials, PA, USA) was added to each beaker to digest any remaining organics. The beaker was then heated on a hot plate at 180 °C until between 1 and 5 mL of solution remained. The beakers were removed from the hot plate and allowed to cool to room temperature. The beakers were rinsed 3 times with 2% nitric acid solution into a 50 mL volumetric flask before being stored for analysis. XSERIES-2 ICP-MS (Thermo Scientific, USA) was used for metal content analysis.

For Au ENPs suspension, an aliquot of 0.45 mL sample was mixed with 2 mL of HNO_3 and 6 mL of HCl in clean polycarbonate plastic tubes. After reacting for 20 minutes, pure water was added to reach a total volume of 15 mL. The whole solution was further diluted 20 times by 2% of HNO_3 for analysis.

For Ag ENPs suspension, an aliquot of 0.45 mL sample was mixed with 5 mL of HNO_3 and 10 mL ultra pure water in a glass beaker. The mixture was heated at 200 °C until about 5 mL the liquid was left. After cooling down the solution to room temperature, the beakers were rinsed 3 times to about 50 mL in a volumetric flask and eventually diluted 20 times with 2% HNO_3. All the tests presented in this section were conducted in duplicates.

Table 3.1: Characterization of total metal content of engineered nanoparticles measured via ICPMS.

ENPs	Concentration Reported by Manufacture [ppm]	Concentration Measured by ICPMS [ppm]
Au_{TA} (20 nm)	20	23 ± 0.7
Ag_{TA} (20 nm)	20	18 ± 1.4
CeO_2	1.8 x 10^5	(2.3 ± 0.02) x 10^4
SiO_2	2.0 x 10^5	(1.8 ± 0.11) x 10^5

We present the zeta potential and hydrodynamic diameter of ENPs in the same buffering agent used in experiments (*i.e.,* 10mM HEPES at pH 7.0), in ultra pure water, and in complex

matrices. Measurements were repeated every 5 min for a total time of 30 min period. We performed hydrodynamic size and zeta potential studies using a Malvern Zetasizer Nano-ZS. Data is reported herein as the mean of three measurements with an uncertainty of 95% confident intervals ($\alpha = 0.05$). For the case of VO_2, we determine the ENPs size by Transmission electron microscopy (TEM). Studies were carried out using an aberration-corrected Titan 80 - 300 TEM operating at 80 kV.

Table 3.2: Hydrodynamic diameter and zeta potential of nanoparticles used in the study. Measurements in ultrapure water and in the solution chemistry that we used in experimental procedures (*i.e.,* pH = 7.0, 10 mM HEPES)

ENPs	Size in ultrapure water [nm]	Zeta potential in ultrapure water [mV]	Size in HEPES [nm]	Zeta potential in HEPES [mV]
Au_{TA} (5 nm)	8.73 ± 1.77	-36.40 ± 4.52	8.51 ± 1.74	-12.80 ± 8.63
Au_{TA} (10 nm)	18.47 ± 7.18	-34.51 ± 7.55	18.02 ± 6.70	-24.70 ± 13.04
Au_{TA} (20 nm)	29.85 ± 11.61	-33.40 ± 5.66	30.13 ± 11.71	-16.30 ± 8.97
Au_{TA} (50 nm)	60.72 ± 19.57	-30.73 ± 3.69	57.82 ± 17.37	-32.42 ± 21.80
Au_{TA} (100 nm)	113.30 ± 21.96	-36.60 ± 10.90	107.0.8 ± 29.26	-24.84 ± 13.34
Au_{PEG} (20 nm)	50.65 ± 14.76	-18.75 ± 3.56	51.33 ± 16.04	-6.89 ± 19.08
Au_{PVP} (20 nm)	27.11 ± 8.46	-22.92 ± 4.72	28.07 ± 9.28	-33.52 ± 18.90
Au_{BPEI} (20 nm)	44.72 ± 17.28	31.34 ± 12.21	49.28 ± 25.49	29.60 ± 17.60
Ag_{TA} (20 nm)	28.51 ± 10.21	-18.30 ± 3.26	29.65 ± 11.26	-28.60 ± 1.60
CeO_2	161.4 ± 61.58	-51.10 ± 9.91	158.30 ± 54.88	-49.52 ± 11.20
SiO_2	28.69 ± 20.46	-37.80 ± 6.62	24.57 ± 10.29	-36.32 ± 5.29
VO_2	427 ± 10.56	-36.31 ± 5.45	–	-38.70 ± 7.18

Table 3.3: Hydrodynamic diameter of engineered nanoparticles used in the study. Measurements in ultrapure water, lake water, urine, NOM, and mouse serum.

ENPs	Size in ultrapure water [nm]	Size in lake water [nm]	Size in urine [nm]	Size in NOM [nm]	Size in serum [nm]
Au_{TA} (20 nm)	29.85 ± 11.61	30.90 ± 10.60	48.30 ± 13.70	32.10 ± 16.80	240.80 ± 180

Engineered nanoparticle detection studies were performed in 3 mL, disposable methacrylate cuvettes (Cat: 9014, Perfector Scientific, Atascadero, CA) with an optical path length of 1 cm. Cuvettes were placed in a portable UV-Vis spectrometer (USB2000+XR1-ES Ocean Optics, Dundin, FL) and mixed with a micro magnetic stirring bar, driven by an external magnetic mixer (Cat: H370170000, Scienceware, Wayne, NJ).

CADE assay consists of final concentrations of 40 μM MB (CAS: 7220-79-3, Sigma - Aldrich, St. Louis, MO), 10 mM Sodium Borohydride (CAS: 16940-66-2, Sigma - Aldrich, St. Louis, MO), and 10 mM N-(2 - hydroxy - ethyl) piperazine - N' - (2 - ethanesulfonic acid)

(HEPES, CAS: 7365 - 45-9 Sigma - Aldrich, St. Louis, MO) at pH = 7. We selected the dye concentration based on our calibration experiments shown in Figure 3.3 where 40 μM of MB falls in the linear region between absorbance and concentration of the absorbing specie, methylene blue, which obeys Beer-Lambert, as presented in Equation 3.1, law linearity regime.[152, 153]

$$C = \frac{A}{\varepsilon l} \tag{3.1}$$

Where C is the concentration of dye solution [M], A is the absorbance at λ_{max}, ε is the extinction coefficient for dye molecules [M^{-1} cm^{-1}], and l is the path length [cm].

Similarly, we studied the effect of pH and the buffering capacity on CADE by investigating multiple buffers (*e.g.,* citric acid, bis - tris, tris, and boric acid) but, ultimately, we chose HEPES as a buffering agent since it maintains the pH constant during our experimental procedures as well as minimizes the dye oxidation, which is a common reaction mechanism when reduced MB is in presence of oxygen.[154, 155] The 10 mM buffer concentration has sufficient buffering capacity without inducing particle instability, *i.e.,* aggregation due to reduction in electric double layer thickness or surface charge as a result of high ionic strength. All aqueous solutions were prepared by using ultra purified water (18.3 MΩ - cm, Milli-Q Advantage A10 system, Millipore Corp., Billerica, MA) and passed through a 200 nm, sterile filter (CAS: 28145-477, VWR international, Radnor, PA). We did not use any surfactants, dispersion stabilizing chemicals, or filtration processes in our complex matrices to avoid the perturbation of the particles or the complex media.

3.3.3 Engineered Nanoparticles as a Redox Catalyst

We investigated the catalytic activity of ENPs in presence of MB and sodium borohydride (BH_4). We prepared our working suspension by dispersing nanoparticles in ultrapure water, environmental or biological medium. The resulting suspension was placed on a rotary shaker (50 rpm) for 1 h at room temperature (23 °C) prior to each experiment. We begin

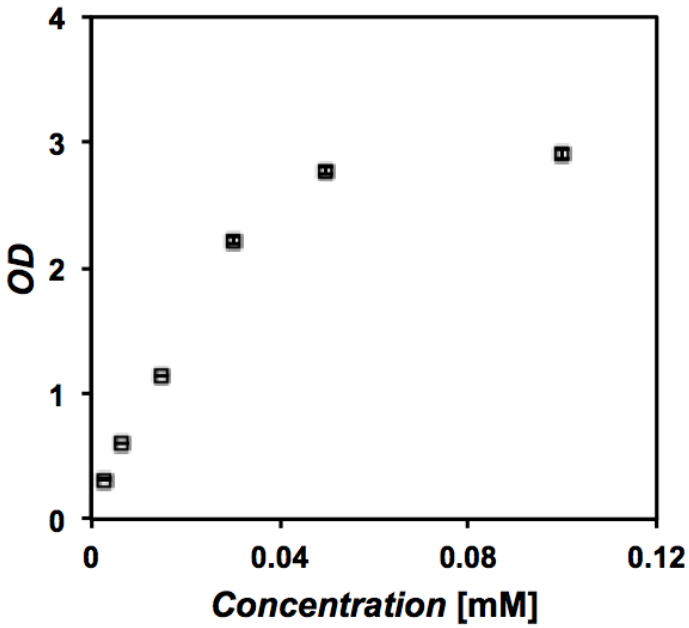

Figure 3.3: Optical density (OD) at a fixed wavelength 665 nm as a function of methylene blue (MB) concentration. OD values are an average over six experiments with error bars that denote 95% confidence intervals.

each experiment by mixing for ∼2 min our ENPs working suspension with a small aliquot of concentrated BH_4 and HEPES solution to reach a final concentration of 10 mM for both reagents. Then, we add a small volume of concentrated dye that provides a final concentration of 40 μM in a 2.5 mL working volume. We continuously monitor the absorbance of our colorimetric assay at the maximum dye's absorbance peak of $\lambda_{max=665nm}$. The concentration of particles reported is the mass of particles per mass of the original sample matrix (*e.g.,* water, lake water, urine, *etc.*) before any necessary dilutions.

Figure 3.4 shows the UV - Vis absorbance spectra of MB – BH_4 solution in the presence of ENPs as a function of wavelength. The absorbance of CADE assay exhibits two main absorption bands, one in the UV region (280 - 295 nm) and other in the visible region (600 - 670 nm) corresponding to (π - π^*) and (n - π^*) respectively. The short wavelength bands with high molecular absorption coefficient values ($log(e) \sim 3.8-4.9$) are due to the ($\pi \leftarrow \pi^*$) transition, while the visible absorption bands ($log(e) \sim$ -44.1 - 5.2) result from the (n $\leftarrow \pi^*$)

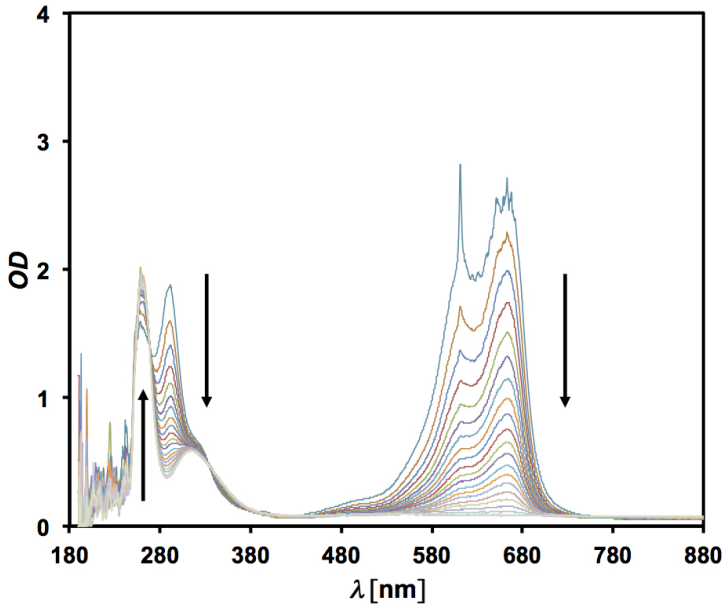

Figure 3.4: Methylene blue (40 μM) and sodium borohydrate (10 mM) absorbance spectra, at 2 s time intervals, in the presence of 5 nm gold nanoparticles coated with tannic acid (Au_{TA}) at a fixed mass concentration of 5 ppb (B). Arrows denote the increasing time.

transition associated with the presence of a $C = S^+$ chromophore group.[156] When 5 nm gold nanoparticles coated with tannic acid (Au_{TA}) are added to solution at the final concentration of 5 ppb, the absorbance decreases with time as MB is reduced, colorless, to leuco-methylene blue (LMB) through a nanoparticle catalytic electron transfer process.[157, 158]. Reduced methylene blue, LMB, exhibits a single peak at ~250 nm that corresponds to the relocation of electrons (*e.g.,* formation of double bonds) in the center ring of MB.[155] We detect the catalytic activity of ENPs by monitoring the optical density (OD) at 665 nm.

3.3.4 CADE Quantification

Figure 3.5 shows OD of CADE solution at 665 nm as a function of time. MB – BH_4 solution in the absence of ENPs has a stable OD of ~2.8 for ~25 s. The stable background indicates that the dye reduction is insignificant when nanoparticles are not in solution. We measured the optical density of dye-reductant for long experimental times, 1 h, in absence

of ENPs for ultra pure water and in complex matrices, and show that OD decreases less than 0.09 over the duration of the experiment (data presented in Figure 3.6).

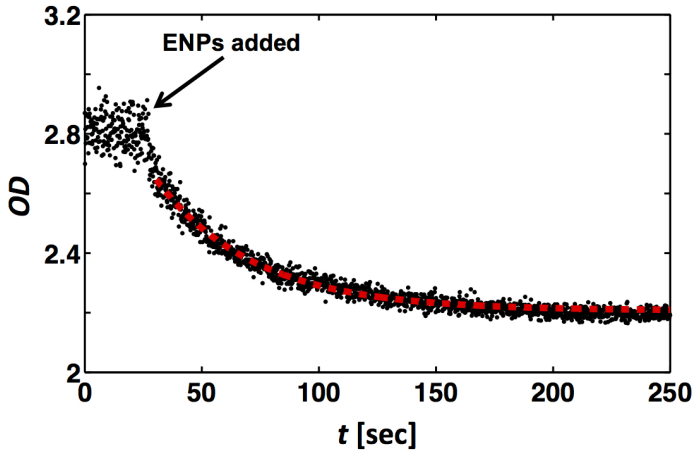

Figure 3.5: Optical density of methylene blue at pH 7.0 (10 mM $NaBH_4$ and 10 mM HEPES) in the presence of 100 nm gold nanoparticles coated with tannic acid (Au_{TA}) at a fixed mass concentration of 300 ppb recorded at 665 nm. Red dash line indicates a fit to an exponential decay model. β is the asymptotic value of the optical density. Nanoparticles are added at t = 28 s causing MB – BH_4 optical density to decrease due to reduction of MB.

After 25 seconds, 100 nm Au_{TA} are added to the solution with a final concentration of 300 ppb which results in an exponential decrease of OD from 2.8 to 2.2 over ∼75 s. Then, the OD plateaus and remains steady for the duration of the experiment. We fit the absorbance as a function of time with an exponential curve, given as,

$$OD = (OD_0 - \beta)exp(-(t/\tau)) + \beta \tag{3.2}$$

where the OD is the optical density of solution, OD_0 is the optical density at $t = 0$, τ is the exponential decay rate constant, t is the time transpired from the addition of the ENP, and β is a constant that represents the asymptotic OD value. OD data processing and analysis was performed by a custom code written in MATLAB, refer to appendix, (MathWorks Inc., Natick, MA). We fit τ and β values (41.8 s and 2.2 for the data shown in Figure 3.5), which respectively represent the decay time at which the dye absorbance is reduced to 1/e of its initial value and the steady state OD that is reached at long times. We explored

the use of a decay rate constant for quantifying the reduction reactions, but ultimately chose β to quantify the presence of ENPs since this asymptotic constant is unbiased from experimental artifacts (*e.g.,* particle diffusion in the solution, formation of hydrogen bubbles, etc). β values have a dynamic range of 0.01 to 2.8 and potentially serve as an ENP surface reactivity indicator. Lower β values correspond to higher ENP surface catalytic activity and higher β values represent lower nanoparticles catalytic activity. We, also, determine the limit of detection (LOD) and limit of quantification (LOQ) for this assay in ultrapure water and in complex matrices. LOD and LOQ definitions and mathematical formulation details can be found in sections below. β, LOD, and LOQ values allowed us to quantitatively compare concentrations, sizes, surface coatings, and core compositions of ENPs in a variety of matrices.

3.4 Physicochemical Properties and ENPs Catalytic Reactivity

3.4.1 CADE Control Analysis

We performed control experiments in absence of ENPs to ensure that the change of optical density (OD) is exclusively attributed to the presence of nanoparticles. Figure 3.6 shows the optical density of CADE solution at $\lambda_{max=665nm}$ as a function of time for ultra pure water, lake water, NOM, serum, and urine. In the case of serum and urine, the sample was diluted 5 and 4 times, respectively, to be able to obtain a measurable signal. MB – BH_4 solution in the absence of ENPs has a stable OD of $\sim$2.8, showing that the color of the dye remains unaltered for 60 min. Results indicate that the dye reduction is insignificant when nanoparticles are not in solution.

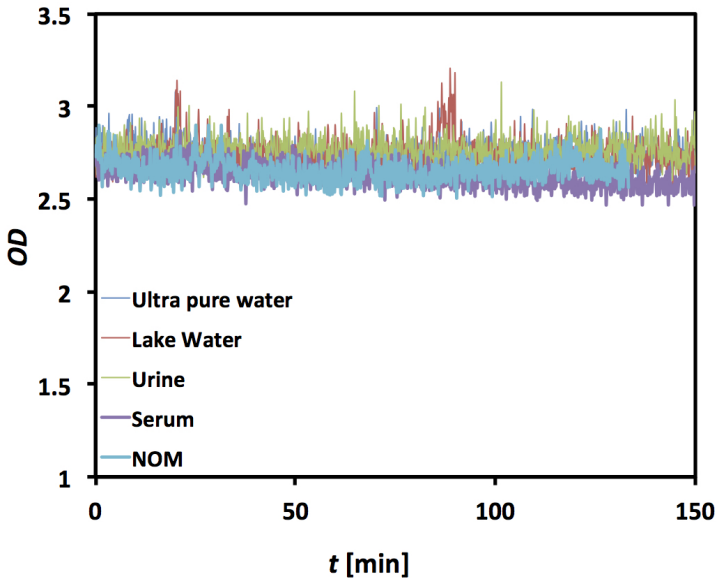

Figure 3.6: Optical density at 665 nm as a function of experimental time for colorimetric assay for ultra pure water, lake water, serum, NOM, and urine in the absence of ENPs.

3.4.2 Verification of ENPs as a Redox Catalysis

Previous studies report that metal nanoparticles can be used as catalysts in electron-transfer reactions and show the mechanism on how ENPs are catalytically active due to the reduction of their electrochemical redox potential, which ultimately enhanced the electron flow from donor species to acceptors.[159, 160, 158, 157] ENPs are important for the mechanistic study of heterogeneous catalysis. We have studied the role of nanoparticles as electron-transfer catalysts and shown, in this chapter, that the catalytic activity of ENPs differ with their intrinsic physicochemical characteristics. Heterogeneous catalytic redox reactions take place at the surface of a ENP where the electron exchange between the particle and the reactants occurs, where the electron transfer occurs from the reducing agent to ENP to the oxidant. A good model reaction for such investigations is the ENP-catalyzed reduction of methylene blue (MB) to leuco methylene blue (LMB) in aqueous solutions in the presence of a reducing agent, as it is shown in Scheme 3.3. We confirmed that ENPs serve as a catalyst on the reduction reaction of MB to LMB by experimentally testing the following characteristics, which are common to must of catalytic reactions: (i) a catalyst remains unchanged at

the end of the reaction, (*ii*) small quantity of the catalyst is sufficient to catalyzes multiple reactions, (*iii*) the function of the catalyst is to alter the reaction kinetics, and (*iv*) catalysts are specific in nature and by changing the catalyst, the nature of products changes.

$$2\,\mathrm{MB} + \mathrm{BH_4} + 2\,\mathrm{H_2O} \underset{k_\mathrm{b}}{\overset{k_\mathrm{f}}{\rightleftharpoons}} 2\,\mathrm{MBH} + \mathrm{BO_2} + 3\,\mathrm{H_2} \tag{3.3}$$

To confirm that ENPs do not go through any major physical or chemical transformations during the catalyzed reduction of methylene blue, we employed electron microscopy, energy-dispersive X-ray spectroscopy (EDX), and dynamic light scattering (DLS) to demonstrate that catalysts are unchanged after the reaction. Bright field transmission electron microscopy (TEM) images were taken on a FEI Tecnai G2 F20 at an accelerating voltage of 200 keV and EDX spectrums were obtained with a 60 second acquisition time. The spectrums were then processed by subtracting the background and smoothing the peaks. The hydrodynamic sizes of ENPs were determined using DLS (NICOMP 380 ZLS, Particle Sizing Systems, Santa Barbara, CA) that uses laser light at 635 nm. The measurements were made under a scattering angle of 90° at 23 °C and all ENP's sizes are reported as intensity-weighted sizes.

Figure 3.7 shows bright field TEM micrographs and EDX analysis of ENPs pre and post reaction of 20 nm gold nanoparticles coated with tannic acid (Au_{TA}) and 20 nm silver nanoparticles coated with tween-20 (Ag_{TW20}). Micrographs reveal that morphology of Au_{TA} and Ag_{TW20} do not change after serving as a catalyst in the reduction of MB to LMB. Similarly EDX spectra, Figure 3.7B, D, F and H, reflect that the elemental composition of Au_{TA} and Ag_{TW20} is constant throughout the catalytic reaction, showing strong gold or silver with carbon and copper peaks originating from ENPs and the lacey carbon, TEM grid used for these analysis, respectively. A sodium peak is also observed in the post-reaction spectrums of both ENPs, Figure 3.7D and H, which could be attributed to the presence of the reducing agent ($\mathrm{NaBH_4}$) in the reaction. Additionally, we investigated the stability of ENPs in the CADE assay by measuring the hydrodynamic size of 20 nm gold nanoparticles

coated with branched polyethylenimine (Au_{BPEI}), as a surrogate particle, over a 60 min experimental time via DLS (refer to Figure 3.8). An analysis of variance (ANOVA) and subsequent comparison of means test (Tukey HSD) showed that particle diameter in the presence of the CADE assay at different experimental times does not differed significantly from the stock solution (control) at an $\alpha = 0.05$ level. Combined TEM, EDX and DSL analyse show that ENPs do not go through any major physicochemical transformations after serving as a catalysis for the reduction of MB.

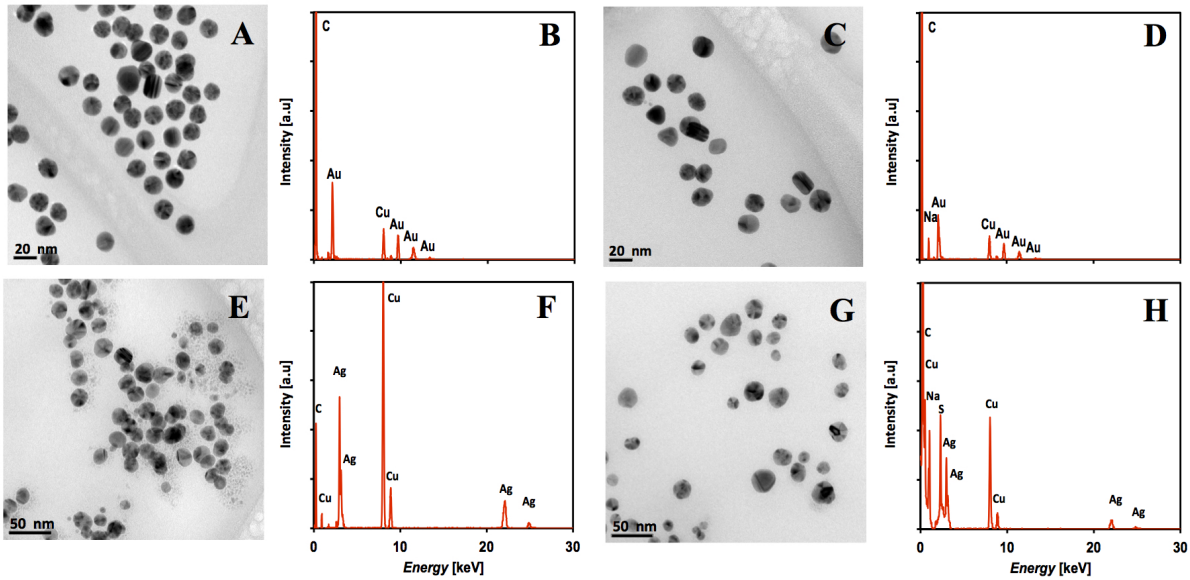

Figure 3.7: Bright field TEM micrographs and EDX spectra of 20 nm gold nanoparticles coated with tannic acid (A, B) before, (C, D) after reaction and 20 nm silver nanoparticles (E,F) before, (G,H) after reaction with the CADE assay at a fixed mass concentration of 20 ppm.

We, also, confirm that small quantities of ENPs are sufficient to catalyze multiple reactions (reduction of MB to LMB). Figure 3.9 presents the optical density of the colorimetric assay in presence of 20 nm Au_{TA} at a fixed mass concentration of 1 ppm. Data shows that when Au_{TA} are added, at 35 s, the dye's optical density rapidly drops to $\sim$0. Then, a fresh solution of MB, final concentration of 40 μM, is introduced resulting in immediate increase in the optical density and subsequent decrease. This behavior is observed multiples times,

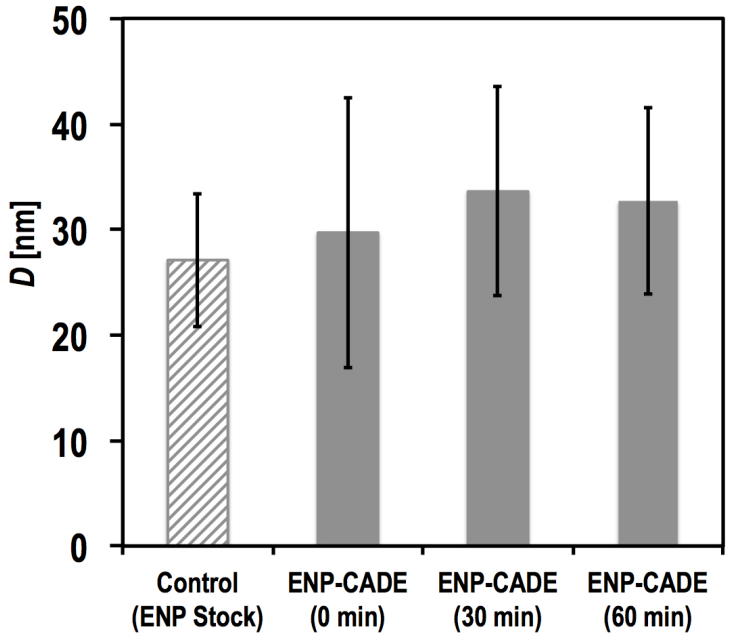

Figure 3.8: Hydrodynamic diameter of 20 nm gold nanoparticles coated with branched polyethylenimine in the presence of the CADE assay showing particle stability over a 60 min experimental time.

(15), proving that the reduction of dye occurs by the presence of ENPs in the solution and that nanoparticles are not being consumed in the electron-transfer reaction.

Furthermore, we verify that the main function of ENPs is to alter the reaction kinetics in the reduction of MB by recording the optical density as a function of experimental time in the presence or absence of nanoparticles. As we described previously, the *OD* of the dye remains unchanged for at least for ∼2 h in the absence of ENPs, indicating that the dye reduction, if it occurs at all, is insignificant (refer to Figure 3.6). The dye reduction occurs very quickly in the presence of ENPs. UV-visible spectra of the CADE assay in the presence of ENPs (Figures 3.4 and 3.5) shows that the color of the dye gradually vanished, which was observed by the gradual decrease in the absorbance value at the dye $\lambda_{max} = 665$ nm. To ensure that the nanoparticles presented in this work do not interfere with the dye's spectrum, we measured the *OD* as a function of wavelength for all ENPs, even at higher concentrations normally used in our experiments (18 ppm), as presented in Figure 3.10. Data shows that ENPs plasmon bands do not overlap with CADEs recordings at λ_{max}. In addition,

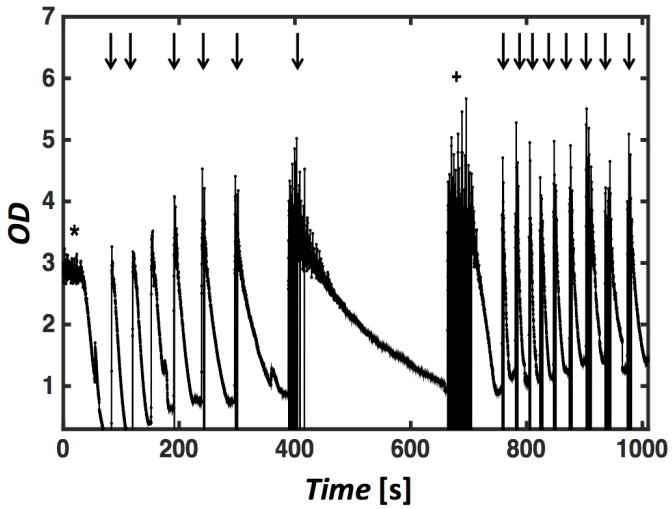

Figure 3.9: Optical density at 665 nm for the reduction of Methylene Blue at pH 7.0 (10 mM $NaBH_4$ 10mM HEPES) in the presence of 20 nm gold nanoparticles coated with tannic acid at 1 ppm showing the catalytic activity of ENPs on dye reduction. The asterisk corresponds to the time when gold nanoparticles were added to the detection solution, downward-pointing arrows denote when 40 μM of MB is added, and the plus sign shows the time when 10 mM of $NaBH_4$ is added.

previous studies reported that the reduction of MB to LMB is thermodynamically favorable but kinetically unfavorable, [133, 134, 135] confirming that ENPs serve as a catalyst in the electron-transfer reaction by altering the kinetics in the reduction of MB.

We, also, investigated the effect of pH on the CADE assay by testing the ENPs' catalytic activity in multiple buffering agents. The reduction of MB was studied in a range of pH values (2.5 - 9.9) and multiple buffers (*e.g.,* citric acid, bis - tris, tris, and boric acid) in the absence or presence of 5 nm gold nanoparticles coated with tannic acid (Au_{TA}) at a fixed mass concentration of 1 ppm. Figure 3.11 shows the *OD* as a function of experimental time in the CADE assay buffered by citric acid at pH 2.5 (A), bis-tris at pH 5.5 (B), tris at pH 8.9 (C), boric acid at pH 9.9 (D), and HEPES at pH 6.9 (E) with a fixed ionic strength of 10 mM for all buffering agents. In all cases, the maximum catalytic efficiency of ENPs was obtained with HEPES buffer at pH 6.9, which allows the complete reduction of MB and lower β-values. The 10 mM of HEPES buffer had sufficient buffering capacity without inducing particle instability (*i.e.,* aggregation due to reduction in electric double layer thickness as

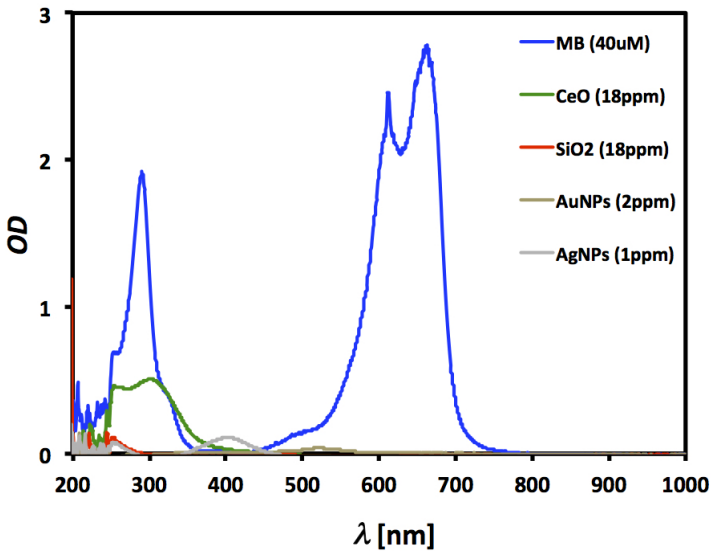

Figure 3.10: Optical density as a function of wavelength of methylene blue at the same concentrations use in the CADE assay and ENPs tested in this work.

a result of high ionic strength) and minimizes the dye oxidation (k_b), which is a common reaction mechanism when reduced MB is in presence of oxygen.[154, 155] Wang *et al.* shows that the surface of ENPs can be modified in acidic solutions to a more positively ζ potential and a reverse effect in alkaline solutions that ultimately enhance or impede the reduction reaction of catatonic dyes by ENPs.[161] As a result, it is not surprising to observe an increase in the adsorption of MB molecules on the surface of ENPs in neutral or alkaline solutions and thus the increase in the dye reduction efficiency. This study confirms the validity of our experimental results as well as the selection of 10 mM HEPES as our buffering agent.

Similarly, we analyze the effect of pH on the β-values as it is shown in Figure 3.11F. The β-values presented here are an average over four experiments with error bars that denote 95% confidence intervals. At low pH (2.5), the β-value is 2.68, which correlates to a minimal reduction of MB (*e.g.,* low catalytic activity of ENPs). This effect could be attributed to the small adsorption of cationic dye-molecules on the surface of the particle since ENPs' surface charge is shifted to a partially net positive that can create repulsive forces between the particles and MB (cationic dye), which will decreased the reduction of MB. Thus, the degradation efficiency will be decreased in acidic pHs. On the other hand, at higher pH,

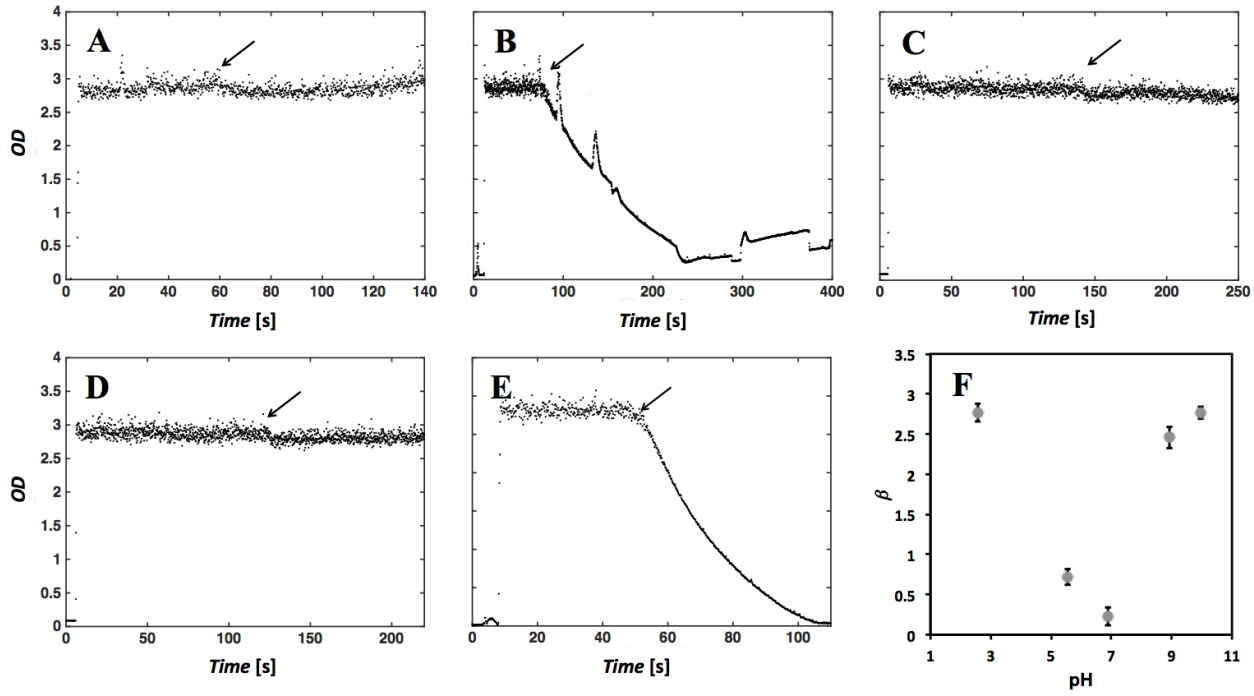

Figure 3.11: Optical density of the CADE assay buffered with citric acid at pH 2.5 (A), bis-tris at pH 5.5 (B), tris at pH 8.9 (C), boric acid at pH 9.9 (D), and HEPES at pH 6.9 (E) with a fixed ionic strength of 10 mM for all buffering agents. The downward-pointing arrows denote when 1 ppm of gold nanoparticles coated with tannic acid (Au_{TA}) are added. The β-values extracted from *OD* spectrums as a function of buffer pH for Au_{TA} are presented in (F). β-values are an average over four experiments with error bars that denote 95% confidence intervals.

8.9 and 9.9, there is an excess of hydroxyl ions that could potentially compete with dye molecules in adsorption process on the surface of ENPs and finally inhibit the reduction of MB (*e.g.,* higher β-values). Overall, our data reveal that ENPs serve as a catalyst in the electron-transfer reduction of MB to LMB where the particles do not go through any major physicochemical changes during this process, small amounts (ppb level) of ENPs was sufficient to catalyzed multiple reactions (over 14), and nanoparticles enhance the kinetics of the reduction of the dye while controlling the rate constants by fixing assays' pH.

3.4.3 Role of ENP Concentration, Size, and Surface Area

The reduction of MB by borohydride depends directly on the concentration of nanoparticles. Figure 3.12 shows the dependence of the measured β values on the ENPs mass concentration for 5 nm Au_{TA}. All β values are reported herein as the mean of at least four experimental measurements with error bars that denote the 95% confident intervals (α = 0.05). In the absence of nanoparticles in the MB – BH_4 solution, the β value is ~2.8, representing the highest absorbance of dye solution. β values decrease as ENPs' mass concentration (mass of particle per volume) increases. Mass concentration should directly correlate with the reduction of the dye's absorbance since the number of metal particles, and their surface area, available to serve as an electron relay between MB and BH_4 increases as particle concentration increases. At 325 ppb or higher concentrations of Au_{TA} the β approaches zero suggesting a complete reduction of the MB. The limit of detection (LOD) of 5 nm Au_{TA} in buffered water is 89 ppb with a 95% confidence level.

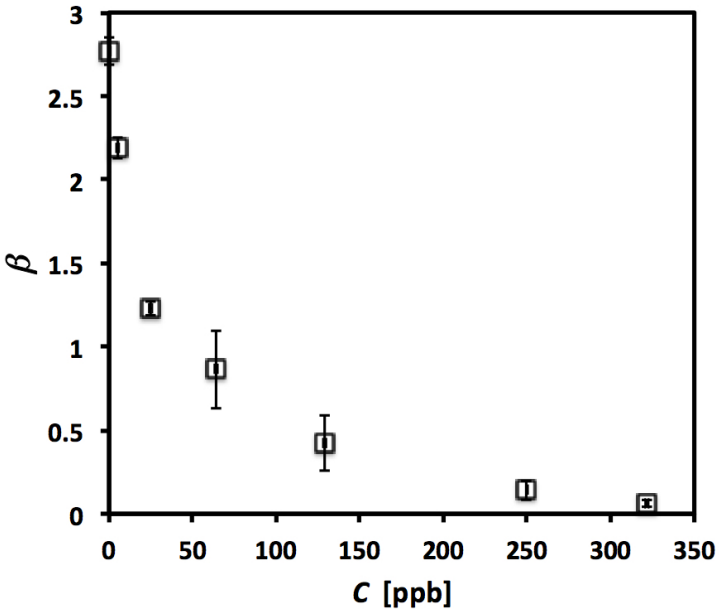

Figure 3.12: β-values as a function of gold nanoparticle concentration, C, coated with tannic acid at a diameter of 5 nm. Each experimental value represents the mean value from a set of four experiments with error bars that correspond to 95% confidence intervals.

We studied the dependence of dye absorbance on ENP size and surface area. Figure 3.13A shows β values as a function of particle size for Au_{TA} for three different constant surface areas 0.1, 0.2, and 0.5 cm^2. The average β values decrease with increasing surface area because higher surface area provides more surface sites for the electron transfer from reducing agent to the dye.[162, 163, 164, 133] For constant surface area, β increases rapidly as particle size increases until it reaches 20 nm and then remains nearly constant for larger diameters. Previous studies have shown that the redox potential of particles decrease as a function of radius which would result in an increase the electron relay of the MB – BH_4 and lower effective β values. [134, 133, 165]

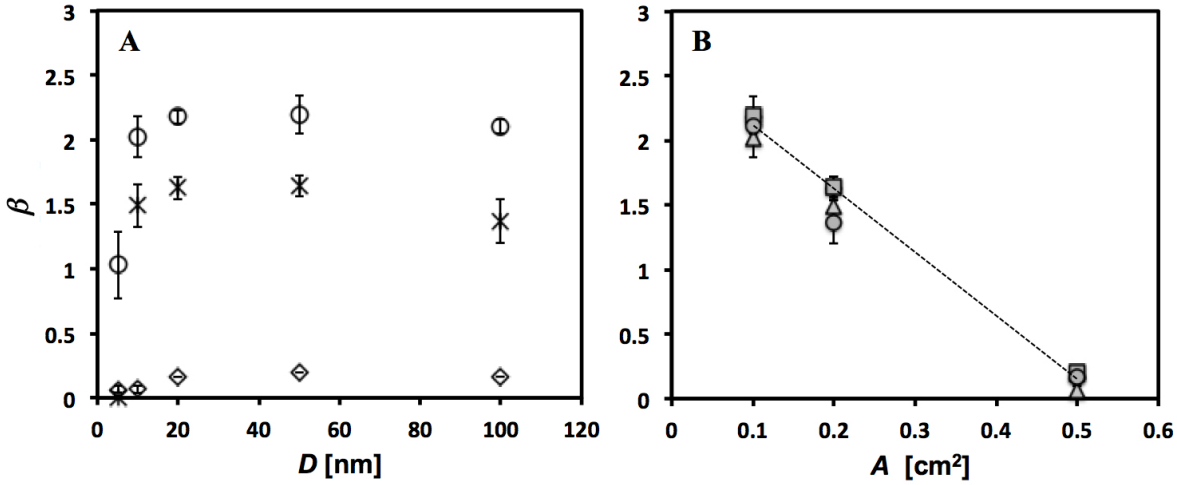

Figure 3.13: (A) Plot of β values as a function of Au_{TA} diameter at a surface area of 0.5 ($\diamond$), 0.2 ($\times$), and 0.1 cm2 ($\circ$) at fixed ENP mass concentration. (B) Plot of β values as a function of Au_{TA} surface area at 10 (triangles), 20 (diamonds), 50 (squares), and 100 nm (circles) particle diameters. All values represent the mean value of four experiments with error bars that correspond to 95% confidence intervals.

Figure 3.13B shows β as a function of nanoparticle surface area for 10, 20, 50, and 100 nm Au_{TA}. By increasing ENP surface area, β values decrease linearly. We expect this linear trend because redox reaction rates (*e.g.,* MB to LMB), can be predicted by the Butler-Volmer equation in the Tafel regime,[166] expressed as,

$$J = \frac{Ai_0}{zF} exp((anF/RT)(E - E_0)) \tag{3.4}$$

where A is the total surface area of all ENPs in the system, z is the valence electrons of the reacting species, α is the charge transfer coefficient, n is the number of electrons in the charge transfer process, i_0 is the exchange current density that is specific for the reaction (dye - ENP pair), E is the electrical potential of NPs, and E_0 is the equilibrium potential for the redox reaction. This equation indicates that reaction rate depends linearly on the surface area, A, and implicitly on particle composition, through i_0 and E_0.[136] i_0 and E_0 are constant for a specific redox reaction and are determined by the dye and ENP used in the system. The equilibrium potential depends on the difference between the reduction potential of the nanoparticle and the dye. Since MB has a constant reduction potential at constant pH, the rate is determined by the reduction potential of the particle. For each ENP and redox chemistry, i_0 and E_0 are constant. From this equation, we gain an intuition about how the particle concentration, size, and composition impact the reaction rate.

3.4.4 Role of Capping Agents and ENPs Core Composition

ENPs are frequently functionalized with a variety of materials such as synthetic polymers, biopolymers, dendrimers, or other small molecules to provide stability, biocompatibility, and functionality. In addition, these functional groups may facilitate or impede the electron transfer mechanism at the nanoparticle's surface. Figure 3.14 shows β values for 20 nm Au nanoparticles as a function of capping agents at a constant particle concentration of 500 ppb. The β values range from 2.25 for Au_{PEG} to 0.18 for Au_{BPEI}. Lower β values correspond to higher ENPs catalytic activity. At fixed ENP diameter and core composition, the surface charge of nanoparticles has a high influence on the catalytic reactivity of ENPs. Positively charged ENPs possess higher reactivity than negatively charged particles. We believe positively charged particles (Au_{BPEI}), with a surface charge of $+29.6 \pm 17.6$ mV, may electrostatically attract $NaBH_4$ molecules to the surface of the particle, which then enhances the reduction of MB, resulting in low β values. In contrast, we observe less dye reduction (high β values) on negatively charged particle surfaces, such as that for PVP

and TA (-33.5 ± 18.9 and -16.3 ± 8.9 mV, respectively). The inhibition of MB reduction when ENPs have a negatively charged surface coating might be explained by an electrostatic repulsion between functional groups and BH_4 molecules. According to Jiang *et al.* and Azad *et al.*, when BH_4 absorbs to the surface of ENPs, it creates a negatively charged layer that attracts cationic organic dyes, such as MB. This electrostatic attraction between the cationic dye and the reducing agents increase the reduction rate of MB.[167, 168]

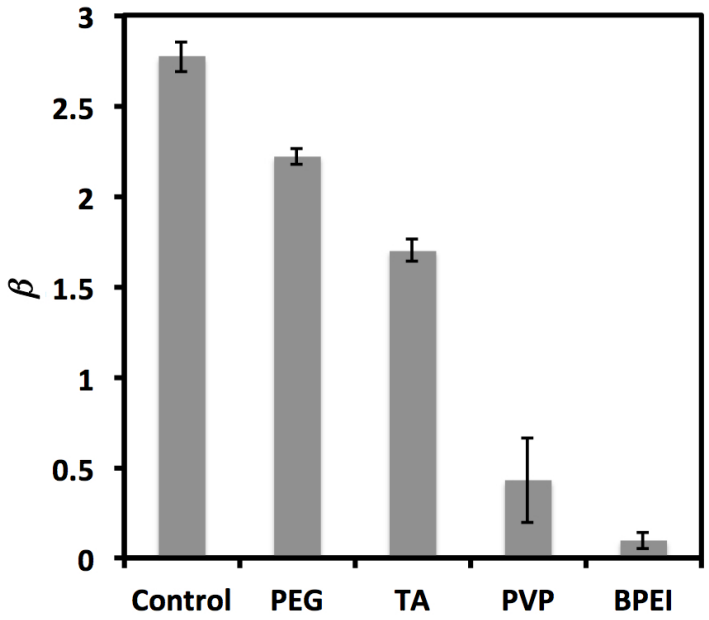

Figure 3.14: β-values as a function of ENPs capping agent at a fix ENP diameter of 20 nm and 500 ppb mass concentration of gold nanoparticles. Control experiments correlate to absence of ENPs in the assay. β-values are an average over four experiments with error bars that denote 95% confidence intervals.

To further understand the effect of dye reduction due to particles' capping agents, we also consider the molecular weight of the synthetic polymers. Figure 3.14 shows that β values decrease as molecular weight increases for the ENPs' capping agents. BPEI, PVP, and PEG have molecular weights of 25, 10, and 5 kDa, respectively. Since the electron transfer between MB and BH_4 occurs at the surface of ENP, we hypothesize that low molecular weight polymers will inhibit the reduction process of MB (high β values) by creating a steric repulsion between the dye and reducing agent at the particle surface. This repulsion is

likely due to low molecular weight coatings having a larger fractional polymeric coverage on nanoparticles, creating a barrier to large molecules, such as MB, to ENPs surfaces.[169] In order to confirm that the reduction of MB is directly correlated with the presence of ENPs and not due to the particle capping polymers and molecules, we decouple both components and test them separately. Figure 3.15 shows *OD* spectra of PVP, TA, and BPEI, at a fixed mass concentration of 100 ppm, Au_{PVP}, Au_{TA}, and Au_{BPEI}, at a fixed mass concentration of 1 ppm, as well as β-values as function of capping agents and metal (Au and Ag) nanoparticles coated with PVP, TA, and BPEI. Altogether, data suggest that all functional groups (*e.g.,* PVP, TA, and BPEI) do not create any interference on the reduction of MB to LMB, even when two order of magnitude of higher concentration (100 ppm) is added to the assay compared to 1 ppm for the case of ENPs, proving that the electron - transfer from the donor to the acceptor only occurs when particles are presence in the system.

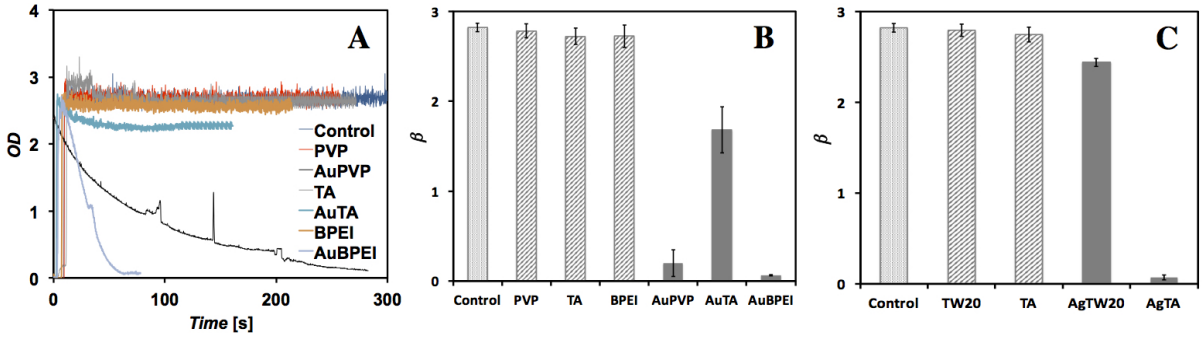

Figure 3.15: Optical density spectra of CADE assay in the presence of polyethylene glycol (PVP), tannic acid (TA), branched polyethylenimine (BPEI), and 20 nm gold nanoparticles coated with PVP (Au_{PVP}), TA (Au_{TA}), and BPEI (Au_{BPEI}) at a fixed mass concentration of 100 ppm for capping agents and 1 ppm for gold nanoparticles (A). β-values as function of capping agent and gold nanoparticles coated with PVP, TA, and BPEI (B) and silver nanoparticles coated with tween20 (Ag_{TW20}) and TA (C). Control experiments correspond to the absence of ENPs. β-values are an average over five experiments with error bars that denote 95% confidence intervals.

Taken together particle surface charge and molecular weight, β values are likely to decrease (more reactive) when particle surface charge has net positive value and when molecular weight of the capping agent increases. Recent studies suggest that the hydrophobicity of the dye, complex formation of the dye with anionic surfactants, repulsion between the dye and

charged surfactants, may also impact the catalytic reactivity of the ENPs, these factors should to be considered for future CADE's experimental procedures.[168, 170, 171]

We, also, examine the surface catalytic reactivity of ENPs over a range of particle compositions. The quantitative comparison of the catalytic activity of different nanoparticles is challenging since the reduction of MB in our assay is proportional to ENP size, core composition, surface coatings, *etc.* Here, we provide a single-value to compare different ENP core compositions and sizes that can potentially be used as a screen tool for the assessment (presence / absence) of nanoparticles in systems with multiple nanoparticles types. $C_\beta = 2$ is the concentration of ENPs (ppm) needed to decrease the *OD* of the solution to 2 (*i.e.,* β value of 2). An *OD* of 2 represents a change in absorbance greater than 10 standard deviations of the background experiments.

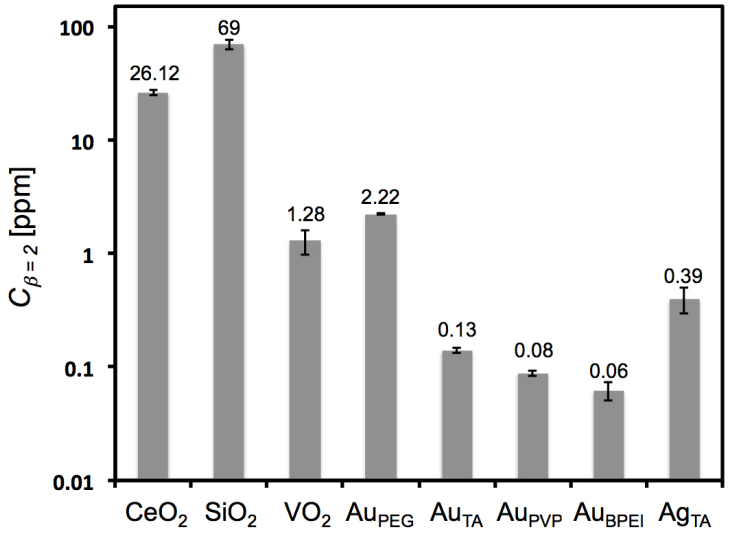

Figure 3.16: ENPs concentration needed to reach a β value of 2 as a function of particle core composition and surface coating. Concentration values were extracted from a set of four experiments and shown as a mean value, exact values shown above each bar, with error bars that represent 95% confidence intervals.

Figure 3.16 shows $C_\beta = 2$ for commercially available particles with various core compositions, particle diameters, and surface coatings. $C_\beta = 2$ for metal nanoparticles (*e.g.,* Au and Ag) ranges from 80 ppb to 4 ppm depending on core composition and particle surface functionally. Similarly, we are able to detect oxide nanoparticles (*e.g.,* CeO_2, SiO_2, VO_2) in

the range of 2 ppm to 90 ppm. The data suggests that the concentration needed to reduce dye-reductant solution is lower for elemental metal ENPs than oxides nanoparticles, which indicates that Au and Ag ENPs have a higher catalytic activity than oxide ones. The electron transfer, BH_4 to MB, may have a higher rate for metal ENPs since this set of nanoparticles has higher electron conductivity than metal oxides. Our results suggest CeO_2 and SiO_2 can transfer electrons from BH_4 to MB similar to TiO_2 (5 nm) and ZnO (6 nm) which have been shown to transfer electrons to organic radicals, like MB. [172]

Despite the differences in the core composition, particle diameter, and surface functionality, the CADE assay is able to assess the catalytic activity of NPs in concentrations (80 ppb to 90 ppm) typically used in environmental exposures models and measurements for nanomaterials hazard studies.[173] While we expect that oxide particles will show lower catalytic activity than metallic ones, more data is needed to explicitly detail the role of the composition and surface coatings. This work represents a step towards the development of sensitive and reliable methodology to detect a variety of ENPs.

3.4.5 Detection of ENPs in Biological and Environmental Matrices

Most analytical methods used for detecting and quantifying ENPs in complex samples require careful sample preparation such as extraction, digestion, or sample fixation. Here we examine the sensitivity and efficacy of our colorimetric detection assay, CADE, by determining limit of detection (LOD) and limit of quantification (LOQ) values in complex environmental and biological media. LOD and LOQ were extracted from standard errors of the response and the slope values from calibration curves.[174, 175] Figure 3.17 shows calibrations curves of 20 nm Au_{TA} in ultra pure water, lake water, NOM, urine, and serum. Each experimental point represents the mean value from a set of a minimum of 3 experiments

with error bars that represent 95% confidence intervals. LOD and LOQ are defined as,

$$LOD = \frac{3(\sigma_{SE})}{|m|}\,[ppb] \tag{3.5}$$

$$LOQ = \frac{10(\sigma_{SE})}{|m|}\,[ppb] \tag{3.6}$$

$$\sigma_{SE} = \sqrt{\frac{\sum(y-\overline{y})^2}{n-2}} \tag{3.7}$$

Where σ_{SE} is the standard error, m is the slope of the linear fit [ppb^{-1}], n is the number of data points, y and $\overline{y}$ are the actual and predicted values respectively.

In the case of urine and serum, samples were diluted 4 and 5 times, respectively, to obtain a detectable signal. We report the concentration of the original suspension. In Table 3.4, we present LOD and LOQ values for 20 nm Au_{TA} in ultra pure water, environmental (*e.g.,* lake water, NOM) and biological matrices (*e.g.,* artificial urine, mouse serum).

Table 3.4: Detection limit values for 20 nm gold nanoparticles coated with tannic acid in complex matrices

Matrix	LOD [ppm]	LOQ [ppm]
Lake water	0.157	0.526
Ultra pure water	0.303	1.012
NOM	04.60	1.536
Serum	1.536	5.131
Urine	1.759	5.864

For the case of gold nanoparticles, the LOD ranges from 0.15 to 1.75 ppm depending on the matrix. The highest LOD values were observed for urine and serum at 1.75 and 1.53 ppm, respectively. Similarly, we have tested high nanoparticle concentrations, $>$ 60 ppm, that provided a complete reduction of the dye indicating that higher concentrations of ENPs will lead to a β value of zero. Urine has an ionic strength of $\sim$ 170 mM and conductivity of 6.6 mS cm^{-1}, which may reduce the catalytic activity of ENPs by inducing particle aggregation. In the case of serum, the absorption of proteins and other biomolecules to the surface of the

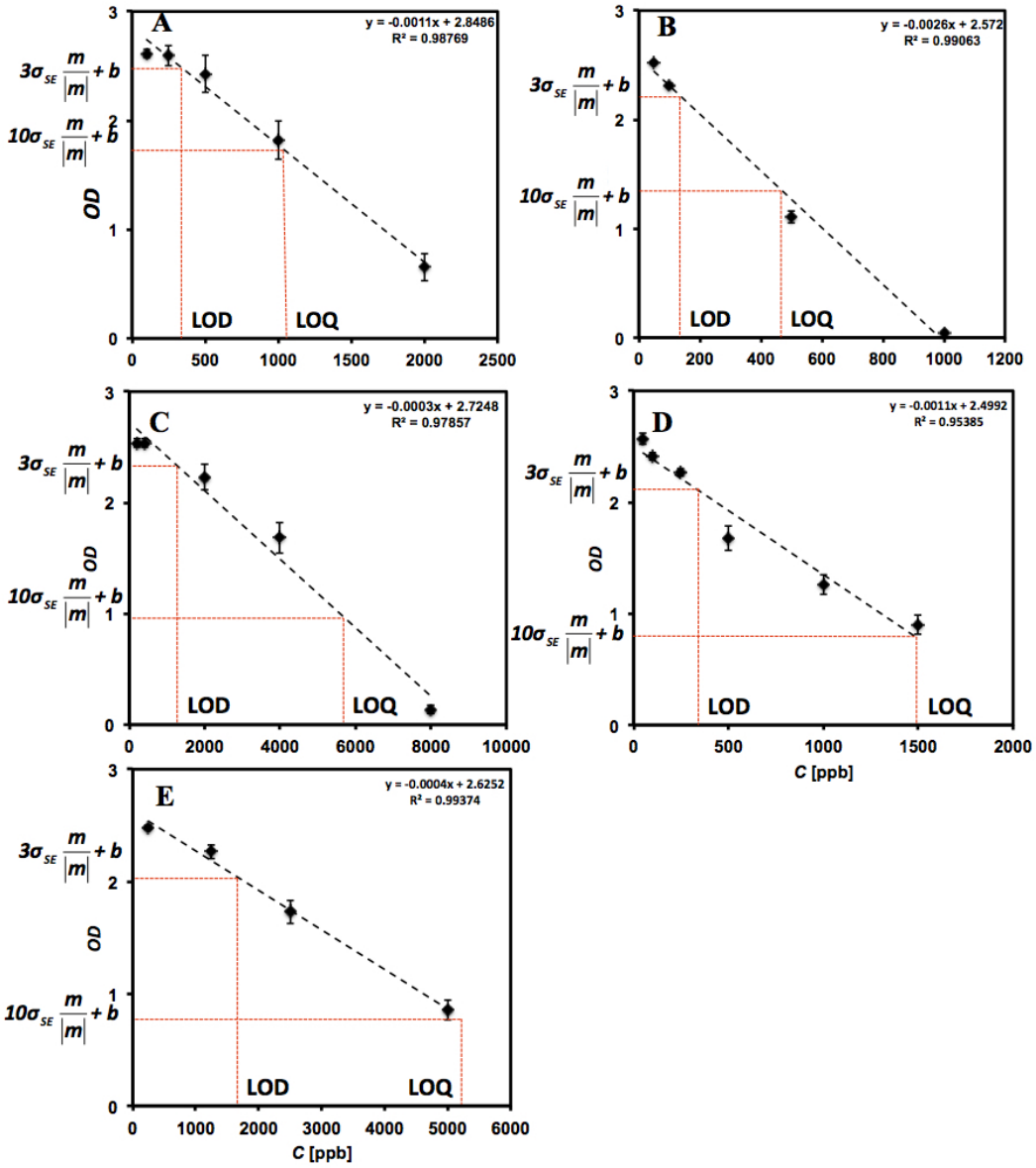

Figure 3.17: Calibration curves showing optical density as a function of 20 nm gold nanoparticles coated with tannic acid in ultrapure water (A), lake water (B), urine (C), NOM (D), and serum (E). Each experimental point represents the mean value from a set of a minimum of 3 experiments with error bars that represent 95% confidence intervals. Assay sensitivity values are shown by red dotted lines as limit of detection (LOD) and limit of quantification (LOQ).

particles may inhibit the catalytic activity of particles by creating proteins coronas that will obstruct the area where dye reduction take place.[176, 66] For NOM and lake water, the LOD values were one order of magnitude lower than serum and urine. These data suggest that the catalytic assay proposed here to detect ENPs in biological and environmental matrices as well as ultra pure water is sensitive, simple and does not require complex instrumentation.

3.4.6 Assessing ENPs from Commercial Products

Engineered nanoparticles have unique and desirable functional properties that can be potentially employed in a wide range of commercial applications. Silver is one of the most widely used metals for the fabrication of ENPs due to its simple and well understood synthesis as well as for its antibacterial properties.[177] Silver ENPs have found a diverse set of applications in consumer goods including appliances, automotive, electronics, food and beverage, goods for children, food storage containers, and wound dressings.[36, 178, 179] It is estimated that silver nanoparticles production in United States is between 2.8 to 20 tons per year and that approximately 25% of nano-enable commercial products contain Ag.[44, 28] The greatest number of commercial products that contained Ag nanoproducts is health and fitness, which includes Ag-enabled textiles (Ag_{ENP} textiles).[180] These textiles include, but are not limited to, shirts, pants, socks, underwear, and linens. Manufacturers of silver-enabled textiles claim that due to the reduction of odor from the antibacterial properties of Ag ENPs, their products will require less laundering than conventional alternatives, which will lead to a reduction in use-phase environmental impacts.[180, 7] However, to date, there is no published research confirming changes in consumer laundering behavior. Increased use of Ag ENPs in consumer goods will drive the release of silver nanomaterials into the environment.[144, 181]

Some industrial processes also use large quantities of engineered nanoparticles in ways that do not directly end up in consumer products but which nonetheless require appropriate handling and environmental controls to assure that they do not pose workplace and/or

environmental risks. Alumina (Al_2O_3), ceria (CeO_2), and silica (SiO_2) represent important classes of ENPs.[21] One principal use of Al_2O_3, CeO_2, and amorphous SiO_2 nanoparticles is the chemical mechanical planarization (CMP) process where particles in the form of abrasive slurries are used to polish wafers when fabricating integrated circuits in the semiconductor industry.[182, 183, 184] In this application, the ENPs are used to manufacture the product (semiconductor chips), but are not incorporated into the product. The fate and transport of ENPs from commercial products and in industrial applications as well as their interaction with biological systems is a current necessity to determine if any environmental toxicity will occur after accidental or incidental release of these materials.

We employ the CADE assay to assess the catalytic activity of ENPs from commercially available products and ENPs used in industrial processes. The assessment of surface catalytic activity of nanoparticles will ultimately assist us in determining the presence or absence of these nanoproducts. We focussed on Ag_{ENP} textiles and CMPs slurries (c-SiO_2 and f-SiO_2) since these two commercial products have high production volumes and they can be currently found in the market place.[184, 180, 177] For the case of silver textiles, we used commercially available textiles containing silver nanoparticles coated with tween-20 (Ag_{TW20}) on polyester fabric (CAS: ACSS062720142T1, Dune Science, Eugene, OR) and two textiles containing silver salts; Xstatic (Noble Biomaterials, Scranton, PA) and Polygiene (Polygiene AB, Malmo, Sweden). Textiles containing Ag_{TW20} have an NS20D antimicrobial coating (Dune Sciences) applied to finished t-shirts at a loading of 20 - 30 ppm Ag_{TW20}. The fabric used by Dune Sciences is an Asics Men's Core Short Sleeve Top, new blue color, 100% polyester mesh. Ag_{TW20} particles are either covalently linked to the surface with Dune Science's cross linking chemistry (LinkedON) or in absence of this covalent linker (UnlinkedON). Shirts were treated and rinsed prior to shipment by the manufacturer but not laundered with detergent to preserve nanoparticle loading to the textile. For Xstatic and Polygiene textiles, they were used as received.

Prior to assessing the capabilities of CADE to determine surface catalytic activity of Ag ENP extracted from commercial products, we characterized particle morphology and stability in working solutions via DLS and TEM. We compared results to silver nanoparticles coated with tannic acid (Ag_{TA}), as a control particle, purchased from nanoCompsix (San Diego, CA). Table 3.5 shows characterization data of silver nanoparticles (*e.g.,* Ag_{TW20} and Ag_{TA}) used in this analysis. Hydrodynamic sizes and zeta potentials of particles are reported herein as means of triplicate measurements. Data shows that Ag_{TW20} and Ag_{TA} have similar sizes ($\sim$20 nm) and surface charge ($\sim$17 mV). We also determine particle stability as a function of buffer acidity for Ag_{TW20}, refer to Figure 3.18C. Stability analysis shows that silver nanoparticles coated with tween-20 have higher surface charge in basic solutions (pH > 7).

Table 3.5: Hydrodynamic diameter, particle size, and surface charge of nanoparticles. Measurements in solution chemistry that we used in experimental procedures (*i.e.,* pH = 7.0, 10 mM HEPES)

ENP	TEM Reported Size [nm]	Hydrodynamic Diameter [nm]	Zeta Potential [mV]
Ag_{TW20}	20 $\pm$ 7	36.4 $\pm$ 13	-15.6 $\pm$ 0.6
Ag_{TA}	21 $\pm$ 4	18.5 $\pm$ 5	-18.3 $\pm$ 3.3

We investigated the effect of the CADE assay on particle morphology and surface composition for Ag_{TW20} and Ag_{TA}. Figure 3.19 shows bright field TEM micrographs and EDX analysis of silver ENPs pre and post reaction with our developed assay. Micrographs reveal that the morphology of Ag_{TW20} and Ag_{TA} is not alter after serving as a catalyst in the CADE assay. Similarly EDX spectra, Figure 3.19B, D, F and H, reveal that the elemental composition of Ag_{TW20} and Ag_{TA} is constant throughout the catalytic reaction, showing strong silver with carbon and copper peaks originating from ENPs and the lacey carbon grid, respectively. A sodium peak is also observed in the post-reaction spectrums of both silver particles, which could be attributed to the presence of the reducing agent ($NaBH_4$) in the reaction.

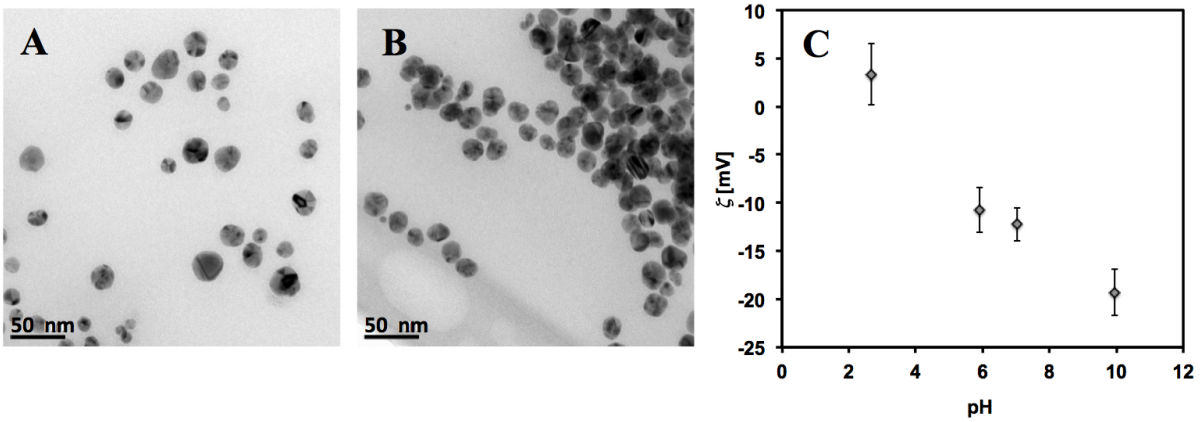

Figure 3.18: TEM micrographs of 20 nm silver particles coated with tween-20 (Ag_{TW20}) and tannic acid (Ag_{TA}) that supports the data in Table 3.5 (A,B) and particle surface charge as a function of buffer pH at a fixed particle concentration of 10 ppm and ionic strength of 10 mM (C). Each experimental value represents the mean value from a set of four experiments with error bars that correspond to 95% confidence intervals.

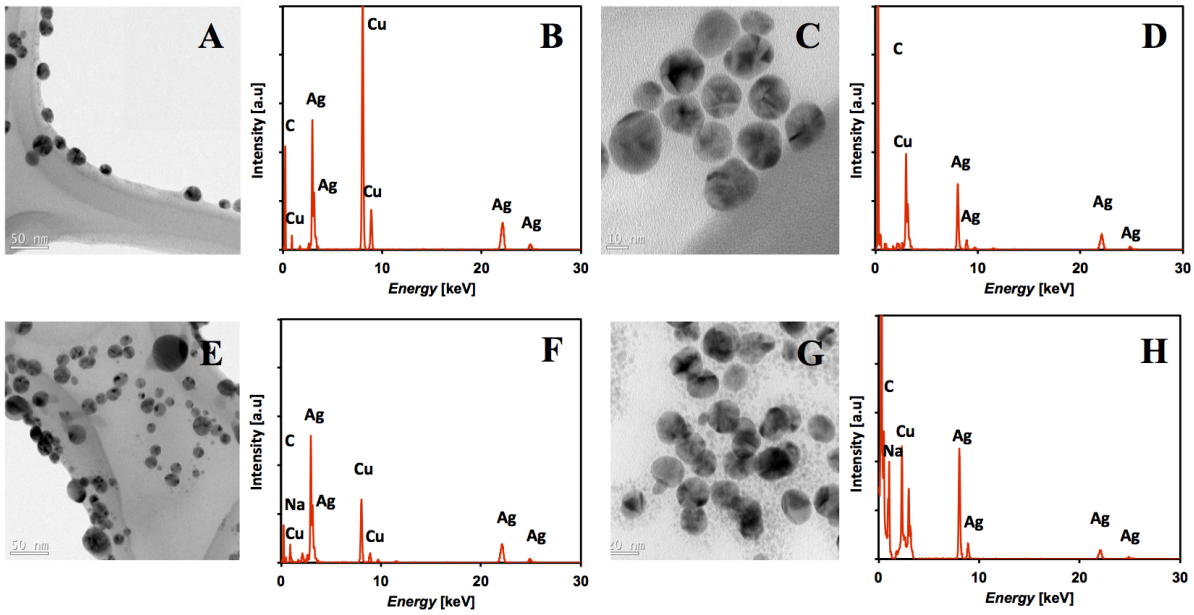

Figure 3.19: Bright field TEM micrographs and EDX spectra of 20 nm silver nanoparticles coated with tween-20 (A, B) before, (E, F) after reaction and 20 nm silver nanoparticles coated with tannic acid (C,D) before, (G,H) after reaction with the CADE assay at a fixed mass concentration of 20 ppm.

We determined the catalytic activity of Ag_{TW20} and Ag_{TA} using CADE. Figure 3.20 presents the optical density (OD) of CADE in the absence (control) and presence of Ag_{TW20} and Ag_{TA} at a fixed mass concentration of 500 ppb. Data shows that OD decreases as ENPs are introduced to the CADE assay at $t = 15$ s. Proving that ENPs serve as a catalyst for the reduction of MB to LMB and that CADE can be potentially used as an assay to detect for Ag ENPs extracted from commercial products. At fixed concentration, Ag_{TA} appears to have the higher catalytic activity compared to Ag_{TW20}, which could be attributed to the effect of coverage by capping agents (*e.g.,* tween-20, tannic acid) as it is described in previous sections. In addition, we examined CADE sensitivity values (*e.g.,* LOD and LOQ) for silver nanoparticles. Figure 3.21 shows calibrations curves of 20 nm Ag_{TW20} in 10 mM HEPES buffered media. Each experimental point represents the mean value from a set of a minimum of 3 experiments with error bars that represent 95% confidence intervals. LOD and LOQ values are mathematically defined in Equations 3.5 and 3.6. For the case of Ag_{TW20}, the LOD is 2.8 ppm and LOQ is 6.9 ppm with a 95% confidence level.

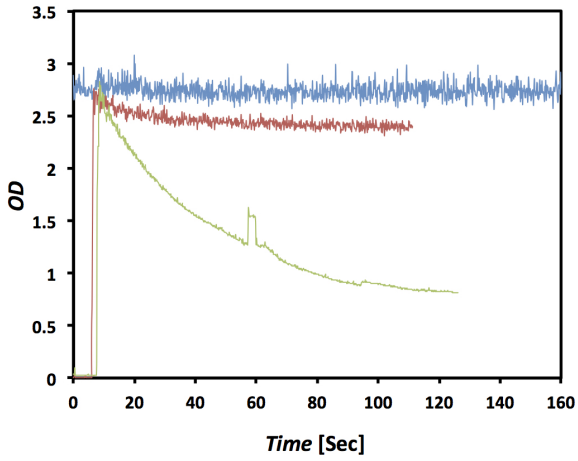

Figure 3.20: Optical density of CADE assay at pH 7.0 (10 mM NaBH4 and 10 mM HEPES) in the absence (blue) and presence of Ag_{TW20} (red) and Ag_{TA} (green) at a fixed mass concentration of 500 ppb recorded at 665 nm. ENPs are added at t = 15 s causing MB-BH_4 optical density to decrease due to reduction of MB.

Geranio *et al.* reported that silver textiles released a portion of the incorporated Ag after washing in conventional laundry processes.[185] In this study, we used a laboratory washing

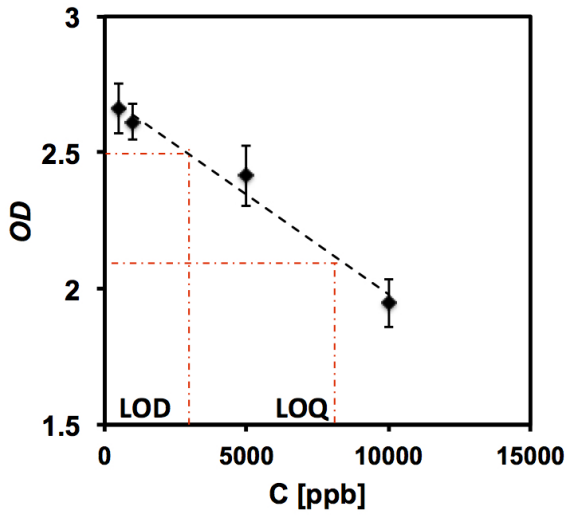

Figure 3.21: Calibration curves showing optical density as a function of silver nanoparticles coated with tween-20 in HEPES buffered media (10 mM). Each experimental point represents the mean value from a set of a minimum of 3 experiments with error barsthat represent 95% confidence intervals. Assay sensitivity values are shown by red dotted lines as limitof detection (LOD) and limit of quantification (LOQ).

machine to simulate the household laundering of a number of commercially available fabrics containing both Ag ENPs and silver salts. The washing procedure was carried out as described in previous literature with some slight modifications.[185, 186] Representative of textile samples, chest area, (0.8 g) were washed in 14 mL of ultra pure water (pH ∼5.7, conductivity 18.2 mΩ) or in a detergent solution of 2003 AATCC Standard Reference Liquid Detergent without brightener (11.2 μL detergent in 15 mL DI water, gives equivalent concentration to 0.5 cups detergent in 40 gallons water) in a 25 mL pre-cleaned polyethylene bottles (CAS:73212, U.S.Plastic Copr) with 6 polyethylene beads (CAS:91545, U.S.Plastic Copr) and mixed in a rotatory shaker at 40 rpm for 168 h at room temperature and in absence of light. Each washing experiments, including controls, were carried out in triplicate. Control samples represent a polyester shirt (Asics Men's Core Short Sleeve Top, 100% polyester mesh) without silver treatment for antibacterial purposes. After the washing procedure, the fabrics were removed and the excess liquid was gently pressed from the fabric

and collected for analysis. We introduced these solutions to CADE assay to determine the surface catalytic activity of Ag extracted from textiles.

Due to the current need for sensitive and simple methodologies to assess for the presence of ENPs, we evaluate the capabilities of CADE to detect nanoparticles extracted from commercially available textiles. Figure 3.22A shows β values for control, Xstatic, Polygeine, LinkedON and UnlinkedON washing solutions. β values were extracted using Equation 3.2 and they represent the mean value from a set of three experiments with error bars that correspond to 95% confidence intervals. An analysis of variance (ANOVA) and subsequent comparison of means test showed that Xstatic and Polygiene samples do not differ from the control. However, LinkedOn and UnlinkedOn samples differed significantly from each other and from the control samples at an $\alpha = 0.05$ level (p-value < 0.0005 for all comparisons). This test shows that the difference in the β values are likely due to the presence of silver suspended in the solution and not due to random error. Control sample has a β value of $\sim$2.85, representing the highest absorbance of dye solution. The β values range from 2.82 for Polygene to 2.59 for LinkedON sample. Lower β values correspond to higher Ag catalytic activity. In addition, we measured the total silver metal concentration of the washing solutions via ICPMS. The Ag concentration of the samples was 345 $\pm$ 59.7, 226.6 $\pm$ 30.4, 0.067 $\pm$ 0.006, 0.055 $\pm$ 0.03, and 0.006 $\pm$ 0.005 ppm for Xstatic, Polygeine, LinkedON, UnlinkedON, and control samples, respectively. Although, the concentration of silver on textiles that contained Ag_{ENP} (*e.g.,* LinkedON, UnlinkedON) was three orders of magnitude lower than silver salts, the catalytic activity recorded was higher. We can concluded that the higher catalytic activity observed in this analysis could be potentially due to the presence of ENPs extracted from fabrics since ENPs have lager surface area (where the electrons can relay between MB and BH_4) than do metal ions extracted from Xstatic and Polygiene fabrics.

In order to confirmed the potential applicability of CADE assay to detect ENPs used in industrial processes such as CMP polishing methods, we assessed the catalytic reactivity of colloidal silicon dioxide (c-SiO_2) and fumed silicon dioxide (f-SiO_2) suspensions used in

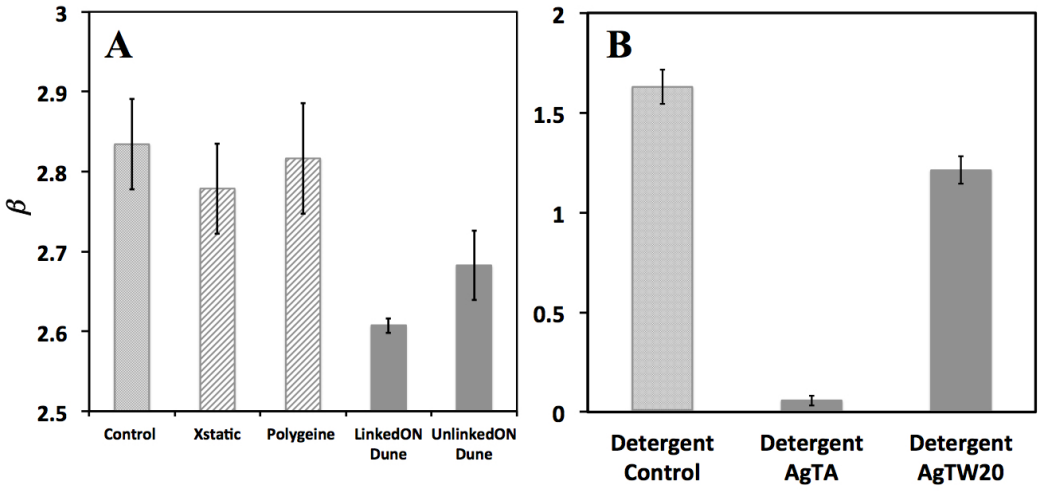

Figure 3.22: β values corresponding to the presence of silver extracted from textiles (A) and analysis on the effect of washing detergent in CADE assessment capabilities. Each experimental value represents the mean value from a set of 3 experiments with error bars that correspond to 95% confidence intervals. ANOVA test and subsequent comparison of means test showed that Dune samples, detergent with Ag_{TW20} and Ag_{TA} differed significantly from each of the control samples ($\alpha = 0.05$, p-value < 0.0005). This test shows that the difference in β value means are likely due to the presence of the different Ag and not due to random error.

semiconductor fabrication. c-SiO_2 and f-SiO_2 slurries were provided by Cabot Inc. through collaboration from the Semiconductor Research Corporation (SRC) and the SRC Engineering Research Center for Environmentally Benign Semiconductor Manufacturing. Since the slurries were custom synthesized, there were no intellectual property challenges to overcome nor any proprietary chemical additives. Table 3.6 summarizes the physiochemical properties of the two CMP slurries, including information provided by the manufacturer as well as DLS and TEM characterization data.

The reduction of MB by BH_4 depends directly on the catalytic activity of nanoparticles in CMPs. Figure 3.23 shows β values as a function of CMPs composition (c-SiO_2 and f-SiO_2) at a constant concentration of 100 ppm. All β values are reported as the mean of at least five experimental measurements with error bars that denote the 95% confident intervals ($\alpha = 0.05$). An analysis of variance (ANOVA) and subsequent comparison of means test showed that all three samples differed significantly from each other at an $\alpha = 0.05$ level

(p-value < 0.0005 for all comparisons). This test shows that the difference in the β value means are likely due to the presence of the different nanoparticles and not due to random error. In the absence of CMPs in the CADE solution, the β values are $\sim$2.8, representing the highest absorbance of CADE solution. The β values range from 2.6 for c-SiO_2 to 2.4 for f-SiO_2. Lower β values correspond to higher CMP catalytic activity. At fixed CMP mass concentration, the surface charge of nanoparticles may have an influence on the catalytic reactivity of CMPs. We believe negatively charged particles, c-SiO_2 and f-SiO_2, with a surface charge of -21 and -50 mV, may electrostatically repel BH_4 molecules to the surface of the particle, which then inhibit the reduction of MB, resulting in high β values. According to Azad *et al.* when BH_4 absorbs to the surface of nanoparticles, it creates a negatively charged layer that attracts cationic organic dyes, such as methylene blue in CADE.[168] This electrostatic attraction or repulsion between particle surfaces and the reducing agents increase or decrease the reduction rate of MB similar to the one we observed for c-SiO_2 and f-SiO_2.

Table 3.6: Summary of key characteristics and characterization analysis for model CMP slurry composition

	c-SiO_2	f-SiO_2
Material	Colloidal SiO_2	Fumed SiO_2
pH	2.5 - 4.5	10
Particle size [nm]	50 - 60	120 - 140
Diameter by TEM [nm]	36 $\pm$ 9	—
Diameter by DLS [nm]	46 $\pm$ 0.2	148 $\pm$ 5.1
Zeta potential [mV]	-21	-50

Taken together, we have developed a sensitive, simple and affordable methodology to screen for the presence or absence of ENPs extracted from commercial products (*e.g.,* textiles) and ENPs used in industrial applications (*e.g.,* microprocessor fabrication). In this section, we present a catalytic-colorimetric method for screening a range of metal (Ag) and oxide (SiO_2) ENPs that are commercially available in consumer goods. Our colorimetric

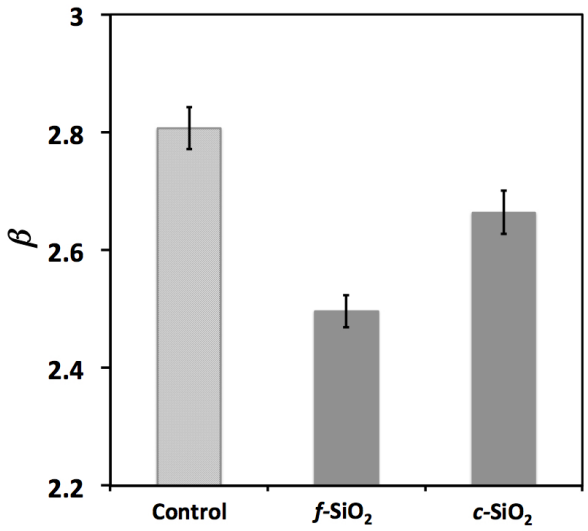

Figure 3.23: β values as a function of CMPs type at a fixed mass concentration of 100 ppm. Control experiments correlate to absence of CMPs in the assay. β value are an average over 5 experiments with error bars that denote 95% confidence intervals. ANOVA test and subsequent comparison of means test showed that all three samples differed significantly from each other ($\alpha = 0.05$, p-value < 0.0005). This test shows that the difference in the β value means are likely due to the presence of the different CMPs and not due to random error.

assay to detect engineered nanoparticles may aid in the assessment of ENPs for industrial applications as a quality control technique for the production of nano-enable products and for the detection of ENPs in accidental environmental spills by industries that used nanoparticles during the fabrication of products.

3.5 Correlation of ENP Catalytic Reactivity and Bacterial Cytotoxicity

During the past three decades, multiple studies has evolved to understand the biological and environmental impacts of ENPs, predict their potential toxicity, and the design of safe nanoproducts.[187, 188, 189, 190] Understanding the interaction mechanisms between biological systems and ENPs and their produced ions are a current interest among multiple research groups since it could provide insights to their potential applications as disinfectants or preser-

vatives as well as understanding possible human health implications.[36, 28] The ability to control some of the physicochemical properties of nanoparticles (*e.g.,* size, stability, morphology, structure, and shape) through manipulation of temperature, pH, metal concentrations, polymeric capping agents, *etc*, provides an opportunity to maximize the functional performance while minimizing the unintended adverse consequences of ENPs. A large number of studies have investigated oxide ENPs toxicity by comparing them to nanomaterials known to exhibit adverse environmental side effects (*e.g.,* ZnO and TiO_2).[191, 192, 193, 194, 195, 196] The properties that have been compared include length scales (micro vs. nano), suspension media, oxidative states, and other intrinsic material properties.

We selected copper oxide engineered nanoparticles (CuO_{ENP}), as a surrogate material, to investigate the effect of particle shape and surface catalytic reactivity in cytotoxicity responses on biological relevant systems (*e.g., Escherichia coli*). Multiple studies have shown that CuO_{ENP} shape influences material properties, such as the electronic band structure, redox potential, optical properties, electrical conductivity and antimicrobial activity.[197, 198, 199] However, the direct influence of shape on CuO_{ENP} has not been thoroughly investigated and remains an opportunity to understand how this property will affect the performance and/or adverse impacts when they are released into the environment.

There is interest in understanding the toxicity of CuO_{ENP}. Various research groups have emphasized their efforts on resolving the mechanistic pathways of ENPs toxicity on biological systems, specifically the contributions of the material itself versus the released ions.[191, 200, 201, 202, 203, 189, 204, 205, 206] When a nanoparticle approaches a cell membrane, several interactions are possible, as illustrated in Figure 3.24. ENPs could be repelled by the membrane, adsorb onto the membrane, become stable embedded within, pass through it, induce pore formation, activate membrane bound receptor proteins, and production of reactive oxygen species (ROS) from the ENP material itself and/or the released ions (*e.g.,* Cu^{+2}).[48, 207, 208, 187, 209, 210]

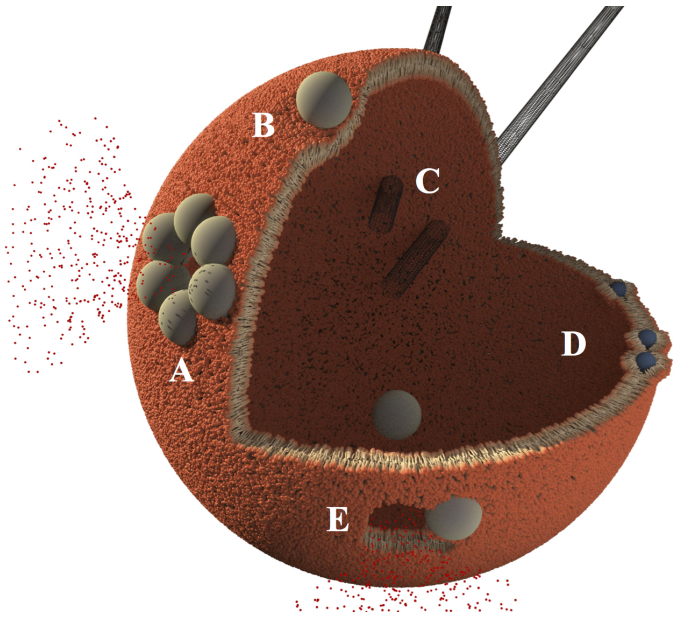

Figure 3.24: Schematic showing diverse ENP interactions with a cell membranes (in the form of lipid vesicle), including (A) aggregation in the membrane forming a disruptive nanopore, (B) adsorption to and potential deformation and modification of phase behavior of the membrane, (C) penetration and disruption of the cell membrane by high aspect ratio ENPs (*i.e.,* carbon nanotubes), (D) partitioning of ENPs into the hydrophobic core of the bilayer, and (E) disruption of the bilayer and formation of nanopores, potentially leading to increased permeability to molecules and ENPs. The small red dots emanating from the pores represent the leakage of molecules or organelles from the core of cells.

This study was performed in collaboration with Leanne Gilbertson from Yale University and investigates the influence of CuO_{ENP} shape and catalytic reactivity to gram negative *Escherichia Coli*-K12 cytotoxicity. We compared CuO nanosheets (CuO_{ST}), synthesis described below, to commercially available CuO_{ENP}. Data shows that CuO_{ST} have a different shape, approximately a magnitude greater in surface area than other studied ENPs, and display higher electrochemical and catalytic surface activity compared to the CuO_{ENP}. CuO_{ENP} (< 50 nm), were purchased from Sigma-Aldrich and used as received. CuO_{ST} were synthesized by dissolving 3.4 g of Copper (II) nitrate trihydrate (Sigma- Aldrich, 99%) in 100 mL of ultrapure water and mixed to a preheated (60 °C) in a solution (900 mL) containing 120 g of NaOH (Sigma-Aldrich, 98%) and 22 g of hexadecyltrimethylammonium bromide (CTAB, Sigma-Aldrich, 99%). The combined solution was mixed by a magnetic stirrer and

allowed to react for ∼1 hour at 60 °C. The black precipitate, which contains CuO_{ST}, was isolated by vacuum filtration. Then, the CuO_{ST} precipitate was washed with ultrapure water followed by rinsed of ethanol to remove residual reactants and dried in an oven for ∼1.5 hour at 250 °C. The reactivity of the CuO_{ENP} and CuO_{ST} was characterized using a biologically relevant oxidation of glutathione (GSH) assay and surface catalytic reactivity via the CADE assay. TEM and SEM analysis provide evidence on the interaction of CuO_{ENP} with *E. Coli*. Results presented in this section show that CuO nanosheets exhibit higher cytotoxicity than ENP. Data, also, provides insights into potential mechanism of bacterial internalization of CuO_{ENP}. This work contributes towards the understanding in the relationships between specific physical (*e.g.,* particle size, surface area) and chemical properties (*e.g.,* catalytic reactivity) of ENPs on their cytotoxicity effects in biological relevant systems.

3.5.1 Physicochemical Properties of CuO Nanopowder and Nanosheets

Examination of the impact of CuO shape on cytotoxicity is a current necessity. We characterized size, shape, surface area, surface charge, and reactivity of CuO. We summarized characterization data for CuO_{ENP} and CuO_{ST} on Table3.7.

Table 3.7: Physicochemical characterization of CuO nanopowder and nanosheets

ENPs	Size/Shape (dry)	Dispersed Aggregate Size [nm]	BET Surface Area [m^2/g]	Zeta Potential [mV]	β Value [1 ppm / 10 ppm]
CuO_{ENP}	< 50 nm (heterogeneous shape)	157	9.2 ± 0.5	-6.4 ± 23.7	2.67 ± 0.06 / 2.16 ± 0.07
CuO_{ST}	250 - 1000 nm^2 x 15 nm thick (sheets)	557	20.0 ± 0.1	-22.1 ± 20.9	2.57 ± 0.02 / 1.11 ± 0.07

We confirmed the crystalline structure of the three CuO materials by X-ray diffraction (XRD). Figure 3.25A shows XRD spectra of CuO_{ST} and CuO_{ENP}. We performed XRD measurements with a Rigaku SmartLab X-ray diffractometer using Cu Kα radiation (λ =1.5418 $\mathring{A}$) and a rotating anode source, operated at 45 kV and 200 mA. The characteristic diffraction peaks for cupric oxide (110), (111)/(002), (111)/(200), (202), (020), (202) can be observed across all of samples and correlates with previous work by Xu *et al.*[211] TEM, SEM

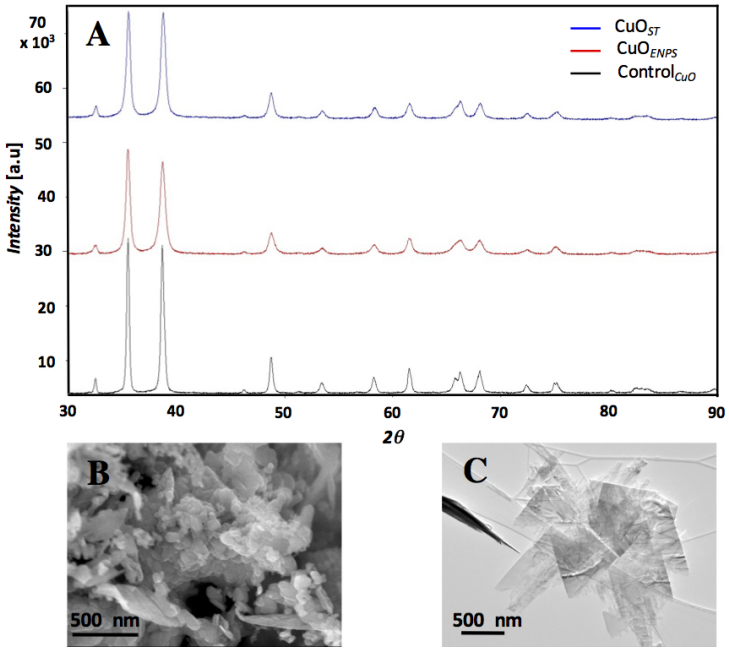

Figure 3.25: X-ray diffraction spectra of copper oxide nanosheets (CuO_{ST}), nanopowder (CuO_{ENP}), and CuO control material ($Control_{CuO}$) (A). Scanning electron micrographs of CuO_{ENPs} (B) and transmission electron micrograph of CuO_{ST} (C). Data collected by Leanne Gilbertson from Yale University and results were submitted to ACSnano.[212]

and atomic force microscopy (AFM) was used to determine the morphology, dimensions, and shape of all CuO samples. Figure 3.25 shows SEM and TEM micrographs for CuO_{ENP} and CuO_{ST}. Data indicates that CuO nanopowder have irregular sphere shaped particles (< 50 nm), and CuO nanosheets are sheet-like particles of heterogenous lengths and widths (250 nm - 1 μm). We observe aggregates on CuO materials, as shown in micrographs, which might be attributed to the intermolecular forces (*e.g.,* van der Waals, electrostatic) of ENPs in the suspension media that is confirmed by low particle surface charge. To resolve the instability of particles, we employed sonication to agitate and disperse CuO particles. However, it is difficult to stabilized CuO particles for long periods of time without the use of surfactants or polymers particularly in biological or environmental media.[213] We did not use any surfactants or dispersion stabilizing chemicals in our analysis to avoid the perturbation of the CuO or cytotoxicity experiments.

We determined size and size distribution for CuO_{ENP} and CuO_{ST} in a biological medium (0.9% NaCl) via DLS. Data shows CuO nanopowder is smaller in size and the sample is more monodispersed than nanosheets sample. We used Brunaur-Emmett-Teller (BET) method to analyze the surface area of CuO material with methodology described previously.[214] All BET measurements were carried out in a Quanta Chrome Autosorb-1C static volumetric instrument. We degassed CuO samples at 200 °C for at least 4 hours and measured using an eleven point BET protocol. The linear region of the BET plot of the N_2 adsorption/desorption isotherm were used to calculate specific surface area. The surface area per gram of nanopowder and nanosheets is 9.20 ± 0.45 and 20.01 ± 0.12 m^2/g, respectively.

We also characterized CuO surface charge in biological media, the same as used for cellular analysis, and over a wide rage of pH values. Electrophoretic mobility measurements were collected to determine the dependence of material stability as a function of complexity (*e.g.,* proteins, lipids, amino acids, *etc*) and proton concentration on suspension media. Zeta potential of CuO nanosheets was determined at a fixed concentration, 20 ppm, using dynamic light scattering (DLS) (NICOMP 380 ZLS, Particle Sizing Systems, Santa Barbara, CA) over a 15 min time period. The zeta potentials of particles influence their electrophoretic mobility, as describe by the Henry equation and the Smoluchowski approximation.[120] All working solutions were prepared in ultrapure water (18.3 MΩ-cm, Milli-Q Advantage A10 system, Millipore Corp., Billerica, MA) by first placing the experimental vial on a rotary shaker (50 rpm) for 20 min at room temperature (23 °C), followed by mild sonication for 1 h (40 kHz, 2510DTH Branson, Ultrasonic Corp., Danbury, CT) prior to each experiment. We prepared a stock 500 mM for each buffer (*e.g.,* HEPES, citric acid, tris, bis-tris) at 22±2 °C. All reagents were purchased from Sigma Aldrich. Each stock buffer solution had a pH near the pKa of the respective buffer for maximum buffering capacity.[215] Stock 500 mM buffer solutions were diluted to 20 mM with DI water prior to measuring pH of the solutions using a dual conductivity and pH meter. Data collected on biological media shows that CuO materials used in this study has zeta potential values ranging from 0.05 to -22.10 mV

indicating that CuO_{ENP} and CuO_{ST} samples are unstable in the working suspension (Table 3.7). Further, when CuO_{ST} was investigated in different pH solutions, the magnitude of particle surface charge (zeta potential) increased with increasing pH indicating that CuO nanosheets are more stable at higher pH (Figure 3.26).

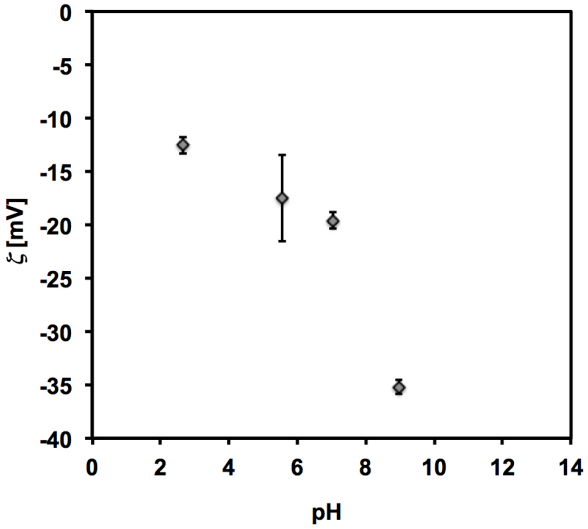

Figure 3.26: Surface charge of CuO nanosheets (reported as zeta potential) as a function of pH at a fixed concentration (20 ppm) and ionic strength (20 mM). The data represents the mean value from a set of six experiments with error bars that correspond to 95% confidence intervals.

We determined the surface reactivity of CuO nanopowder and nanosheets using the colorimetric assay to detect engineered nanoparticles (CADE). The surface catalytic reactivity of nanomaterials in aqueous media is assessed colorimetrically using a combined dye (methylene blue, MB) and a reducing agent (sodium borohydride, BH_4) system as described in previous sections of this dissertation. The reduction of MB by borohydride depends directly on the catalytic activity of CuO particles. Figure 3.27 shows β values as a function of CuO shape (nanopowder and nanosheets) at a constant mass concentration of 1 and 10 ppm. In the absence of CuO the β value is approximately 2.8, representing the maximum dye absorbance. The β values of the CuO samples range from 2.6 for nanosheets in the case of 1 ppm to 1.1 for 10 ppm. Lower β values corresponding with higher material catalytic activity. The nanosheets present the lowest β value and the greatest catalytic surface activity of the CuO

materials studied here. An analysis of variance (ANOVA) was carried out and confirms that the catalytic surface activity of CuO nanopowder and nanosheets are significantly different from control ($\alpha = 0.05$).

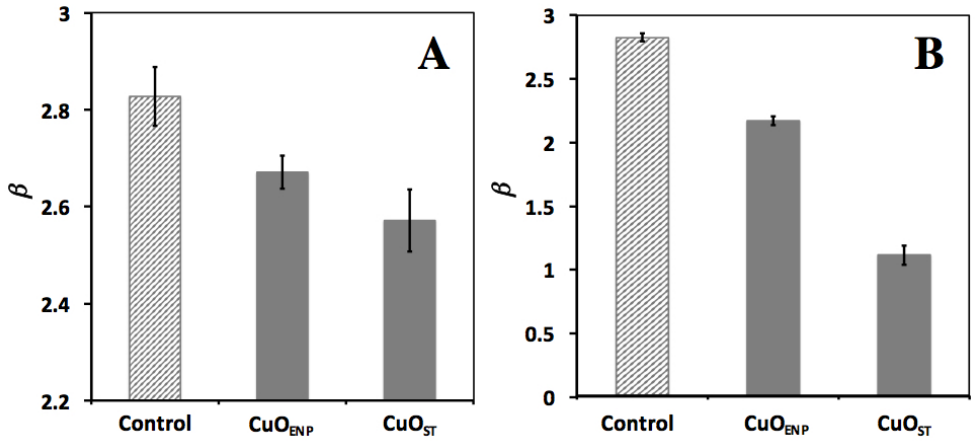

Figure 3.27: β-values for nanopowder (CuO_{ENP}) and nanosheets (CuO_{ST}) at a fixed mass concentration of 1 (A) and 10 ppm (B). Control experiments correspond to the absence of CuO material. The lower the β-values, the higher the material catalytic activity. Each experimental value represents the mean from a set of five experiments with error bars that correspond to 95% confidence intervals. ANOVA and subsequent comparison of means test showed that the difference in the values of CuO_{ENP} and CuO_{ST} are statistically significant ($\alpha = 0.05$, p-value < 0.0005).

Taken together, these characterization results indicate that CuO nanopowder and nanosheets differ in size, shape, dispersed aggregate size, morphology, surface area, and surface reactivity (control $<$ CuO_{ENP} $<$ CuO_{ST}). These properties influence the biological impacts (*e.g.,* cytotoxicity) and can be potentially modified for future ENP applications such as disinfectants or antibacterial coatings.

The bacterial responses of CuO_{ENP} and CuO_{ST} were examined by using *E.coli* K12 (MG1655) as a biological model organism. Bacteria are a preferred model organism for assessing environmental hazards and fates of chemicals as well as materials.[216] *E.coli* has gained momentum across multiple fields to be used as a representative platform to evaluate cytotoxicity and antibacterial performances of ENPs, specially for CuO nanomaterials.[217, 203, 199] Here we used both acellular and cellular assays to corroborate observed trends in

bacterial impact of CuO ENPs. The acellular glutathione assay serves as an indicator of cytotoxicity as well as a measurement for chemical reactivity of the CuO materials and the cellular assay evaluates the adverse impact of CuO when they get into contact with *E.coli* cells.

Glutathione (GSH) is a biomolecule that serves an important role in maintaining a healthy cellular redox environment and can be used a surrogate molecule for acellular assays.[218] The oxidation of GSH to oxidized glutathione (GSSG) serves as an indicator of a material's ability induce oxidative stress and potential mortality at the cellular level. GSSG was used as a measurement of relative oxidation potential for these CuO materials. Details for GSH assays are described elsewhere.[219, 220] GSH concentration quantification was done by measuring the optical density of reagents at $\lambda_{max} = 412$ nm. Each CuO sample was compared to the control (no CuO) at each time point to obtain a percent oxidation of GSH according to the Beer-Lambert Law, as presented in Equation 3.1. Results are shown as the percent of GSH that is oxidized over time compared to the initial GSH concentration. Figure 3.28A and B shows the oxidation percentage of GSH as a function of experimental time for CuO_{ENP} and CuO_{ST}, respectively. Among CuO materials, nanosheets has the highest rate of GSH oxidization $> 60\%$ within 15 minutes follow by CuO_{ENP} with $\sim$50% in 1 h. Findings correlated with previous work that showed that ENPs possess higher propensity to oxidize GSH and create elevate cellular stress compared to bulk material.[221, 222, 192, 195, 196, 223] Suggesting that the manipulation of CuO shape at the nanoscale level has a significant influence on bacterial cytotoxicity.

In-vitro cellular assays were used to investigate *E.coli* response to CuO_{ENP} or CuO_{ST} exposure. Details of cellular assay is described by Pasquini *et al.*[220] We plate solutions and quantify the colonies of *E.coli* to determine the percent reduction in CFUs/mL by comparing them to the control samples, no CuO. Figure 3.28D shows the percent reduction of *E.coli* [CFUs] as a function of CuO concentration for nanopowder and nanosheets. CuO_{ST} reduced 100% of bacteria colonies at a mass concentration of 40 ppm, implying that nanosheets

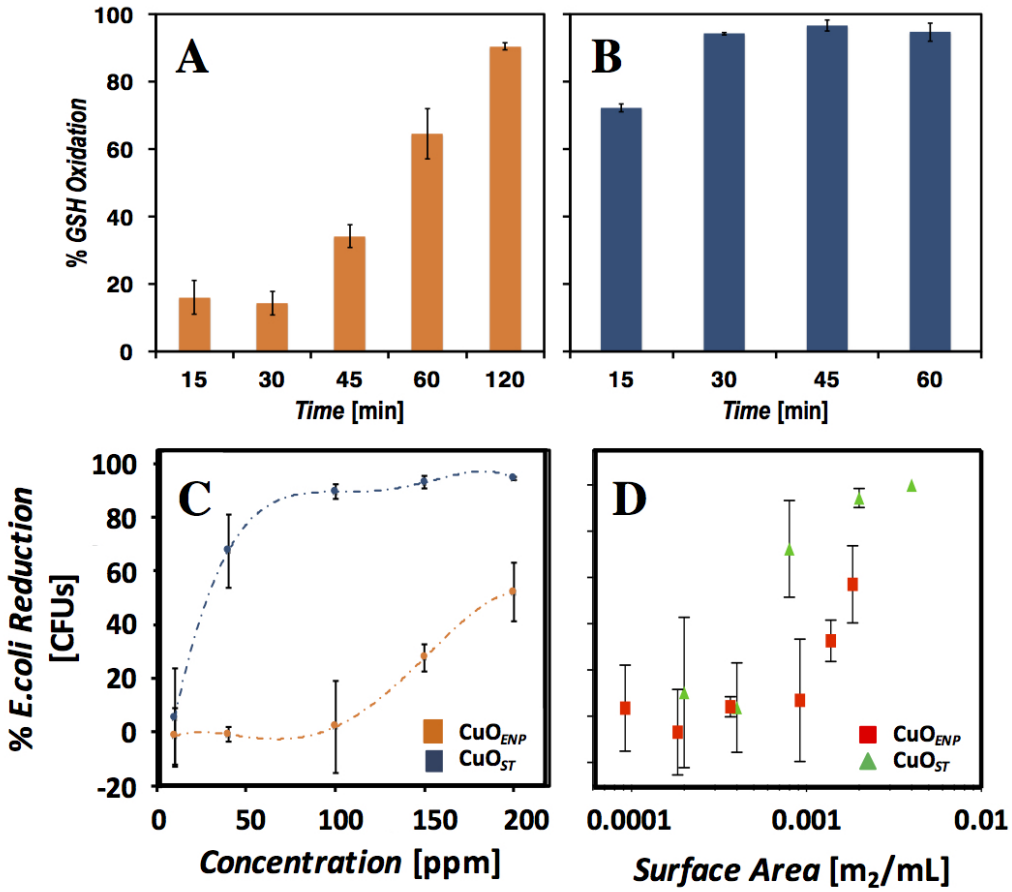

Figure 3.28: Percentage of oxidize glutathione (GSH) as a function of time for CuO_{ENP} (A) and CuO_{ST} (B). CuO nanosheets have the highest oxidation potential (∼100% oxidation within 30 minutes). Each experimental value represents the mean value from a set of six experiments. Percent reduction *E.coli* colonies as a function of CuO_{ENP} (orange) and CuO_{ST} (blue) mass concentration exposure (C) and surface are response for CuO_{ENP}, and CuO_{ST} (D). Data shows consistency under both analysis and nanosheets exhibit higher cytotoxicity than nanopowder material. Samples were run in triplicates. Data collected by Leanne Gilbertson from Yale University and results were submitted to ACSnano.[212]

possess the highest cytotoxicity among the other CuO materials. In contrast, CuO_{ENP} did not attain 100% *E.coli* colony reduction even at the higher concentrations ∼200 ppm. Results are consistence with our acellular analysis that shows that CuO nanosheets exhibit higher cytotoxicity compared to different shaped ENPs (*i.e.,* nanopowder). Results from both acellular and cellular assay indicate that shape and size on ENPs play an essential role in the cytotoxicity and biological impact of CuO materials.

Table 3.7 provides evidence on the distinctive variation of surface area for CuO samples. It is essential to understand whether the cytotoxicity observed for the CuO materials hold when it is normalized to their respective surface areas. Mass concentrations (mg/mL) of the CuO nanomaterials were converted to surface area concentrations (m^2/mL) using the surface areas (m^2/g) determined by BET analysis. Figure 3.28E shows percent reduction *E.coli* colonies as a function of particle surface area for CuO_{ENP}, and CuO_{ST}. The relative cytotoxicity trends for nanosheets remains present when they are considered on surface area basis compared to nanopowder; reaffirming that ENP shape and size influence the biological impacts of nanomaterials. This work represents a step toward the understanding of nanomaterials' dose standardization (*e.g.,* mass, particle, or surface area basis) for environmental toxicological analysis, which is a current topic of discussion among the scientific community.[224, 225, 226]

Results suggest that particles with higher surface catalytic activity and surface area can induce higher biological responses, such as oxidation of biomolecules or bacterial mortality. This provides an opportunity to compare and correlate how ENPs surface properties affect the potential toxicological outcomes. Figure 3.29 show a comparison analysis of CADE and bacterial responses for CuO_{ENP} and CuO_{ST}. In order to compared all assays, we report activity responses as the normalized the experimental outcomes from the catalytic at 10 ppm, acellular at 30 min, and bacterial assays at 40 ppm. The normalized response is given by

$$\frac{(R - R_{min})}{(R_{max} - R_{min})} \tag{3.8}$$

Where R is the experimental response-dependent, R_{min} is the initial experimental response, and R_{max} is the maximum experimental response for a given assay. Data shows a potential correlation between ENPs catalytic activity measured using CADE with the biological responses of nanomaterials at certain experimental conditions. However, more investigations need to be performed in order to firmly determine the direct correlation between surface catalytic activity and potential toxicity of ENPs.

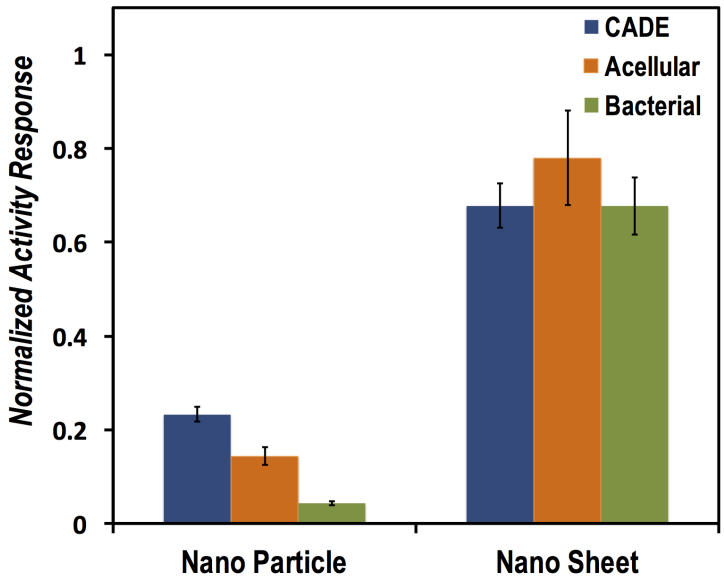

Figure 3.29: Surface catalytic activity and bacterial responses correlation analysis for CuO materials as normalized activity responses obtained by CADE, GHS, and bacterial assays for CuO_{ENP} and CuO_{ST}. Each value represents the mean from a set of three experiments with error bars that correspond to 95% confidence intervals.

While the mechanisms for cellular uptake of ENPs via endocytosis has been demonstrated for eukaryotic cells (*e.g.,* mammalian and plant cell lines)[227, 202], the pathways by which nanoparticles interact with *E.coli* is still unknown. There is evidence for uptake of nanomaterials by bacterial cells.[217, 228, 229] One of the proposed mechanism involves internalization of ENPs after chemical or physical perturbation to the cell membrane .[49, 88, 230, 101] Once this protective barrier is breeched, the nanomaterial is able to move freely into the bacterial cell. Kaweeteerawat, *et al.* recently showed that both Cu and CuO ENPs can be internalized by bacteria without disruption of their cell walls and this that ultimately creates irreparable

damage to the integrity of prokaryote cells.[217] Results presented herein provide additional evidence of the interaction of CuO with *E.coli* and deepen the understanding of bacterial - ENPs uptake mechanism.

To evaluate the interaction of CuO_{ENP} and CuO_{ST} with *E.coli*, the usage of transmission electron microscopy (TEM), scanning TEM (STEM), and elemental mapping via electron energy-loss spectrometer was employed. Samples were prepared for electron microscopy by following the method described by Perreault, *et al.*[202] Figure 3.30 shows TEM, STEM

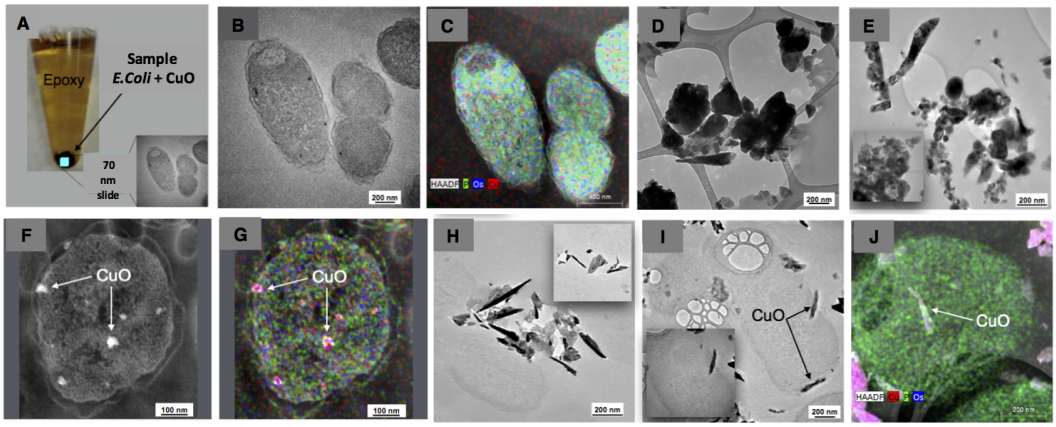

Figure 3.30: Photograph of CuO and *E.coli* sample fixed in resin prior to be sliced into 70 nm specimens (A), TEM and STEM-EDX micrographs control samples (B-C), CuO_{ENP} (D-G), and CuO_{ST} (H-J). Control samples correlates to *E.coli* in absence of CuO material. Data collected by Leanne Gilbertson from Yale University and results were submitted to ACSnano.[212]

and X-ray elemental mapping of CuO_{ENP} and CuO_{ST} in the presence of bacterial samples. Overall, results reveal the interactions of CuO with *E.coli* cells (*e.g.,* inside the cell, at the cell surface, and/or penetrating the cell wall). In the case of control experiments, no copper exposure to cells, phosphorous and osmium were identified that can be attributed to the intrinsic cell composition and to the staining solutions used for these experiments, respectively. Also, we observed a small copper readings in the control samples (shown as red), which can be due to the residual Cu in NaCl salt used to prepare the biological media. For the case of CuO materials, micrographs show evidence of copper interacting with *E.coli* cells, which are presented with arrows. While the micrographs provide evidence

that all CuO materials do interact with bacterial cells (*i.e.,* inside or embedded in the cell membrane), it is important to note that the internalized material is either as single particles, for the case of CuO_{ST}, or as aggregates. There has been significant evidence that ENPs do interact and accumulate at the surface of cell membranes, which are potential mechanisms for CuO materials.[50, 51, 48] Confirmation of some of the potential mechanisms are illustrated in Figure 3.30K, where CuO_{ST} are penetrating as well as at the accumulating in the cell membrane surface. Indicating that the material-cell mechanism of internalization is important aspect that require further examination.

We showed that shape, surface area, and reactivity of CuO material, specially nanosheets, increase the bacterial cytotoxicity for *E.coli* cells and provided information on how to manipulate some of physicochemical properties to enhance the antibacterial efficacy of CuO nanopowder and nanosheets. In some applications where the desired function is bacterial cytotoxicity, shape can be manipulated to improve functional performance efficiency and potentially decrease the total amount of CuO required to achieve final goals and for cases where antimicrobial activity is not desired, CuO shape can be manipulated to optimize the desired function while minimizing the potential for adverse environmental and human health impacts.

3.6 Summary

We have developed a sensitive and simple methodology to screen for the presence of ENPs in complex samples (environmental waters and biological fluids). In this chapter, we present a catalytic-colorimetric assay to detect engineered nanoparticles (CADE) method that is used to screen for a wide range of ENPs in complex matrices. This method is sufficiently sensitive to surface reactivity, which is a unique nano-scale property of environmental relevance in ENP toxicity, and uses inexpensive, commercially available reagents. CADE assay has detection limits below the typical concentrations commonly used in toxicological

studies[41, 231] with an analytical sensitivity in the range reported for LC_{50} concentration values.[232, 233] Our results demonstrate that this assay can detect the presence of ENPs at ppb concentration levels. We have detected a wide range of metal (*e.g.,* Ag and Au) and metal oxide (*e.g.,* CeO_2, SiO_2, VO_2, CuO) nanoparticles with a diameter range of 5 to 400 nm and multiple capping agents. The detection capabilities of this assay enable the assessment of ENPs in serum, urine, environmental waters, and natural organic matter as well as nanomaterials extracted from commercial products without any sample preparation or complex instrumentation. Incidental or endogenous nanoparticles may pose a challenge for the colorimetric assay. As a first step, we showed that this assay is not susceptible to false positive readings in lake water, which most likely contains endogenous nanoparticles, however we can not draw general conclusions about the assay's efficacy in the presence of all incidental and natural nanoparticles. The development of CADE may aid in the assessment of nanoparticles for environmental, industrial, and medical applications.

We are also interested in correlating ENPs catalytic activity measured using CADE with the formation of reactive oxygen species, cellular toxicity, and biological responses of nanomaterials. We used CuO, as a surrogate material, to study the effect of shape, size (micro versus nano), surface area, and material reactivity to cytotoxicity of *E.coli* cells. We employed electron microscopy to support the existence of bacterial internalization of copper nanomaterials. Our results will build upon the foundation and refinement of information and resolve the mechanistic pathways through which ENPs' internalization occurs. Data shows that ENPs with higher catalytic activity reduce vitality of bacterial colonies and produce higher cytotoxicity to *E.coli* cells. Our work represents a step towards reliable, sensitive, and accurate methodologies for the detection of ENPs in complex matrices, using low-cost and portable instrumentation. This work will ultimately assist in the design criteria to enable development of nanomaterials for enhanced functional performance while minimizing potential adverse and unintended consequences.

Chapter 4

Summary, Recommendations, and Closing Remarks

4.1 Results Summary

Nanotechnology has a large potential for improving multiple aspects in human welfare, such as medicine, energy efficiency, manufacturing, catalysis, and food preservation, among others.[234, 235] However, both scientists and the public are concerned about the risk and the potential adverse health impacts of engineered nanoparticle exposure in manufacturing facilities (*i.e.,* the workplace), from commercial products, or environmental impacts when ENPs are released.[42, 236] Nanotechnology introduces a new field that requires novel approaches and methodologies for hazard and risk assessment. The appropriate platform for safety assessment and detection of nanoparticles must consider unique properties and functions of ENPs , including how the physicochemical properties relate to mechanisms of injury at the nano - bio interface as well as how to employ their individual properties for detection. This rapidly advancing field requires novel test strategies since the current techniques are expensive, do not work well in biological and environmental relevant samples, and require highly trained personnel to operate.[237] This dissertation includes a detailed development of

methodologies to assess for the presence and biological impacts of engineered nanoparticles, which represents a step toward the understanding of potential toxicity of these materials, design of safe nanoproducts, and advancement of nanomedicine.

In this dissertation, we employed an electrophysiological methodology to assess for the biological impact of ENPs to cellular membranes. We report direct measurements of ion migration across lipid bilayers induced by ENPs. Our results suggest that the distinctive current flux behavior for carbon nanotubes may be attributed to ions electromigrating through the core of CNTs that are inserted and span into the suspended lipid bilayer. Electrophysiological measurements enabled monitoring of ENP and cell membranes (lipid bilayer) interaction dynamics in real time. The diverse set of current traces suggests that the mode of bilayer disruption is dependent on the shape and concentration of particles. Furthermore, we presented a quantitative analysis (*e.g.,* FEI and average conductance) of the interaction of ENPs - lipid membranes that captures the ion migration effect induced by particle shape, size and concentration. Given that the disruption of cellular membrane disruption is one of the potential mechanisms leading to nanotoxicity, our electrophysiological platform provides insights on the biological impacts of nanoparticles that can, ultimately, serve as a potential predictor of cytotoxicity for ENPs.

This dissertation also covered a description on the development of a simple and affordable methodology to screen for the presence of ENPs in environmental waters and biological fluids as well as the detection of nanoparticles extracted from commercially available products. This work present a catalytic-colorimetric method for screening a wide range of ENPs in complex matrices which may aid in the detection of nanoparticles for environmental, industrial, and medical applications. The method is sufficiently sensitive to surface reactivity which is a unique nanoscale property of environmental relevance in ENP toxicity, and uses inexpensive, commercially available reagents. This assay has detection limits below the typical concentrations commonly used in toxicological studies with an analytical sensitivity in the range reported for LC_{50} concentration values. Our results demonstrate that this as-

say can detect the presence of metal and metal oxide ENPs at ppb concentration levels as well as assessing for ENPs extracted from nano-enable products. We also correlated ENP's catalytic reactivity measured using this assay with bacterial cytotoxicity. Proving that our colorimetric assay can serve as a potential screening for toxicity of nanoparticles. Our work represents a step toward reliable, sensitive, and accurate methodologies for the detection of ENPs in complex matrices as well as extracted ENPs from consumer goods, using low-cost and portable instrumentation.

4.2 Future Recommendations

In the second chapter of this dissertation, we showed the electron migration across cell membranes due to the interaction with ENPs (*i.e.,* carbon nanotubes, quantum dots) and how concentration as well as particles aspect ratios influenced the ion flow across lipid bilayers. There are some interesting directions that this study can take: determine mechanism of interaction between CNTs and cell membranes (*e.g.,* contributions of ion flowing through the core of CNTs or creation of nanopores around the ENP) by investigating the effect that capped carbon nanotubes [101] on the electron flux across lipid bilayers. Examine CNT ion conductive properties through membranes by chemically functionalized the tip of MWCNT that will modified their ion selectivity.[238, 239] This approach should provide further evidence that current fluxes are not induced by transmembrane gaps while elucidating the mechanism of step increase in ion flow. It should also allow us to determine how specific physicochemical properties (*e.g.,* size, core composition, surface functionality) of a single set of ENPs will directly influence the interaction with cell membranes, and to specify whether CNTs are permanently embedded within cell membranes or act as ion channels while temporarily interacting with the lipid membrane. We can also investigate nanoparticle transport through cell membranes by correlating ENP mass spectroscopy measurements in both sides of the suspended lipid bilayer. Given that cellular membrane disruption is one of the potential

mechanisms leading to cytotoxicity, by addressing these mentioned concerns, the scientific community will gain some mechanistic understanding by which ENPs induce cell membrane disruption and how ENPs and lipid membranes properties govern the interactions.

With respect to the developed assay to detect engineered nanoparticles (CADE), there are some pathways that need to be considered in order to improve the assessment of ENPs for environmental, medical, or commercial applications. These include examining the effect of incidental or endogenous nanoparticles and how to differentiate them from ENPs. As a first step, we showed in this dissertation that our assay is not susceptible to false positive readings in lake water, which most likely contains endogenous nanoparticles, however we can not draw general conclusions about CADE's efficacy in the presence of all incidental and natural nanoparticles. It would also be important to determine the correlation of nanoparticles catalytic reactivity measured using CADE with the formation of reactive oxygen species in cellular toxicity assays, as well as the development of dye-reducing agent pairs that will be specific to a single ENPs' physicochemical characteristic (*e.g.,* composition, size, concentration, redox potential, reactivity). In addition, testing other commercial nano-enabled products (*e.g.,* food products, cosmetics, *etc*) and determine the assessment capabilities during their life cycle would be desirable. Examing the development of a single ENPs' catalytic descriptor value could be used to compared and measure catalytic reactivity of nanomaterials. A potential approach will be by measuring the catalytic activity via CADE of a reference material (*i.e.,* RM 8011-Gold Nanoparticles, Nominal 10 nm Diameter, National Institute of Standards and Technology, MD) and compare its value to unknown ENPs. We also would like to investigate the effect of hydrophobicity of the dye, complex formation of the dye with anionic surfactants, repulsion between the dye and charged surfactants, since we believe they may also impact the catalytic reactivity of the ENPs. Finally, in a step toward integration of CADE into portable devices for field analysis, we suspect that the potential usage of smartphone based optical detection technology, as portable spectrometer can be achieved in the years ahead[240, 241], as well as the creating a disposable, one time

use, CADE microfluidic cartridges for multiplex and portable detection of nanomaterials for occupational safety and study of environmental exposure to particles .

4.3 Closing Remarks

One of the topics that I have not covered in this dissertation is the experience of assisting Professor Jonathan D. Posner to setup his research lab. As Prof. Posner moved from Arizona State University to the University of Washington, I had the privilege of helping him to rebuild the lab from bare rooms and footprints to the functioning and efficient machine that it is today. I could write at length of all of the essential components (*e.g.,* microscopes, optical tables, ultra-pure water systems, dynamic light scattering instrumentation, pH meters, computers, softwares, laser cutter, fridges, chemicals, glassware, *etc*) and not-so-important components (*e.g.,* printers, label makers, markers, storage cabinets, gloves, *etc*) that I helped to set up and/or advised to purchase at the lab's initial stages after our transition to UW. However, there would not be much to learn from the discussion other than one simple fact that: *"it is simpler to truly understand and appreciate any complex system when you know all of parts and how they work together"*. I took great pride and thoroughly enjoyed rebuilding Posner's Research Lab. Having a keen understanding of the instrumentation that I used for the experiments presented in this dissertation provided me with a much greater insight into the data analysis and results than I would have had without having this experience. Even though, these efforts often go unnoticed and do not generally result in journal publications, the working knowledge gained often does come across in the quality of research presented.

The results of the developed methods to assess for the presence and biological impacts of engineered nanoparticles presented in this dissertation have proven to be of great utility for numerous potential applications including nano-toxicology, nano-medicine, industrial quality control, and basic understating of biophysics at the nano-level. However, like all good research, our results have lead to other interesting questions and directions that this

work might take. Many of these questions are currently being investigated here at Posner Research Lab and are sure to spring multiple interesting science and future applications. I am confident that Posner's research group will continue to make progress in these fields and discover many new breakthroughs along the way.

List of Publications Covered in this Work

1. **Corredor. C**, Reed. R, Westerhoff. P, Posner. J D, Colorimetric Detection of Silver Nanoparticles from Commercial Textiles *Environ. Sci. and Tech.*, In Preparation, 2015

2. Gilbertson. L, Albalghiti. E, **Corredor. C**, Fishman. Z, *et al.* Shape - Dependent Antimicrobial Activity of Nano-Cupric Oxide *ACS nano*, Submitted, 2015

3. Speed. D, Westerhoff. P , Sierra-Alvarez. R, Draper R, **Corredor. C**, Posner. J D,*et al.* Physical and Chemical Characterization of Nanoparticles in Chemical Mechanical Planarization Suspensions Used in the Semiconductor Industry: Towards Environmental Health and Safety Assessments *Environ. Science: Nano*, 2 (3): 227–244, 2015.

4. **Corredor. C**, Borysiak. M, Wolfer. J, Westerhoff. P, Posner. J D. Colorimetric Detection of Catalytic Reactivity of Nanoparticles in Complex Matrices *Environ. Sci. and Tech.*, 49 (6): 3611–3618, 2015.

5. **Corredor. C**, Hou. W, Klien. S A, Moghadam. B., Goryll. M, Westerhoff. P, Posner. J D. Disruption of Model Cell Membranes by Carbon Nanotubes *Carbon*, 60: 67–75, 2013.

6. Negoda. A. Liu. Y, Hou. W, **Corredor. C**, Moghadam. B,*et al.* Engineered Nanomaterial Interactions with Bilayer Lipid Membranes: Screening Platforms to Assess Nanoparticle Toxicity, *International Journal of Biomedical Nanoscience and Nanotechnology*, 3 (1-2): 52–83, 2013.

7. Moghadam. B, Hou. W, **Corredor. C**, Westerhoff. P, Posner. J D. Role of Nanoparticle Surface Functionality in the Disruption of Model Cell Membranes *Langmuir*, 28 (47): 16318–16326, 2012.

8. Hou, W., Moghadam, B, **Corredor. C**, Westerhoff, P., Posner, J D. Distribution of Functionalized Gold Nanoparticles between Water and Lipid Bilayers as Model Cell Membranes *Environ. Sci. and Tech.*, 46 (3): 1869–1876, 2012.

Scientific Covers Issues Presented in this Work

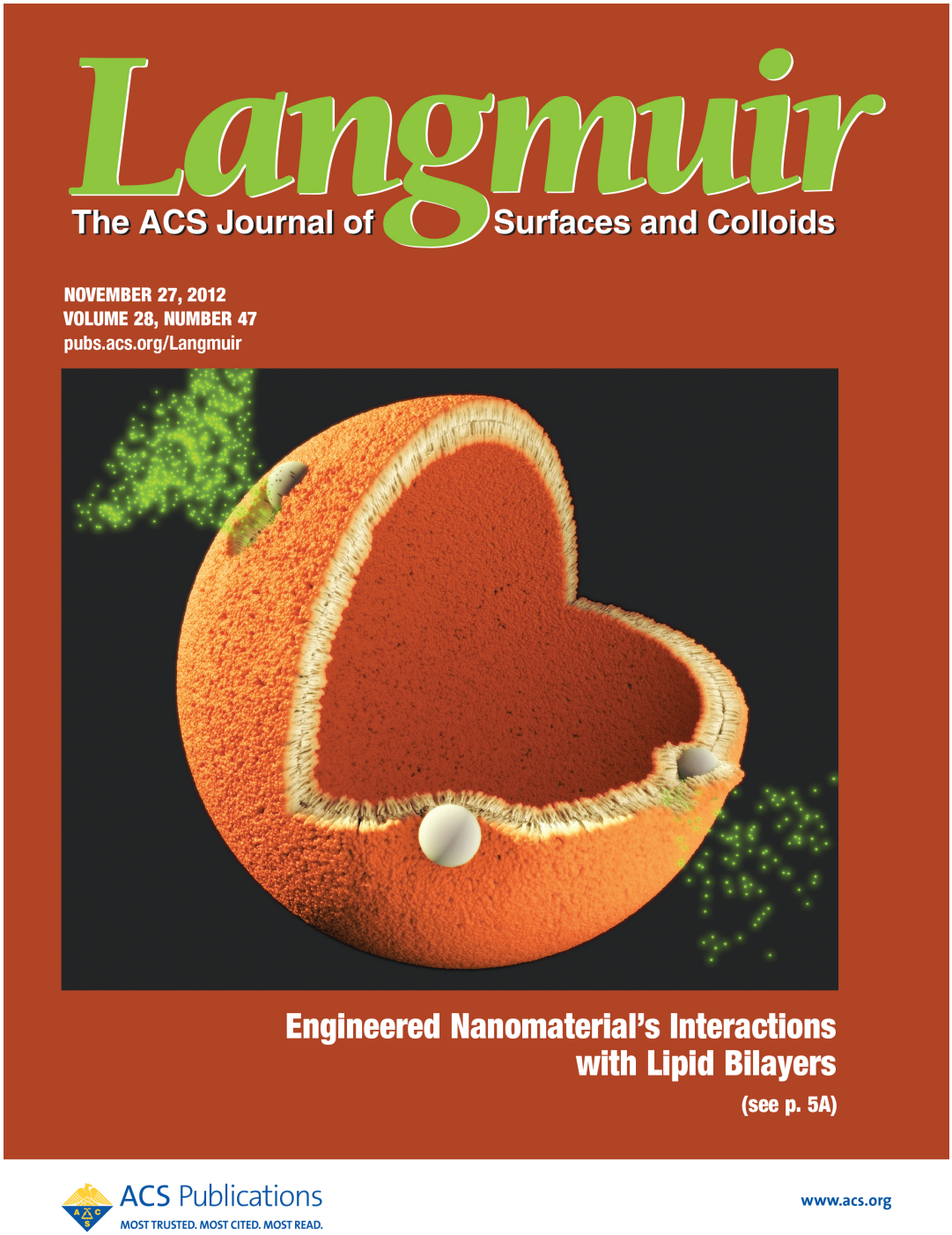

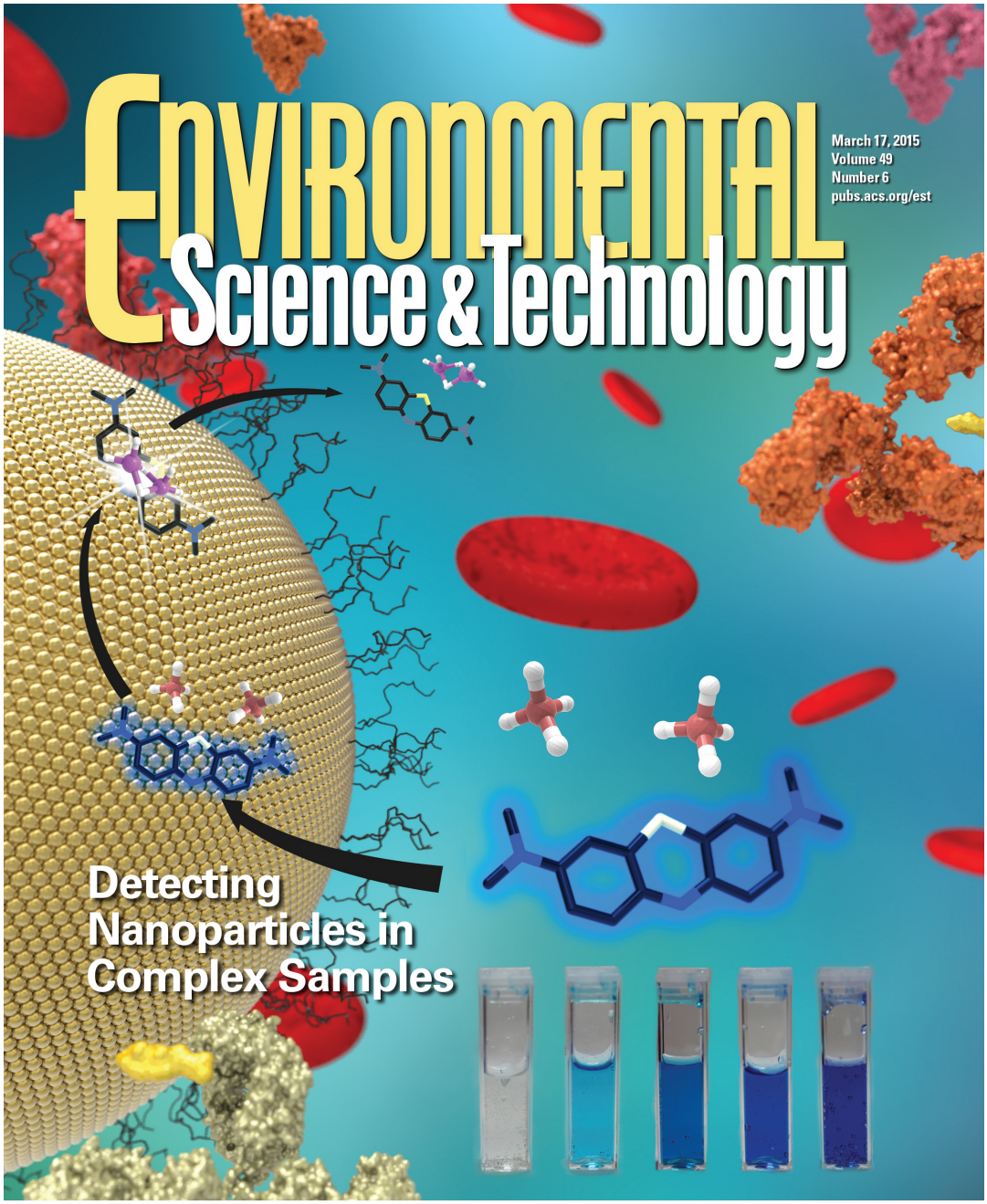

Chapter 5

Appendix: Matlab Files

5.1 Background

Over the last five years at the Posner Research Group, my peers and I have managed to write many Matlab scripts for a variety of experimental analysis and applications. It would be unnecessary to include all of the scripts here, but there are two scripts in particular that serve as great references for the work presented in this dissertation.

The first script is to process and quantify the current passing through a suspended lipid bilayer (pBLM) due to the interaction of ENPs, refer to Chapter 2. This script serves as a great example because it employs integration and extraction of current flux raw data from a custom LabView script as well as statistical analysis to extract comparable ENP – membrane interaction values (*e.g.,* FEI and Average conductance) that can be potentially used to understand the difference in mechanistic interaction behavior on nanoparticles with cell membranes.

The second script is used to compute and quantify surface catalytic reactivity values of ENPs (*e.g.,* β and τ) in a variety of complex solutions and nanoparticles extracted from commercial products, as shown in Chapter 3. This Matlab script can easily be adapted to account for the presence or absence of ENPs in environmental and biological media, which

is a step towards the development of a sensitive, simple, and reliable methodology to detect ENPs in complex samples.

5.2 ENP–Membrane Interaction Quantification

```
%% This code is used to extract anaytical values of ENP-Lipid Bilayer
%% interactions (e.g., FEI and average conductance)
%% of ENPs.
%
%% Posner Research Group
%% University of Washington, Department of Chemical & Mechanical Engineering
%% Created: 02/13/2012
%% Last Updated: 05/14/2013
%
%% Administrative
clear all
close all

clear all; close all; clc;
%%Start Code%%
function SmallAmp_loopv2_function_Charlie(flatstart,flatend,flatfolder,
    runstart,runend,experiment,amplitude,bins,cut1,cut2,filefolder,doRxx,doFFT
    ,psize,Vfrac)
%function [cond_Sig,maxflat,current_mean] = SmallAmp_loopv2_function(flatstart
    ,flatend,flatfolder,runstart,runend,experiment,amplitude,bins,cut1,cut2,
    filefolder,doRxx,doFFT,psize,Vfrac)
%%%%%

%%%%%
%function [CondTT,tplot,current_dataTT,current_dataTTp,current_dataAVE,xplot,
    pdfc,cdfc, Rxx1,lags,FFTfreq,yFFT] = SmallAmp_loopv2_function(runstart,
    runend,experiment,amplitude,bins,cut1,cut2,filefolder)
```

```
%[CondTT,tplot,current_dataTT,current_dataTTp,xplot,pdfc,cdfc] =
    SmallAmp_loopv2_function(runstart,runend,experiment,amplitude,bins,cut1,
    cut2,filefolder)

%NOTES%
%psize ids string with particle diameter in nm
% Vfrac is string with volume fraction
%SmallAmp_loopv2_function(runstart,runend,experiment,amplitude,bins,cut1,cut2,
    filefolder)
% runstart is first numbered entry, runend is last, both integers
% experiment is a string that has the experiment name for results folder
% amplitude is bias voltage applied, bins is for Conductance histogram
%cut1 and cut2 cuts off the jumps at beginning and end of measurement
%
%change std back from 5 to 3 and change savefolder back uncomment cdf pdf
tic
%
%savefolder=['C:\Documents and Settings\ccorred1\Desktop\Suspended Bilayer\
    Results\'];
%folder=['C:\Documents and Settings\ccorred1\Desktop\Suspended Bilayer\'
    flatfolder];

current_scale = 2;
%     if (current_scale==1)
%         scale=1e12;
%         voltage_scale=1e3;
%     else (current_scale==2)
%             scale=1;
%             voltage_scale=1;
%     end

    if (current_scale==1)
        scale=1e12;
```

```
        voltage_scale=1;
    elseif (current_scale==2)
            scale=1;
            voltage_scale=1;
    end

flatcount=flatstart;


%begin data loop
while (flatcount<=flatend)

flatcount
cd(folder);


pathname=[folder];

path(path,pathname);

if flatcount>99
    file_name=[int2str(flatcount),'.txt'];
elseif flatcount > 9
    file_name=['0',int2str(flatcount),'.txt'];
else
    file_name=['00',int2str(flatcount),'.txt'];
end


fid = fopen (file_name);
```

```
%data_file_type = input('What is the current output, 1 for Old (Labview 6.1),
   2 for Newer (Labview 8)    ');
data_file_type = 2;
    if (data_file_type==1)
        gain_alpha = fgetl(fid);
        gain_beta = fgetl(fid);
        Filter_kHz = fgetl(fid);
        Scan_rate = fgetl(fid);
        Number_of_points = fgetl(fid);
        Applied_Voltage = fgetl(fid);
        Info_1 = fgetl(fid);
        Info_2 = fgetl(fid);
        Resistance = fgetl(fid);
        Capacitance = fgetl(fid);
        Data_labels = fgetl(fid);


    elseif (data_file_type==2)
        File_name = fgetl(fid);
        Applied_Voltage = fgetl(fid);
        Space_Fill1 = fgetl(fid);
        Space_Fill2 = fgetl(fid);
        Space_Fill3 = fgetl(fid);
        Space_Fill4 = fgetl(fid);
        Space_Fill5 = fgetl(fid);
        Space_Fill6 = fgetl(fid);
        Space_Fill7 = fgetl(fid);
        Added_signal = fgetl(fid);
        gain_alpha = fgetl(fid);
        Device = fgetl(fid);
        Solution = fgetl(fid);
        Comments = fgetl(fid);
```

```
        Resistance = fgetl(fid);
    end



matrix2 = fscanf(fid,'%c');
file_data=strread(matrix2);
voltage_data=file_data(:,1);
voltage_data=voltage_data/voltage_scale;
current_data=file_data(:,2);
current_data=current_data*scale;
conductance = current_data/amplitude;




pts=cut2-cut1+1;


current_dataAVEflat((flatcount-flatstart)+1)=mean(current_data(cut1:cut2,1));
current_dataTTflat((flatcount-flatstart)*pts+1:pts+(flatcount-flatstart)*pts)=
    current_data(cut1:cut2,1);




flatcount=flatcount+1;
end

%end data loop

stdflat=std(current_dataTTflat);
maxflat=max(current_dataTTflat);
```

```
minflat=min(current_dataTTflat);
meanflat=mean(current_dataTTflat);



%change this
%put at 3
p3_std=meanflat+4*stdflat
n3_std=meanflat-4*stdflat




tTotflat=length(current_dataTTflat)/10000;
tplotflat=linspace(0,tTotflat,length(current_dataTTflat));



figure1=figure;
plot(tplotflat,current_dataTTflat);
%plot(runplot,current_dataTT);
ylim([-50 150]);
title(['Current vs time flat   run#s', int2str(flatstart), int2str(flatend),
    psize ' nm', ' vol frac ', Vfrac , '     ', experiment])
xlabel(['Time (s)'])
ylabel('I (pA)')

Condflat=current_dataTTflat./amplitude;

figure2=figure;
 hist(Condflat,bins)
 xlim([-0.5 5]);
 ylim([0 2500]);
title(['Conductance  flat  run#s', int2str(flatstart), int2str(flatend), psize
     ' nm  ', ' vol frac  ' Vfrac, '     ', experiment])
 xlabel(['Cond (nS)'])
```

```
 ylabel('Number of Occurrences')

f1=[savefolder '\' experiment];
if (exist(f1) == 0)
   mkdir (f1);
end

saveas(figure1,[savefolder '\' experiment '\' experiment '_currentFLAT.fig']);
saveas(figure1,[savefolder '\' experiment '\' experiment '_currentFLAT.tif']);


saveas(figure2,[savefolder '\' experiment '\' experiment '_condFLAT.fig']);
saveas(figure2,[savefolder '\' experiment '\' experiment '_condFLAT.tif']);

toc
cd('C:\Documents and Settings\ccorred1\Desktop\Suspended Bilayer\matlabfile
    scrpts\')
keep meanflat p3_std minflat maxflat runstart runend experiment amplitude bins
     cut1 cut2 filefolder doRxx doFFT psize Vfrac savefolder n3_std
%
% flat data above ^
%%%%%%%%%%%%%%%%%%%%%%%%%%%%%%%%%%%%%%%%%%%%%%%%
% run data below v
%
%savefolder=['C:\Nanoparticle Bilayer\Results'];
%folder=['C:\Documents and Settings\ccorred1\Desktop\Suspended Bilayer\'
    filefolder];
tic

current_scale = 2;
%     if (current_scale==1)
%         scale=1e12;
%         voltage_scale=1e3;
```

```
%      else (current_scale==2)
%              scale=1;
%              voltage_scale=1;
%      end

    if (current_scale==1)
        scale=1e12;
        voltage_scale=1;
    elseif (current_scale==2)
            scale=1;
            voltage_scale=1;
    end

run=runstart;


%%%%%%%%%%%%%%%%%% begin data loop
while(run<=runend)


cd(folder);


pathname=[folder];

path(path,pathname)

if run>99
    file_name=[int2str(run),'.txt'];
elseif run > 9
    file_name=['0',int2str(run),'.txt'];
else
    file_name=['00',int2str(run),'.txt'];
```

```
end



fid = fopen (file_name);




%data_file_type = input('What is the current output, 1 for Old (Labview 6.1),
   2 for Newer (Labview 8)    ');
data_file_type = 2;
    if (data_file_type==1)
        gain_alpha = fgetl(fid);
        gain_beta = fgetl(fid);
        Filter_kHz = fgetl(fid);
        Scan_rate = fgetl(fid);
        Number_of_points = fgetl(fid);
        Applied_Voltage = fgetl(fid);
        Info_1 = fgetl(fid);
        Info_2 = fgetl(fid);
        Resistance = fgetl(fid);
        Capacitance = fgetl(fid);
        Data_labels = fgetl(fid);



    elseif (data_file_type==2)
        File_name = fgetl(fid);
        Applied_Voltage = fgetl(fid);
        Space_Fill1 = fgetl(fid);
        Space_Fill2 = fgetl(fid);
        Space_Fill3 = fgetl(fid);
        Space_Fill4 = fgetl(fid);
        Space_Fill5 = fgetl(fid);
```

```
        Space_Fill6 = fgetl(fid);
        Space_Fill7 = fgetl(fid);
        Added_signal = fgetl(fid);
        gain_alpha = fgetl(fid);
        Device = fgetl(fid);
        Solution = fgetl(fid);
        Comments = fgetl(fid);
        Resistance = fgetl(fid);
    end



matrix2 = fscanf(fid,'%c');
file_data=strread(matrix2);
voltage_data=file_data(:,1);
voltage_data=voltage_data/voltage_scale;
current_data=file_data(:,2);
current_data=current_data*scale;
conductance = current_data/amplitude;

toc



tic

pts=cut2-cut1+1;
meas_time=9000+(length(current_data)-cut2)+cut1;

current_dataAVE((run-runstart)+1)=mean(current_data(cut1:cut2,1));

fclose all;
if run==1
```

```
    CondTT((run-runstart)*pts+1:pts+(run-runstart)*pts)=conductance(cut1:cut2
    ,1);
    current_dataTTp((run-runstart)*pts+1:pts+(run-runstart)*pts)=current_data(
    cut1:cut2,1);
    current_dataTT((run-runstart)*pts+1:pts+(run-runstart)*pts)=current_data(
    cut1:cut2,1);
elseif run >= 1
    CondTT((run-runstart)*pts+1:pts+(run-runstart)*pts)=conductance(cut1:cut2
    ,1);
    current_dataTTp(pts+(run-runstart)*pts+meas_time*(run-runstart)+1:pts+
    meas_time+(run-runstart)*pts+meas_time*(run-runstart))=zeros(1,meas_time);
    current_dataTTp((run-runstart)*pts+1+meas_time*(run-runstart):pts+(run-
    runstart)*pts+(run-runstart)*meas_time)=current_data(cut1:cut2,1);
    current_dataTT((run-runstart)*pts+1:pts+(run-runstart)*pts)=current_data(
    cut1:cut2,1);
end


run=run+1

end

%%%%%%%%%%%%%%%%%% end data loop


currentSUM=0;
current_count=0;




if amplitude >0
```

```
%      for i=1:length(current_dataTT)
%       if current_dataTT(i)>=p3_std & current_dataTT(i) < 9000
%           current_count=current_count+1;
%           cond_Sig(current_count)=current_dataTT(i)./amplitude;
%       end
%      end

 cond_Sig = current_dataTT(current_dataTT >= p3_std & current_dataTT < 9000)./
    amplitude;

% cond_Sig = current_dataTT(current_dataTT >= p3_std & current_dataTT < 9000)
    ./amplitude;

elseif amplitude <0
      for i=1:length(current_dataTT)
          if current_dataTT(i)<=n3_std & current_dataTT(i) > -9000
          current_count=current_count+1;
          cond_Sig(current_count)=current_dataTT(i)./amplitude;
          end
      end
end

Ttotal=length(current_dataTT)./10000;
Tsignal=length(cond_Sig)./10000;

%
% current_mean=currentSUM/current_count
% current_mean=mean(current_Sig)
cond_max=max(cond_Sig)
cond_mean=mean(cond_Sig)
cond_mode=mode(cond_Sig);
cond_median=median(cond_Sig);
current_mean=cond_mean*amplitude
```

```
toc

tic

%fid1=fopen('C:\Documents and Settings\ccorred1\Desktop\Suspended Bilayer\
    Results\Output_NP.csv','a');
if amplitude > 0
     fprintf(fid1,['\n' experiment ',' psize ',' num2str(cond_mean) ',' num2str
    (cond_max) ',' num2str(cond_mode) ',' num2str(cond_median) ',' num2str(
    current_mean) ',' int2str(amplitude) ',' num2str(p3_std) ',' Vfrac ','
    num2str(Ttotal) ',' num2str(Tsignal) ',' int2str(runstart) ',' int2str(
    runend)]);
elseif amplitude < 0
     fprintf(fid1,['\n' experiment ',' psize ',' num2str(cond_mean) ',' num2str
    (cond_max) ',' num2str(cond_mode) ',' num2str(cond_median) ',' num2str(
    current_mean) ',' int2str(amplitude) ',' num2str(n3_std) ',' Vfrac ','
    num2str(Ttotal) ',' num2str(Tsignal) ',' int2str(runstart) ',' int2str(
    runend)]);
end
fclose(fid1);




bigS=size(current_dataTT);



runplot=linspace(runstart,runstart+(runend-runstart),bigS(1,2));
tTot=length(current_dataTTp)./10000;
tplot=linspace(0,tTot,length(current_dataTTp));
tplot2=linspace(0,tTot,length(current_dataTT));
```

```
figure1=figure;
% plot(tplot,current_dataTTp);
plot(runplot,current_dataTT);
if amplitude > 0
    ylim([-50 3500]);
elseif amplitude < 0
    ylim ([-3500 50]);
end
title(['Current vs time    ', psize ' nm  ', ' vol frac  ' Vfrac, '    run #s
    ',  num2str(runstart), ' ' , num2str(runend), '     ', experiment])
xlabel(['Time (s)'])
ylabel('I (pA)')

%%This is to paste the line with out breaks%
% figure1=figure;
% plot(tplot2,current_dataTT);
% plot(runplot,current_dataTT);
% ylim([-10 150])
% xlim([0 1200])
% xlabel('Time (s)','FontName','Helvetica','FontSize',32,'FontWeight','bold')
% ylabel('I (pA)','FontName','Helvetica','FontSize',32,'FontWeight','bold')
% set(gca,'FontName','Helvetica','FontSize',32,'FontWeight','bold')




figure2=figure;
 hist(CondTT,bins)
 xlim([-0.5 20]);
 ylim([0 2500]);
```

```
title(['Conductance    Avg Cond ~ ' num2str(cond_mean), psize ' nm  ', ' vol
    frac  ' Vfrac, ' # bins  ', num2str(bins), '        run #s ' , num2str(
    runstart),' ' , num2str(runend), '     ', experiment])
 xlabel(['Cond (nS)'])
 ylabel('Number of Occurrences')


AveTime=linspace(0,[meas_time/10000*(runend-runstart+1)+5*(runend-runstart+1)
    ],length(current_dataAVE));
figure3=figure;
plot(AveTime,current_dataAVE,'kx-');
%plot(runplot,current_dataTT);
%ylim([-50 2500]);
title(['Current Average    ', '    run #s ', num2str(runstart),' ' , num2str
    (runend), '  ', psize ' nm  ', ' vol frac  ' Vfrac, '     ', experiment])
xlabel(['Time (s)'])
ylabel('I (pA)')


figure4=figure;
 hist(cond_Sig,bins)
 xlim([-0.5 20]);
 ylim([0 2500]);
title(['Conductance - no noise,   Avg Cond ~ ' num2str(cond_mean), ' ', psize
    ' nm  ', ' vol frac  ', Vfrac,  ' # bins  ', num2str(bins),'        run #s
     ' , num2str(runstart),' ' , num2str(runend), '  ', experiment])
 xlabel(['Cond (nS)'])
 ylabel('Number of Occurrences')



figure5=figure;
 plot(cond_Sig*amplitude)
```

```
 %xlim([-0.5  20]);
if amplitude > 0
    ylim([-50  3500]);
elseif amplitude < 0
    ylim ([-3500  50]);
end
title(['Conductance - no noise,    Avg Cond ~ ' num2str(cond_mean), ' ', psize
    ' nm  ', ' vol frac  ', Vfrac,  ' # bins  ', num2str(bins),'        run #s
     ' ,  num2str(runstart),' ' ,  num2str(runend), '  ', experiment])
 xlabel(['data points'])
 ylabel('Current (pA)')



% figure6=figure;
% plot(tplot,current_dataTT);
% %plot(runplot,current_dataTT);
% if amplitude > 0
%     ylim([-50  3500]);
% elseif amplitude < 0
%     ylim ([-3500  50]);
% end
% title(['Current vs time    ', psize ' nm  ', ' vol frac  ' Vfrac, '    run #
    s ',  num2str(runstart), ' ' , num2str(runend), '     ', experiment])
% xlabel(['Time (s)'])
% ylabel('I (pA)')


f1=[savefolder '\' experiment];
if (exist(f1) == 0)
   mkdir (f1);
end
```

```
saveas(figure1,[savefolder '\' experiment '\' experiment '_current.fig']);
saveas(figure2,[savefolder '\' experiment '\' experiment '_cond.fig']);
saveas(figure1,[savefolder '\' experiment '\' experiment '_current.tif']);
saveas(figure2,[savefolder '\' experiment '\' experiment '_cond.tif']);

saveas(figure3,[savefolder '\' experiment '\' experiment '_currentAVE.fig']);
saveas(figure3,[savefolder '\' experiment '\' experiment '_currentAVE.tif']);


saveas(figure4,[savefolder '\' experiment '\' experiment '_cond_nonoise.fig'
  ]);
saveas(figure4,[savefolder '\' experiment '\' experiment '_cond_nonoise.tif'
  ]);

saveas(figure5,[savefolder '\' experiment '\' experiment '_current_nonoise.
  fig']);
saveas(figure5,[savefolder '\' experiment '\' experiment '_current_nonoise.
  tif']);


save([savefolder '\' experiment '\' experiment '.mat']);



%cd('C:\Nanoparticle Bilayer\Useful Codes Etc')
%[rmsc]=rms_sk(current_dataTT);

%[pdfc,cdfc,xplot]=pdf_sk(current_dataTT,round(0.08*rmsc));
%[pdfc,cdfc,xplot]=pdf_sk(current_dataTT,1000);


if doRxx==1
```

```
M=length(current_dataTT);



[Rxx1,lags]=xcorr(current_dataTT,((M)/2)-1,'coeff');

figure5=figure
plot(lags,Rxx1)
%ylim([-200 1000]);
 %xlim()
 title(['Autocorrelation Coefficient ', psize ' nm ', ' vol frac ' Vfrac, '
    ', experiment])
 xlabel(['lags'])
 ylabel('Rxx')

saveas(figure5,[savefolder '\' experiment '\' experiment '_Rxx.fig']);
saveas(figure5,[savefolder '\' experiment '\' experiment '_Rxx.tif']);

end
%
% figure6=figure;
% plot(xplot,pdfc)
% %xlim([-0.5 35]);
%  title(['PDF of current signal ', psize ' nm ', ' vol frac ' Vfrac, ' ',
    experiment])
%  xlabel(['bin #', run])
%  ylabel('pdf(x)')
%
%  figure7=figure
%  plot(xplot,cdfc)
% %xlim([-0.5 35]);
%  title(['CDF of current signal ' psize ' nm ', ' vol frac ' Vfrac, ' ',
    experiment])
%  xlabel(['bin #', run])
```

```
%  ylabel('cdf(x)')
%



 %saveas(figure6,[savefolder '\' experiment '\' experiment '_pdf.fig']);

 %saveas(figure6,[savefolder '\' experiment '\' experiment '_pdf.tif']);
 %saveas(figure7,[savefolder '\' experiment '\' experiment '_cdf.fig']);
 %saveas(figure7,[savefolder '\' experiment '\' experiment '_cdf.tif']);


 %save([folder '\' experiment]);

 % save([savefolder '\' experiment '\' experiment]);


if doFFT==1
 figure8=figure

NFFT=2^nextpow2(length(current_dataTT))
FFTc=fft(current_data,NFFT)/length(current_dataTT);
FFTfreq=500/2*linspace(0,1,NFFT/2);
yFFT=2*abs(FFTc(1:NFFT/2));
plot(FFTfreq,yFFT)

 title(['FFT of current signal ' psize ' mm  ', ' vol frac  ' Vfrac, ' ' ,
   experiment])
 xlabel(['Freq (Hz)', int2str(run)])
 ylabel('Amplitude')

 saveas(figure8,[savefolder '\' experiment '\' experiment '_fft.fig']);
 saveas(figure8,[savefolder '\' experiment '\' experiment '_fft.tif']);
```

```
end

 save([savefolder '\' experiment '\' experiment]);

 close all
toc
```

5.3 Colorimetric Assay Quantification

```
% This code is used to analytical beta & tau values from catalytic surface
% of ENPs.
% This code fits a function of the form f = A*exp((-t+t0)/tau)) + B to data
    from txt files created by Kinetics UVvis experiments

% Posner Research Group
% University of Washington, Department of Chemical & Mechanical Engineering
% Created: 03/13/2013
% Last Updated: 06/14/2015

%% Administrative
clear all
close all

clear all; close all; clc;

files = dir('*.txt'); % Creates a list of the .txt files in the current folder

% Creates new folder in the current folder to store coefficients
mkdir('Data_2', 'Figures') %Creates Data folder and Figures folder
cd Data_2 %Changes directory to Data folder to create additional folders
mkdir('Figures', 'fig') %Creates fig folder
mkdir('Figures', 'tiff') %Creates tiff folder
cd .. %Changes directory back to original folder

screen_size = get(0, 'ScreenSize'); % Gets screen size info for full screen
    plots

for i = 1:numel(files); %Runs for the number of .txt files found in the
    current folder
    %Saves data from .txt files
```

```
    delimiter = '\t';
    startRow = 6;
    formatSpec = '%s%f%f%[^\n\r]';
    fid = fopen(files(i).name, 'r');

    A = textscan(fid, formatSpec, 'Delimiter', delimiter, 'EmptyValue' ,NaN,'
    HeaderLines' ,startRow-1, 'ReturnOnError', false); % reads first column of
     excel data in specified file
    fclose(fid);
    xdata = A{2}; %Frequency data
    ydata = A{3}; %Absorbance data
%     ydata = ydata./max(ydata); %Normalizes y data
%     xdata = xdata./max(xdata); %Normalizes x data
%     ydata = smooth(ydata,50);

    for m=1:20

        % Plots data and allows user to select domain of curve fit
        figure(1)
        subplot(2,2,[1 3]);
        hold on
        plot(xdata,log(ydata),'.k');
        xlabel('Time [s]','FontWeight','bold','FontSize',18);
        ylabel('ln(OD)','FontWeight','bold','FontSize',18);
        subplot(2,2,[2 4]);
        plot(xdata,ydata,'.k');
        xlabel('Time [s]','FontWeight','bold','FontSize',18);
        ylabel('OD','FontWeight','bold','FontSize',18);
        set(figure(1),'Position', [0 0 screen_size(3) screen_size(4) ] ); %
    Makes plot full screen
        hold off
        jw = datacursormode;
        datacursormode on; %Enables user to select data points
```

```
pause
p1 = getCursorInfo(jw); %Stores first data point info
figure(1)
pause
p2 = getCursorInfo(jw); %Stores second data point info
figure(1)
datacursormode off;

close all
clf('reset')

% Creates new matrices with data from selected domain
X = xdata((p1.DataIndex+1):p2.DataIndex);
XX1 = xdata(p1.DataIndex) - X;
XX2 = xdata(p1.DataIndex) - xdata((p1.DataIndex+1):length(xdata));
Y = ydata((p1.DataIndex+1):p2.DataIndex);

% Defines function and performs least-squares curve fit
F = @(c,x) c(1)*exp(x/c(2)) + c(3);

c0 = [0.1 0.1 0]; % Initial guess for coefficients

options = optimset('TolFun',1e-12,'TolX',1e-12,'MaxFunEvals',100000,'
MaxIter',100000);
[c, RESNORM] = lsqcurvefit(F,c0,XX1,Y,[-1000 0 0],[],options);

Rsqr(i) = 1 - RESNORM/((length(Y)-1)*var(Y)); % R^2 equation from
Mathworks site

%Creates a string with the R^2 value to display on the plots
R2(1) = {'R^2 ='};
R2(2) = {Rsqr(i)};
```

```
    C(i,2) = Rsqr(i);

    %Plots the data with curve fit
    subplot(2,2,[1 3]);
    hold on
    plot(xdata,ydata,'k.',p1.Position(1),exp(p1.Position(2)),'ko',p2.
Position(1),exp(p2.Position(2)),'ko') %Plots data with user selected
points
    plot(xdata((p1.DataIndex+1):length(xdata)),F(c,XX2),'r-') %Plots curve
 fit
    legend('off')
    xlabel('Time (s)','FontWeight','bold','FontSize',18);
    ylabel('Abs (a.u.)','FontWeight','bold','FontSize',18);
    hold off

    %Plots the data with curve fit, zoomed in on the user-selected domain
    subplot(2,2,[2 4]);
    hold on

    %Displays R^2 value on plot
    x1 = p2.Position(1);
    y1 = exp(p2.Position(2)) + 0.75*(exp(p1.Position(2))-exp(p2.Position
(2)));
    text(x1,y1,R2)

    %Creates zoomed-in plot
    xmin = p1.Position(1)-5;
    xmax = p2.Position(1)+5;
    ymin = exp(p2.Position(2))-0.01;
    ymax = exp(p1.Position(2))+0.01;
    axis([xmin,xmax,ymin,ymax])
```

```
    plot(xdata,ydata,'k.',p1.Position(1),exp(p1.Position(2)),'ko',p2.
Position(1),exp(p2.Position(2)),'ko') %Plots data with user selected
points
    plot(X,F(c,XX1),'r-') %Plots curve fit
    legend('off')
    xlabel('Time (s)','FontWeight','bold','FontSize',18);
    ylabel('Abs (a.u.)','FontWeight','bold','FontSize',18);
    set(figure(1),'Position', [0 0 screen_size(3) screen_size(4) ]); %
Makes plot full screen
    hold off

    %Opens a window for user to select the quality of the curve fit
    %Good - saves figures and coeff values, moves to next .txt file
    %Poor - allows user to reselect data points for curve fit
    %Trash - saves no data and moves to next .txt file
    choice = menu('Data fit quality', 'Good', 'Poor', 'Trash');

    close all

    if choice == 1; %Good option

        %Replots both graphs seperately to save as both .fig and .tif
files
        for n=1:3
            hold on
            plot(xdata,ydata,'k.',p1.Position(1),exp(p1.Position(2)),'ko',
p2.Position(1),exp(p2.Position(2)),'ko') %Plots data with user selected
points

            if n==3 %Creates zoomed-in plot for second figure
                axis([xmin,xmax,ymin,ymax])
                y1 = (ymin+ymax)/2; %Positions R^2 value
                text(x1,y1,R2) %Displays R^2 value
```

```
            end

            if n==2
                plot(xdata((p1.DataIndex+1):length(xdata)),F(c,XX2),'r-')
            else
                plot(X,F(c,XX1),'r-') %Plots curve fit
            end

            legend('off')

            %Graph display options
            box on %Creates solid box around graph
            set(gca,'linewidth',1.5,'FontWeight', 'bold', 'FontSize', 16)
%Sets width of box around graph and axis label text size
            xlabel('Time (s)','FontWeight','bold','FontSize',18);
            ylabel('Abs (a.u.)','FontWeight','bold','FontSize',18);
            hold off

            %Saves .fig and .tif files
            cd Data_2; cd Figures; cd tiff; %Changes directory to save .
tif file
            filename = sprintf('%0d-%0d_eq1.tif',i,n); %Labels tif files
as 1-1,1-2,2-1,2-2...
            print('-dtiff', filename); %Saves .tif file
            cd ..; cd fig %Changes directory to save .fig file
            filename = sprintf('%0d-%0d_eq1.fig',i,n); %Labels tif files
as 1-1,1-2,2-1,2-2...
            hgsave(filename); %Saves .fig file
            cd ..; cd ..; cd .. %Changes directory back to original folder

            close all

        end
```

```
            C(i,1) = c(2); % Saves tau value
            C(i,3) = c(3); % Saves B value

            break
        end

        if choice == 3; %Trash option
            close all
            C(i,1) = 0; %Saves tau value as 0
            break
        end
end

end

cd Data_2 %Changes directory to save file
dlmwrite('coeff_eq1.txt', C,'delimiter','\t'); %Saves coeff_eq1.txt file
cd .. %Changes directory back to original folder
```

Bibliography

[1] Norio Taniguchi and others. On the basic concept of nanotechnology. In *Proc. Intl. Conf. Prod. Eng. Tokyo, Part II, Japan Society of Precision Engineering*, pages 18–23, 1974.

[2] Scientific Committee on Emerging and Newly Identified Health Risks. Opinion on the appropriateness of the Risk Assessment Methodology in accordance with the technical guidance documents for new and existing substances for assessing the risks of nanomaterials. *Scientific Committee on Emerging and Newly Identified Health Risks*, 2007.

[3] ISO Nanotechnologies Terminology. definitions for nano-objects: Nanoparticle, nanofibre and nanoplate. *International Organization for Standardization*, 2008.

[4] Karen Tiede, Alistair BA Boxall, Steven P. Tear, John Lewis, Helen David, and Martin Hassellv. Detection and characterization of engineered nanoparticles in food and the environment. *Food Additives and Contaminants*, 25(7):795–821, 2008.

[5] Michael F. Hochella. Nanoscience and technology: the next revolution in the Earth sciences. *Earth and Planetary Science Letters*, 203(2):593–605, 2002.

[6] Paul JA Borm, David Robbins, Stephan Haubold, Thomas Kuhlbusch, Heinz Fissan, Ken Donaldson, Roel Schins, Vicki Stone, Wolfgang Kreyling, Jurgen Lademann, Jean Krutmann, David Warheit, and Eva Oberdorster. The potential risks of nanomaterials: a review carried out for ECETOC. *Particle and Fibre Toxicology*, 3(1):11, August 2006.

[7] Marina E Vance, Todd Kuiken, Eric P Vejerano, Sean P McGinnis, Michael F Hochella, David Rejeski, and Matthew S Hull. Nanotechnology in the real world: Redeveloping the nanomaterial consumer products inventory. *Beilstein Journal of Nanotechnology*, 6:1769–1780, August 2015.

[8] Vicki L Colvin. The potential environmental impact of engineered nanomaterials. *Nature biotechnology*, 21(10):1166–1170, 2003.

[9] Catia Contado. Nanomaterials in consumer products: a challenging analytical problem. *Analytical Chemistry*, page 48, 2015.

[10] Christopher Szakal, Stephen M Roberts, Paul Westerhoff, Andrew Bartholomaeus, Neil Buck, Ian Illuminato, Richard Canady, and Michael Rogers. Measurement of

nanomaterials in foods: integrative consideration of challenges and future prospects. *Acs Nano*, 8(4):3128–3135, 2014.

[11] David J. Burleson, Michelle D. Driessen, and R. Lee Penn. On the characterization of environmental nanoparticles. *Journal of Environmental Science and Health, Part A*, 39(10):2707–2753, 2004.

[12] Prashant V. Kamat. Photophysical, photochemical and photocatalytic aspects of metal nanoparticles. *The Journal of Physical Chemistry B*, 106(32):7729–7744, 2002.

[13] Jillian F. Banfield and Hengzhong Zhang. Nanoparticles in the Environment. *Reviews in Mineralogy and Geochemistry*, 44(1):1–58, January 2001.

[14] Andrew S. Madden and Michael F. Hochella. A test of geochemical reactivity as a function of mineral size: Manganese oxidation promoted by hematite nanoparticles. *Geochimica et Cosmochimica Acta*, 69(2):389–398, 2005.

[15] Andre Nel, Tian Xia, Lutz Mdler, and Ning Li. Toxic Potential of Materials at the Nanolevel. *Science*, 311(5761):622–627, February 2006.

[16] Paul J A Borm and Wolfgang Kreyling. Toxicological hazards of inhaled nanoparticles–potential implications for drug delivery. *Journal of nanoscience and nanotechnology*, 4(5):521–531, May 2004.

[17] Wim H De Jong and Paul JA Borm. Drug delivery and nanoparticles: Applications and hazards. *International Journal of Nanomedicine*, 3(2):133–149, June 2008.

[18] Julius A. Edson and Young Jik Kwon. RNAi for silencing drug resistance in microbes toward development of nanoantibiotics. *Journal of Controlled Release*, 2014.

[19] Jose R. Peralta-Videa, Lijuan Zhao, Martha L. Lopez-Moreno, Guadalupe de la Rosa, Jie Hong, and Jorge L. Gardea-Torresdey. Nanomaterials and the environment: A review for the biennium 2008–2010. *Journal of Hazardous Materials*, 186(1):1–15, February 2011.

[20] W. Dab, N. Fabre, A. George-Guiton, E. Gaffet, S. Desmoulin, J. Cambou, D. Benoit-Browaeys, G. Hriard-Dubreuil, L. Pitoun, G. Gurive, L. Trpied, A. Pochet, B. Laurent, J. Boudot, M. Fontaine, R. Chevallier, J. L. Pujol, and D. Houssin. Risques et bnfices des nanotechnologies : le besoin de nouvelles formes de dbat social. *Annales des Mines - Responsabilit et environnement*, N 55(3):55–61, September 2009.

[21] Arturo A. Keller and Anastasiya Lazareva. Predicted Releases of Engineered Nanomaterials: From Global to Regional to Local. *Environmental Science & Technology Letters*, 1(1):65–70, January 2014.

[22] Laura Hodson, Mark Methner, and Ralph D Zumwalde. *Approaches to safe nanotechnology: managing the health and safety concerns associated with engineered nanomaterials*. Department of Health and Human Services, Centers for Disease Control and Prevention, National Institute for Occupational Safety and Health, 2009.

[23] Philip Shapira, Jan Youtie, and Alan L. Porter. The emergence of social science research on nanotechnology. *Scientometrics*, 85(2):595–611, March 2010.

[24] Can Huang, Ad Notten, and Nico Rasters. Nanoscience and technology publications and patents: a review of social science studies and search strategies. *The Journal of Technology Transfer*, 36(2):145–172, January 2010.

[25] Joyce S. Tsuji, Andrew D. Maynard, Paul C. Howard, John T. James, Chiu-wing Lam, David B. Warheit, and Annette B. Santamaria. Research Strategies for Safety Evaluation of Nanomaterials, Part IV: Risk Assessment of Nanoparticles. *Toxicological Sciences*, 89(1):42–50, January 2006.

[26] Frederic Vandermoere, Sandrine Blanchemanche, Andrea Bieberstein, Stephan Marette, and Jutta Roosen. The public understanding of nanotechnology in the food domain the hidden role of views on science, technology, and nature. *Public Understanding of Science*, 20(2):195–206, 2011.

[27] Carey C Jordan, Iona Kaiser, and Valerie C Moore. 2013 nanotechnology patent literature review: Graphitic carbon-based nanotechnology and energy applications are on the rise. *Nanotech. L. & Bus.*, 11:111, 2014.

[28] An inventory of nanotechnology-based consumer products currently on the market of the Project of Emerging Nanotechnology, January 2014.

[29] Mark W. Frampton, Judith C. Stewart, Gnter Oberdrster, Paul E. Morrow, David Chalupa, Anthony P. Pietropaoli, Lauren M. Frasier, Donna M. Speers, Christopher Cox, Li-Shan Huang, and others. Inhalation of ultrafine particles alters blood leukocyte expression of adhesion molecules in humans. *Environmental Health Perspectives*, pages 51–58, 2006.

[30] Anton W. Jensen, Stephen R. Wilson, and David I. Schuster. Biological applications of fullerenes. *Bioorganic & medicinal chemistry*, 4(6):767–779, 1996.

[31] Tatiana Da Ros and Maurizio Prato. Medicinal chemistry with fullerenes and fullerene derivatives. *Chemical Communications*, (8):663–669, 1999.

[32] N. Tagmatarchis and H. Shinohara. Fullerenes in medicinal chemistry and their biological applications. *Mini reviews in medicinal chemistry*, 1(4):339–348, 2001.

[33] Rania Bakry, Rainer M. Vallant, Muhammad Najam-ul Haq, Matthias Rainer, Zoltan Szabo, Christian W. Huck, and Gnther K. Bonn. Medicinal applications of fullerenes. *International journal of nanomedicine*, 2(4):639, 2007.

[34] Huanan Guan, Defu Chi, Jia Yu, and Xiaocan Li. A novel photodegradable insecticide: Preparation, characterization and properties evaluation of nano-Imidacloprid. *Pesticide Biochemistry and Physiology*, 92(2):83–91, 2008.

[35] Paul Westerhoff and Jennifer James. Nitrate removal in zero-valent iron packed columns. *Water Research*, 37(8):1818–1830, 2003.

[36] Troy M. Benn and Paul Westerhoff. Nanoparticle Silver Released into Water from Commercially Available Sock Fabrics. *Environmental Science & Technology*, 42(11):4133–4139, June 2008.

[37] Kevin J. Cash and Heather A. Clark. Nanosensors and nanomaterials for monitoring glucose in diabetes. *Trends in molecular medicine*, 16(12):584–593, 2010.

[38] Sanjeeb K. Sahoo and Vinod Labhasetwar. Nanotech approaches to drug delivery and imaging. *Drug discovery today*, 8(24):1112–1120, 2003.

[39] Bing Wang, Xiao He, Zhiyong Zhang, Yuliang Zhao, and Weiyue Feng. Metabolism of nanomaterials in vivo: blood circulation and organ clearance. *Accounts of chemical research*, 46(3):761–769, 2012.

[40] Cristina Buzea, Ivan I. Pacheco, and Kevin Robbie. Nanomaterials and nanoparticles: Sources and toxicity. *Biointerphases*, 2(4):MR17–MR71, December 2007.

[41] Alex Weir, Paul Westerhoff, Lars Fabricius, Kiril Hristovski, and Natalie von Goetz. Titanium Dioxide Nanoparticles in Food and Personal Care Products. *Environmental Science & Technology*, 46(4):2242–2250, February 2012.

[42] Dietram A. Scheufele, Elizabeth A. Corley, Sharon Dunwoody, Tsung-Jen Shih, Elliott Hillback, and David H. Guston. Scientists worry about some risks more than the public. *Nature Nanotechnology*, 2(12):732–734, December 2007.

[43] Charlie Corredor, Wen-Che Hou, Steven A. Klein, Babak Y. Moghadam, Michael Goryll, Kyle Doudrick, Paul Westerhoff, and Jonathan D. Posner. Disruption of model cell membranes by carbon nanotubes. *Carbon*, 60:67–75, August 2013.

[44] Christine Ogilvie Hendren, Xavier Mesnard, Jocelyn Drge, and Mark R. Wiesner. Estimating Production Data for Five Engineered Nanomaterials As a Basis for Exposure Assessment. *Environmental Science & Technology*, 45(7):2562–2569, April 2011.

[45] David M. Brown, Martin R. Wilson, William MacNee, Vicki Stone, and Ken Donaldson. Size-dependent proinflammatory effects of ultrafine polystyrene particles: a role for surface area and oxidative stress in the enhanced activity of ultrafines. *Toxicology and applied pharmacology*, 175(3):191–199, 2001.

[46] Marianne Geiser, Barbara Rothen-Rutishauser, Nadine Kapp, Samuel Schrch, Wolfgang Kreyling, Holger Schulz, Manuela Semmler, Vinzenz Im Hof, Joachim Heyder, and Peter Gehr. Ultrafine particles cross cellular membranes by nonphagocytic mechanisms in lungs and in cultured cells. *Environmental health perspectives*, pages 1555–1560, 2005.

[47] Tobias J. Brunner, Peter Wick, Pius Manser, Philipp Spohn, Robert N. Grass, Ludwig K. Limbach, Arie Bruinink, and Wendelin J. Stark. In Vitro Cytotoxicity of Oxide Nanoparticles: Comparison to Asbestos, Silica, and the Effect of Particle Solubility. *Environmental Science & Technology*, 40(14):4374–4381, July 2006.

[48] Alexander Negoda, Ying Liu, Wen-Che Hou, Charlie Corredor, Babak Yaghoubi Moghadam, Corey Musolff, Lin Li, William Walker, Paul Westerhoff, Andrew J. Mason, Phillip Duxbury, Jonathan D. Posner, and R. Mark Worden. Engineered nanomaterial interactions with bilayer lipid membranes: screening platforms to assess nanoparticle toxicity. *International Journal of Biomedical Nanoscience and Nanotechnology*, 3(1):52–83, January 2013.

[49] Babak Y. Moghadam, Wen-Che Hou, Charlie Corredor, Paul Westerhoff, and Jonathan D. Posner. Role of Nanoparticle Surface Functionality in the Disruption of Model Cell Membranes. *Langmuir*, 28(47):16318–16326, November 2012.

[50] Wen-Che Hou, Babak Yaghoubi Moghadam, Paul Westerhoff, and Jonathan D. Posner. Distribution of Fullerene Nanomaterials between Water and Model Biological Membranes. *Langmuir*, 27(19):11899–11905, September 2011.

[51] Wen-Che Hou, Babak Yaghoubi Moghadam, Charlie Corredor, Paul Westerhoff, and Jonathan D Posner. Distribution of Functionalized Gold Nanoparticles between Water and Lipid Bilayers as Model Cell Membranes. *Environ. Sci. Technol.*, 2012.

[52] Chiu-Wing Lam, John T James, Richard McCluskey, Sivaram Arepalli, and Robert L Hunter. A review of carbon nanotube toxicity and assessment of potential occupational and environmental health risks. *Critical reviews in toxicology*, 36(3):189–217, March 2006.

[53] Min Chen and Anna von Mikecz. Formation of nucleoplasmic protein aggregates impairs nuclear function in response to SiO2 nanoparticles. *Experimental Cell Research*, 305(1):51–62, April 2005.

[54] Eva Oberdrster. Manufactured nanomaterials (fullerenes, C60) induce oxidative stress in the brain of juvenile largemouth bass. *Environmental health perspectives*, 112(10):1058, 2004.

[55] Eva Oberdrster, Shiqian Zhu, T. Michelle Blickley, Patricia McClellan-Green, and Mary L. Haasch. Ecotoxicology of carbon-based engineered nanoparticles: effects of fullerene (C 60) on aquatic organisms. *Carbon*, 44(6):1112–1120, 2006.

[56] Ling Yang and Daniel J. Watts. Particle surface characteristics may play an important role in phytotoxicity of alumina nanoparticles. *Toxicology Letters*, 158(2):122–132, 2005.

[57] Sarah B. Lovern and Rebecca Klaper. Daphnia magna mortality when exposed to titanium dioxide and fullerene (C60) nanoparticles. *Environmental Toxicology and Chemistry*, 25(4):1132–1137, 2006.

[58] Rebecca Bullard-Dillard, Kim E. Creek, Walter A. Scrivens, and James M. Tour. Tissue sites of uptake of 14 C-labeled C 60. *Bioorganic Chemistry*, 24(4):376–385, 1996.

[59] Amane Shiohara, Akiyoshi Hoshino, Ken-ichi Hanaki, Kazuo Suzuki, and Kenji Yamamoto. On the Cyto-Toxicity Caused by Quantum Dots. *Microbiology and immunology*, 48(9):669–675, 2004.

[60] Ron Hardman. A toxicologic review of quantum dots: toxicity depends on physicochemical and environmental factors. *Environmental health perspectives*, pages 165–172, 2006.

[61] Annette M Koch, Fred Reynolds, Hans P Merkle, Ralph Weissleder, and Lee Josephson. Transport of surface-modified nanoparticles through cell monolayers. *Chembiochem: a European journal of chemical biology*, 6(2):337–345, February 2005.

[62] Chandran Krishnaraj, Stacey L Harper, and Soon-Il Yun. In Vivo toxicological assessment of biologically synthesized silver nanoparticles in adult Zebrafish (Danio rerio). *Journal of Hazardous Materials*, 2015.

[63] Benny Lyvn, Martin Hassellv, David R. Turner, Conny Haraldsson, and Karen Andersson. Competition between iron-and carbon-based colloidal carriers for trace metals in a freshwater assessed using flow field-flow fractionation coupled to ICPMS. *Geochimica et Cosmochimica Acta*, 67(20):3791–3802, 2003.

[64] Cristina Lamelas and Vera I. Slaveykova. Comparison of Cd (II), Cu (II), and Pb (II) biouptake by green algae in the presence of humic acid. *Environmental science & technology*, 41(11):4172–4178, 2007.

[65] Xuezhi Zhang, Hongwen Sun, Zhiyan Zhang, Qian Niu, Yongsheng Chen, and John C. Crittenden. Enhanced bioaccumulation of cadmium in carp in the presence of titanium dioxide nanoparticles. *Chemosphere*, 67(1):160–166, 2007.

[66] Anna Lesniak, Federico Fenaroli, Marco P. Monopoli, Christoffer berg, Kenneth A. Dawson, and Anna Salvati. Effects of the Presence or Absence of a Protein Corona on Silica Nanoparticle Uptake and Impact on Cells. *ACS Nano*, 6(7):5845–5857, July 2012.

[67] Juan A. Varela, Mariana G. Bexiga, Christoffer berg, Jeremy C. Simpson, and Kenneth A. Dawson. Quantifying size-dependent interactions between fluorescently labeled polystyrene nanoparticles and mammalian cells. *Journal of Nanobiotechnology*, 10(1):39, September 2012.

[68] Kungang Li, Ying Chen, Wen Zhang, Zhichao Pu, Lin Jiang, and Yongsheng Chen. Surface Interactions Affect the Toxicity of Engineered Metal Oxide Nanoparticles toward Paramecium. *Chemical Research in Toxicology*, 25(8):1675–1681, August 2012.

[69] Na Gou, Annalisa Onnis-Hayden, and April Z. Gu. Mechanistic Toxicity Assessment of Nanomaterials by Whole-Cell-Array Stress Genes Expression Analysis. *Environmental Science & Technology*, 44(15):5964–5970, August 2010.

[70] Tian Xia, Michael Kovochich, Jonathan Brant, Matt Hotze, Joan Sempf, Terry Oberley, Constantinos Sioutas, Joanne I Yeh, Mark R Wiesner, and Andre E Nel. Comparison of the abilities of ambient and manufactured nanoparticles to induce cellular toxicity according to an oxidative stress paradigm. *Nano letters*, 6(8):1794–1807, 2006.

[71] Andre E Nel, Wolfgang J Parak, Warren CW Chan, Tian Xia, Mark C Hersam, C Jeffrey Brinker, Jeffrey I Zink, Kent E Pinkerton, Donald R Baer, and Paul S Weiss. Where are we heading in nanotechnology environmental health and safety and materials characterization. *ACS nano*, 9(6):5627–5630, 2015.

[72] Scientific Committee on Emerging and Newly Identified Health Risks. Opinion on the appropriateness of the risk assessment methodology in accordance with the technical guidance documents for new and existing substances for assessing the risks of nanomaterials. *Scientific Committee on Emerging and Newly Identified Health Risks*, 2007.

[73] Denise M. Mitrano, Sylvie Motellier, Simon Clavaguera, and Bernd Nowack. Review of nanomaterial aging and transformations through the life cycle of nano-enhanced products. *Environment international*, 77:132–147, 2015.

[74] Paul Borm, Frederick C. Klaessig, Timothy D. Landry, Brij Moudgil, Jrgen Pauluhn, Karluss Thomas, Remi Trottier, and Stewart Wood. Research strategies for safety evaluation of nanomaterials, part V: role of dissolution in biological fate and effects of nanoscale particles. *Toxicological Sciences*, 90(1):23–32, 2006.

[75] Kevin W. Powers, Scott C. Brown, Vijay B. Krishna, Scott C. Wasdo, Brij M. Moudgil, and Stephen M. Roberts. Research strategies for safety evaluation of nanomaterials. Part VI. Characterization of nanoscale particles for toxicological evaluation. *Toxicological Sciences*, 90(2):296–303, 2006.

[76] Jingkun Jiang, Gnter Oberdrster, Alison Elder, Robert Gelein, Pamela Mercer, and Professor Pratim Biswas. Does nanoparticle activity depend upon size and crystal phase. *Nanotoxicology*, 2(1):33–42, January 2008.

[77] Wei Liu, Yuan Wu, Chang Wang, Hong C. Li, Thanh Wang, Chun Y. Liao, Lin Cui, Qun F. Zhou, Bing Yan, and Gui B. Jiang. Impact of silver nanoparticles on human cells: Effect of particle size. *Nanotoxicology*, 4(3):319–330, September 2010.

[78] Gregory V. Lowry, Kelvin B. Gregory, Simon C. Apte, and Jamie R. Lead. Transformations of Nanomaterials in the Environment. *Environmental Science & Technology*, 46(13):6893–6899, July 2012.

[79] Clment Levard, E. Matt Hotze, Gregory V. Lowry, and Gordon E. Brown. Environmental Transformations of Silver Nanoparticles: Impact on Stability and Toxicity. *Environmental Science & Technology*, 46(13):6900–6914, July 2012.

[80] Yang Zhang, Yongsheng Chen, Paul Westerhoff, Kiril Hristovski, and John C. Crittenden. Stability of commercial metal oxide nanoparticles in water. *Water Research*, 42(8-9):2204–2212, April 2008.

[81] Kyle Doudrick, Pierre Herckes, and Paul Westerhoff. Detection of Carbon Nanotubes in Environmental Matrices Using Programmed Thermal Analysis. *Environmental Science & Technology*, 46(22):12246–12253, November 2012.

[82] Desire L. Plata, Christopher M. Reddy, and Philip M. Gschwend. Thermogravimetry-Mass Spectrometry for Carbon Nanotube Detection in Complex Mixtures. *Environmental Science & Technology*, 46(22):12254–12261, November 2012.

[83] Ce Gao, David Weisman, Na Gou, Valentine Ilyin, and April Z. Gu. Analyzing High Dimensional Toxicogenomic Data Using Consensus Clustering. *Environmental Science & Technology*, 46(15):8413–8421, August 2012.

[84] Bernd Nowack, Mohamed Baalousha, Nikolaus Bornhft, Qasim Chaudhry, Geert Cornelis, Jane Cotterill, Andreas Gondikas, Martin Hassellv, Jamie Lead, Denise M. Mitrano, and others. Progress towards the validation of modeled environmental concentrations of engineered nanomaterials by analytical measurements. *Environmental Science: Nano*, 2015.

[85] Dion MAM Luykx, Ruud JB Peters, Saskia M. van Ruth, and Hans Bouwmeester. A review of analytical methods for the identification and characterization of nano delivery systems in food. *Journal of agricultural and food chemistry*, 56(18):8231–8247, 2008.

[86] Ana Lpez-Serrano, Riansares Muoz Olivas, Jon Sanz Landaluze, and Carmen Cmara. Nanoparticles: a global vision. Characterization, separation, and quantification methods. Potential environmental and health impact. *Analytical Methods*, 6(1):38–56, 2014.

[87] EFSA Scientific Committee and others. Guidance on the risk assessment of the application of nanoscience and nanotechnologies in the food and feed chain. *EFSA Journal*, 9(5):2140, 2011.

[88] Andre E. Nel, Lutz Mdler, Darrell Velegol, Tian Xia, Eric M. V. Hoek, Ponisseril Somasundaran, Fred Klaessig, Vince Castranova, and Mike Thompson. Understanding biophysicochemical interactions at the nano-bio interface. *Nature Materials*, 8(7):543–557, June 2009.

[89] Yan Yan, Georgina K. Such, Angus P. R. Johnston, James P. Best, and Frank Caruso. Engineering Particles for Therapeutic Delivery: Prospects and Challenges. *ACS Nano*, 2012.

[90] Junhua Yu, Sandeep 4;A. Patel, and Robert 4;M. Dickson. In 4;Vitro and Intracellular Production of Peptide-Encapsulated Fluorescent Silver Nanoclusters. *Angewandte Chemie. International Edition*, 46(12):2028–2030, March 2007.

[91] Kostas Kostarelos, Lara Lacerda, Giorgia Pastorin, Wei Wu, WieckowskiSebastien, Jacqueline Luangsivilay, Sylvie Godefroy, Davide Pantarotto, Jean-Paul Briand, Sylviane Muller, Maurizio Prato, and Alberto Bianco. Cellular uptake of functionalized carbon nanotubes is independent of functional group and cell type. *Nat Nano*, 2(2):108–113, February 2007.

[92] Pascale R. Leroueil, Stephanie A. Berry, Kristen Duthie, Gang Han, Vincent M. Rotello, Daniel Q. McNerny, Baker, Bradford G. Orr, and Mark M. Banaszak Holl. Wide Varieties of Cationic Nanoparticles Induce Defects in Supported Lipid Bilayers. *Nano Letters*, 8(2):420–424, February 2008.

[93] Catherine M. Goodman, Catherine D. McCusker, Tuna Yilmaz, and Vincent M. Rotello. Toxicity of Gold Nanoparticles Functionalized with Cationic and Anionic Side Chains. *Bioconjugate Chem.*, 15(4):897–900, 2004.

[94] Production and applications of carbon nanotubes, carbon nanofibers, fullerenes, graphene, and nanodiamonds: A global technology survey and market analysis. Technical Report et-113, Innovative Research and Products, Inc, February 2011.

[95] Nastassja Lewinski, Vicki Colvin, and Rebekah Drezek. Cytotoxicity of Nanoparticles. *Small*, 4(1):26–49, January 2008.

[96] Anna Shvedova, Vincent Castranova, Elena Kisin, Diane Schwegler-Berry, Ashley Murray, Vadim Gandelsman, Andrew Maynard, and Paul Baron. Exposure to Carbon Nanotube Material: Assessment of Nanotube Cytotoxicity using Human Keratinocyte Cells. *Journal of Toxicology and Environmental Health, Part A*, 66(20):1909–1926, 2003.

[97] Alexandra E. Porter, Mhairi Gass, Karin Muller, Jeremy N. Skepper, Paul A. Midgley, and Mark Welland. Direct imaging of single-walled carbon nanotubes in cells. *Nature Nanotechnology*, 2(11):713–717, October 2007.

[98] S.H. De Paoli Lacerda, J. Semberova, K. Holada, O. Simakova, S.D. Hudson, and J. Simak. Carbon Nanotubes Activate Store-Operated Calcium Entry (SOCE) in Human Blood Platelets. *ACS nano*, 2011.

[99] Jana Semberova, Silvia H. De Paoli Lacerda, Olga Simakova, Karel Holada, Monique P. Gelderman, and Jan Simak. Carbon Nanotubes Activate Blood Platelets by Inducing Extracellular Ca2+ Influx Sensitive to Calcium Entry Inhibitors. *Nano Letters*, 9(9):3312–3317, September 2009.

[100] S. Kang, M.S. Mauter, and M. Elimelech. Microbial cytotoxicity of carbon-based nanomaterials: implications for river water and wastewater effluent. *Environmental science & technology*, 43(7):2648–2653, 2009.

[101] Xinghua Shi, Annette von dem Bussche, Robert H. Hurt, Agnes B. Kane, and Huajian Gao. Cell entry of one-dimensional nanomaterials occurs by tip recognition and rotation. *Nature Nanotechnology*, 6(11):714–719, 2011.

[102] Luca Monticelli, Emppu Salonen, Pu Chun Ke, and Ilpo Vattulainen. Effects of carbon nanoparticles on lipid membranes: a molecular simulation perspective. *Soft Matter*, 5(22):4433, 2009.

[103] Carlos F. Lopez, Steve O. Nielsen, Preston B. Moore, and Michael L. Klein. Understanding nature's design for a nanosyringe. *Proceedings of the National Academy of Sciences of the United States of America*, 101(13):4431 –4434, March 2004.

[104] Bo Liu, Xiaoyi Li, Baolei Li, Bingqian Xu, and Yuliang Zhao. Carbon Nanotube Based Artificial Water Channel Protein: Membrane Perturbation and Water Transportation. *Nano Letters*, 9(4):1386–1394, April 2009.

[105] G. Hummer, J. C. Rasaiah, and J. P. Noworyta. Water conduction through the hydrophobic channel of a carbon nanotube. *Nature*, 414(6860):188–190, November 2001.

[106] R. Coronado. Recent advances in planar phospholipid bilayer techniques for monitoring ion channels. *Annual review of biophysics and biophysical chemistry*, 15(1):259–277, 1986.

[107] M. Goryll, S. Wilk, G. M. Laws, T. Thornton, S. Goodnick, M. Saraniti, J. Tang, and R. S. Eisenberg. Silicon-based ion channel sensor. *Superlattices and Microstructures*, 34(3):451–457, 2003.

[108] M. Criado and B. U Keller. A membrane fusion strategy for single-channel recordings of membranes usually non-accessible to patch-clamp pipette electrodes. *FEBS letters*, 224(1):172–176, 1987.

[109] Aparna Agarwal, Imants Zudans, Owe Orwar, and Stephen G. Weber. Simultaneous Maximization of Cell Permeabilization and Viability in Single-Cell Electroporation Using an Electrolyte-Filled Capillary. *Analytical Chemistry*, 79(1):161–167, January 2007.

[110] Jiumei Chen, Jessica A. Hessler, Krishna Putchakayala, Brian K. Panama, Damian P. Khan, Seungpyo Hong, Douglas G. Mullen, Stassi C. DiMaggio, Abhigyan Som, Gregory N. Tew, Anatoli N. Lopatin, James R. Baker, Mark M. Banaszak Holl, and Bradford G. Orr. Cationic Nanoparticles Induce Nanoscale Disruption in Living Cell Plasma Membranes. *The Journal of Physical Chemistry B*, 113(32):11179–11185, August 2009.

[111] Sujatha Ramachandran, George L. Kumar, Robert H. Blick, and Daniel W. van der Weide. Current bursts in lipid bilayers initiated by colloidal quantum dots. *Applied Physics Letters*, 86(8):083901, February 2005.

[112] S. A Klein, S. J Wilk, T. J Thornton, and J. D Posner. Formation of nanopores in suspended lipid bilayers using quantum dots. volume 109, page 012022, 2008.

[113] Maurits R. R. de Planque, Sara Aghdaei, Tiina Roose, and Hywel Morgan. Electrophysiological Characterization of Membrane Disruption by Nanoparticles. *ACS Nano*, 5(5):3599–3606, September 2011.

[114] Yubing Wang, Zafar Iqbal, and Somenath Mitra. Rapidly Functionalized, Water-Dispersed Carbon Nanotubes at High Concentration. *J. Am. Chem. Soc.*, 128(1):95–99, 2005.

[115] Xiang Wang, Tian Xia, Susana Addo Ntim, Zhaoxia Ji, Saji George, Huan Meng, Haiyuan Zhang, Vincent Castranova, Somenath Mitra, and Andr E. Nel. Quantitative Techniques for Assessing and Controlling the Dispersion and Biological Effects of Multiwalled Carbon Nanotubes in Mammalian Tissue Culture Cells. *ACS Nano*, 4(12):7241–7252, 2010.

[116] Grazia Sessa, John H. Freer, Giuseppe Colacicco, and Gerald Weissmann. Interaction of a Lytic Polypeptide, Melittin, with Lipid Membrane Systems. *Journal of Biological Chemistry*, 244(13):3575 –3582, July 1969.

[117] M. Pawlak, S. Stankowski, and G. Schwarz. Melittin induced voltage-dependent conductance in DOPC lipid bilayers. *Biochimica et Biophysica Acta (BBA)-Biomembranes*, 1062(1):94–102, 1991.

[118] K. Matsuzaki, S. Yoneyama, and K. Miyajima. Pore formation and translocation of melittin. *Biophysical journal*, 73(2):831–838, 1997.

[119] John T. Edward. Molecular volumes and the Stokes-Einstein equation. *Journal of Chemical Education*, 47(4):261, April 1970.

[120] Robert J Hunter. *Zeta potential in colloid science : principles and applications*. Academic Press, London; New York, 1981.

[121] M. B Bally, M. J Hope, L. D Mayer, T. D Madden, and P. R Cullis. Novel procedures for generating and loading liposomal systems. *Liposomes as drug carriers: Recent trends and progress. Wiley*, pages 841–853, 1988.

[122] M. Montal and P. Mueller. Formation of Bimolecular Membranes from Lipid Monolayers and a Study of their Electrical Properties. *Proceedings of the National Academy of Sciences of the United States of America*, 69(12):3561–3566, December 1972.

[123] Mahendra K. Jain, Alfred Strickholm, Frederick P. White, and E. H. Cordes. Electronic Conduction across a Black Lipid Membrane. *Nature*, 227(5259):705–707, 1970.

[124] M. T. Tosteson and D. C. Tosteson. The sting. Melittin forms channels in lipid bilayers. *Biophysical Journal*, 36(1):109–116, 1981.

[125] Christopher Miller, Edward Moczydlowski, Ramon Latorre, and Marcia Phillips. Charybdotoxin, a protein inhibitor of single Ca2+-activated K+ channels from mammalian skeletal muscle. *Nature*, 313(6000):316–318, January 1985.

[126] Almut Mecke, Istvn J. Majoros, Anil K. Patri, Baker, Mark M. Banaszak Holl, and Bradford G. Orr. Lipid Bilayer Disruption by Polycationic Polymers: The Roles of Size and Chemical Functional Group. *Langmuir*, 21(23):10348–10354, 2005.

[127] Sony Joseph, R. Jay Mashl, Eric Jakobsson, and N. R. Aluru. Electrolytic Transport in Modified Carbon Nanotubes. *Nano Lett.*, 3(10):1399–1403, 2003.

[128] T.A. Hilder, D. Gordon, and S.H. Chung. Synthetic Chloride-Selective Carbon Nanotubes Examined by Using Molecular and Stochastic Dynamics. *Biophysical journal*, 99(6):1734–1742, 2010.

[129] Chang Young Lee, Wonjoon Choi, Jae-Hee Han, and Michael S. Strano. Coherence Resonance in a Single-Walled Carbon Nanotube Ion Channel. *Science*, 329(5997):1320 –1324, 2010.

[130] Wonjoon Choi, Chang Young Lee, Moon-Ho Ham, Steven Shimizu, and Michael S. Strano. Dynamics of Simultaneous, Single Ion Transport through Two Single-Walled Carbon Nanotubes: Observation of a Three-State System. *J. Am. Chem. Soc.*, 133(2):203–205, 2010.

[131] I. Laoufi, M.-C. Saint-Lager, R. Lazzari, J. Jupille, O. Robach, S. Garaude, G. Cabailh, P. Dolle, H. Cruguel, and A. Bailly. Size and Catalytic Activity of Supported Gold Nanoparticles: An in Operando Study during CO Oxidation. *The Journal of Physical Chemistry C*, 115(11):4673–4679, March 2011.

[132] M. Haruta, N. Yamada, T. Kobayashi, and S. Iijima. Gold catalysts prepared by coprecipitation for low-temperature oxidation of hydrogen and of carbon monoxide. *Journal of Catalysis*, 115(2):301–309, February 1989.

[133] Nikhil R. Jana, Tapan K. Sau, and Tarasankar Pal. Growing Small Silver Particle as Redox Catalyst. *The Journal of Physical Chemistry B*, 103(1):115–121, January 1999.

[134] Nikhil R. Jana, Z. L. Wang, and Tarasankar Pal. Redox Catalytic Properties of Palladium Nanoparticles: Surfactant and Electron DonorAcceptor Effects. *Langmuir*, 16(6):2457–2463, March 2000.

[135] Sudip Nath, Snigdhamayee Praharaj, Sudipa Panigrahi, Soumen Basu, and Tarasankar Pal. Photochemical evolution of palladium nanoparticles in Triton X-100 and its application as catalyst for degradation of acridine orange. *Current Science*, 92(6):786–790, 2007.

[136] W. J. Plieth. Electrochemical properties of small clusters of metal atoms and their role in the surface enhanced Raman scattering. *The Journal of Physical Chemistry*, 86(16):3166–3170, August 1982.

[137] Kaushik Mallick, Mike Witcomb, and Mike Scurrell. Silver nanoparticle catalysed redox reaction: An electron relay effect. *Materials Chemistry and Physics*, 97(2-3):283–287, June 2006.

[138] Nicolas Cheval, Nabil Gindy, Clifford Flowkes, and Amir Fahmi. Polyamide 66 microspheres metallised with in situ synthesised gold nanoparticles for a catalytic application. *Nanoscale Research Letters*, 7(1):1–9, December 2012.

[139] P. Ken Gillman. CNS toxicity involving methylene blue: the exemplar for understanding and predicting drug interactions that precipitate serotonin toxicity. *Journal of Psychopharmacology*, 25(3):429–436, March 2011.

[140] Mahadevaiyer Krishnan, Jakub W. Nalaskowski, and Lee M. Cook. Chemical Mechanical Planarization: Slurry Chemistry, Materials, and Mechanisms. *Chemical Reviews*, 110(1):178–204, 2009.

[141] E. Uchaker, Y. Z. Zheng, S. Li, S. L. Candelaria, S. Hu, and G. Z. Cao. Better than crystalline: amorphous vanadium oxide for sodium-ion batteries. *J. Mater. Chem. A*, 2(43):18208–18214, September 2014.

[142] Jerzy Haber. Fifty years of my romance with vanadium oxide catalysts. *Catalysis Today*, 142(3-4):100–113, April 2009.

[143] John D. Jarrell, Brandon Dolly, and Jeffrey R. Morgan. Rapid screening, in vitro study of metal oxide and polymer hybrids as delivery coatings for improved soft-tissue integration of implants. *Journal of Biomedical Materials Research. Part A*, 92(3):1094–1104, March 2010.

[144] Troy Benn, Bridget Cavanagh, Kiril Hristovski, Jonathan D. Posner, and Paul Westerhoff. The Release of Nanosilver from Consumer Products Used in the Home. *Journal of Environment Quality*, 39:1875, 2010.

[145] P B Thapa, F Nakajima, and H Furumai. Characterization of natural organic matter in a shallow eutrophic lake. *Water science and technology: a journal of the International Association on Water Pollution Research*, 46(11-12):465–471, 2002.

[146] S Wenzler-Rttele, M Dettenkofer, E Schmidt-Eisenlohr, A Gregersen, J Schulte-Mnting, and M Tvede. Comparison in a laboratory model between the performance of a urinary closed system bag with double non-return valve and that of a single valve system. *Infection*, 34(4):214–218, August 2006.

[147] N Bahary, R L Leibel, L Joseph, and J M Friedman. Molecular mapping of the mouse db mutation. *Proceedings of the National Academy of Sciences of the United States of America*, 87(21):8642–8646, November 1990.

[148] H Chen, O Charlat, L A Tartaglia, E A Woolf, X Weng, S J Ellis, N D Lakey, J Culpepper, K J Moore, R E Breitbart, G M Duyk, R I Tepper, and J P Morgenstern. Evidence that the diabetes gene encodes the leptin receptor: identification of a mutation in the leptin receptor gene in db/db mice. *Cell*, 84(3):491–495, February 1996.

[149] Lisa A McConnachie, Isaac Mohar, Francesca N Hudson, Carol B Ware, Warren C Ladiges, Carolina Fernandez, Sam Chatterton-Kirchmeier, Collin C White, Robert H Pierce, and Terrance J Kavanagh. Glutamate cysteine ligase modifier subunit deficiency and gender as determinants of acetaminophen-induced hepatotoxicity in mice. *Toxicological sciences: an official journal of the Society of Toxicology*, 99(2):628–636, October 2007.

[150] Evan Uchaker, Meng Gu, Nan Zhou, Yanwei Li, Chongmin Wang, and Guozhong Cao. Enhanced Intercalation Dynamics and Stability of Engineered Micro/Nano-Structured Electrode Materials: Vanadium Oxide Mesocrystals. *Small*, 9(22):3880–3886, November 2013.

[151] Robert B. Reed, James J. Faust, Yu Yang, Kyle Doudrick, David G. Capco, Kiril Hristovski, and Paul Westerhoff. Characterization of Nanomaterials in Metal Colloid-Containing Dietary Supplement Drinks and Assessment of Their Potential Interactions after Ingestion. *ACS Sustainable Chemistry & Engineering*, June 2014.

[152] Hobart Hurd Willard, Lynne Lionel Merritt, and John Aurie Dean. *Instrumental methods of analysis*. Van Nostrand, 1974.

[153] Siladitya Behera. UV-Visible Spectrophotometric Method Development and Validation of Assay of Paracetamol Tablet Formulation. *Journal of Analytical & Bioanalytical Techniques*, 03(06), 2012.

[154] Yulia Galagan and Wei-Fang Su. Reversible photoreduction of methylene blue in acrylate media containing benzyl dimethyl ketal. *Journal of Photochemistry and Photobiology A: Chemistry*, 195(2-3):378–383, April 2008.

[155] Olga Impert, Anna Katafias, Przemysaw Kita, Andrew Mills, Aleksandra Pietkiewicz-Graczyk, and Grzegorz Wrzeszcz. Kinetics and mechanism of a fast leuco-Methylene Blue oxidation by copper(II)halide species in acidic aqueous media. *Dalton Transactions*, 345(3):348–353, January 2003.

[156] Dominik Heger, Jaromir Jirkovsky, and Petr Klan. Aggregation of Methylene Blue in Frozen Aqueous Solutions Studied by Absorption Spectroscopy. *The Journal of Physical Chemistry A*, 109(30):6702–6709, August 2005.

[157] Michael Spiro. Heterogeneous catalysis in solution. Part 17.Kinetics of oxidation reduction reaction catalysed by electron transfer through the solid: an electrochemical treatment. *Journal of the Chemical Society, Faraday Transactions 1: Physical Chemistry in Condensed Phases*, 75(0):1507–1512, January 1979.

[158] Michael Spiro and Paul L. Freund. Colloidal catalysis. Transport versus surface control. *Journal of the Chemical Society, Faraday Transactions 1: Physical Chemistry in Condensed Phases*, 79(7):1649–1658, January 1983.

[159] Yao-Hong Chen and Ulrich Nickel. Superadditive catalysis of homogeneous redox reactions with mixed silver gold colloids. *Journal of the Chemical Society, Faraday Transactions*, 89(14):2479–2485, January 1993.

[160] Paul L. Freund and Michael Spiro. Colloidal catalysis: the effect of sol size and concentration. *The Journal of Physical Chemistry*, 89(7):1074–1077, March 1985.

[161] Wen-Yu Wang and Young Ku. Effect of solution pH on the adsorption and photocatalytic reaction behaviors of dyes using TiO2 and Nafion-coated TiO2. *Colloids and Surfaces A: Physicochemical and Engineering Aspects*, 302(1-3):261–268, July 2007.

[162] Jacqueline Belloni. Metal nanocolloids. *Current Opinion in Colloid & Interface Science*, 1(2):184–196, April 1996.

[163] Arnim Henglein. Small-particle research: physicochemical properties of extremely small colloidal metal and semiconductor particles. *Chemical Reviews*, 89(8):1861–1873, December 1989.

[164] Arnim Henglein. Physicochemical properties of small metal particles in solution: "microelectrode" reactions, chemisorption, composite metal particles, and the atom-to-metal transition. *The Journal of Physical Chemistry*, 97(21):5457–5471, May 1993.

[165] Yang-Chuang Chang and Dong-Hwang Chen. Catalytic reduction of 4-nitrophenol by magnetically recoverable Au nanocatalyst. *Journal of Hazardous Materials*, 165(1-3):664–669, June 2009.

[166] Lei Tang, Xiaoqian Li, Robert C. Cammarata, Cody Friesen, and Karl Sieradzki. Electrochemical Stability of Elemental Metal Nanoparticles. *Journal of the American Chemical Society*, 132(33):11722–11726, August 2010.

[167] Zhong-Jie Jiang, Chun-Yan Liu, and Lu-Wei Sun. Catalytic Properties of Silver Nanoparticles Supported on Silica Spheres. *The Journal of Physical Chemistry B*, 109(5):1730–1735, February 2005.

[168] Uday Pratap Azad, Vellaichamy Ganesan, and Manas Pal. Catalytic reduction of organic dyes at gold nanoparticles impregnated silica materials: influence of functional groups and surfactants. *Journal of Nanoparticle Research*, 13(9):3951–3959, September 2011.

[169] John C. Berg. *An Introduction to Interfaces and Colloids: The Bridge to Nanoscience*. World Scientific, Singapore ; Hackensack, NJ, November 2009.

[170] K. Bergmann and C. T. O'Konski. A Spectroscopic Study of Methylene blue Monomer, Dimer, and Complexes with Montmorillonite. *The Journal of Physical Chemistry*, 67(10):2169–2177, October 1963.

[171] Surojit Pande, Sujit Kumar Ghosh, Sudip Nath, Snigdhamayee Praharaj, Subhra Jana, Sudipa Panigrahi, Soumen Basu, and Tarasankar Pal. Reduction of methylene blue by thiocyanate: Kinetic and thermodynamic aspects. *Journal of Colloid and Interface Science*, 299(1):421–427, July 2006.

[172] Joel N. Schrauben, Rebecca Hayoun, Carolyn N. Valdez, Miles Braten, Lila Fridley, and James M. Mayer. Titanium and Zinc Oxide Nanoparticles Are Proton-Coupled Electron Transfer Agents. *Science*, 336(6086):1298–1301, June 2012.

[173] Patricia A. Holden, Frederick Klaessig, Ronald F. Turco, John H. Priester, Cyren M. Rico, Helena Avila-Arias, Monika Mortimer, Kathleen Pacpaco, and Jorge L. Gardea-Torresdey. Evaluation of Exposure Concentrations Used in Assessing Manufactured Nanomaterial Environmental Hazards: Are They Relevant. *Environmental Science & Technology*, 48(18):10541–10551, 2014.

[174] ICH Harmonized Tripartite Guideline. Q2b validation of analytical procedures: methodology. *Fed. Regist*, 62, 1997.

[175] Alankar Shrivastava and VipinB Gupta. Methods for the determination of limit of detection and limit of quantitation of the analytical methods. *Chronicles of Young Scientists*, 2(1):21, 2011.

[176] Martin Lundqvist, Johannes Stigler, Giuliano Elia, Iseult Lynch, Tommy Cedervall, and Kenneth A. Dawson. Nanoparticle size and surface properties determine the protein corona with possible implications for biological impacts. *Proceedings of the National Academy of Sciences*, 105(38):14265–14270, September 2008.

[177] Fabiano Piccinno, Fadri Gottschalk, Stefan Seeger, and Bernd Nowack. Industrial production quantities and uses of ten engineered nanomaterials in Europe and the world. *Journal of Nanoparticle Research*, 14(9):1–11, August 2012.

[178] Lynn J. Frewer, Willem Norde, Arnout Fischer, and Frans Kampers. *Nanotechnology in the Agri-Food Sector*. John Wiley & Sons, February 2011.

[179] Samuel Luoma. Silver nanotechnologies and the environment : old problems or new challenges, 2008.

[180] Andrea L. Hicks, Leanne M. Gilbertson, Jamila S. Yamani, Thomas L. Theis, and Julie B. Zimmerman. Life Cycle Payback Estimates of Nanosilver Enabled Textiles under Different Silver Loading, Release, And Laundering Scenarios Informed by Literature Review. *Environmental Science & Technology*, 49(13):7529–7542, July 2015.

[181] Sabine A. Blaser, Martin Scheringer, Matthew Macleod, and Konrad Hungerbhler. Estimation of cumulative aquatic exposure and risk due to silver: contribution of nano-functionalized plastics and textiles. *The Science of the Total Environment*, 390(2-3):396–409, February 2008.

[182] Mahadevaiyer Krishnan, Jakub W. Nalaskowski, and Lee M. Cook. Chemical Mechanical Planarization: Slurry Chemistry, Materials, and Mechanisms. *Chemical Reviews*, 110(1):178–204, January 2010.

[183] Parshuram B. Zantye, Ashok Kumar, and A. K. Sikder. Chemical mechanical planarization for microelectronics applications. *Materials Science and Engineering: R: Reports*, 45(36):89–220, October 2004.

[184] David Speed, Paul Westerhoff, Reyes Sierra-Alvarez, Rockford Draper, Paul Pantano, Shyam Aravamudhan, Kai Loon Chen, Kiril Hristovski, Pierre Herckes, Xiangyu Bi, Yu Yang, Chao Zeng, Lila Otero-Gonzalez, Carole Mikoryak, Blake A. Wilson, Karshak Kosaraju, Mubin Tarannum, Steven Crawford, Peng Yi, Xitong Liu, S. V. Babu, Mansour Moinpour, James Ranville, Manuel Montano, Charlie Corredor, Jonathan Posner, and Farhang Shadman. Physical, chemical, and in vitro toxicological characterization of nanoparticles in chemical mechanical planarization suspensions used in the semiconductor industry: towards environmental health and safety assessments. *Environ. Sci.: Nano*, 2(3):227–244, 2015.

[185] L. Geranio, M. Heuberger, and B. Nowack. The Behavior of Silver Nanotextiles during Washing. *Environmental Science & Technology*, 43(21):8113–8118, November 2009.

[186] C. Lorenz, L. Windler, N. von Goetz, R. P. Lehmann, M. Schuppler, K. Hungerbhler, M. Heuberger, and B. Nowack. Characterization of silver release from commercially available functional (nano)textiles. *Chemosphere*, 89(7):817–824, October 2012.

[187] Aleksandra B. Djuriic, Yu Hang Leung, Alan M. C. Ng, Xiao Ying Xu, Patrick K. H. Lee, Natalie Degger, and R. S. S. Wu. Toxicity of Metal Oxide Nanoparticles: Mechanisms, Characterization, and Avoiding Experimental Artefacts. *Small*, 11(1):26–44, January 2015.

[188] Elijah J. Petersen, Theodore B. Henry, Jian Zhao, Robert I. MacCuspie, Teresa L. Kirschling, Marina A. Dobrovolskaia, Vincent Hackley, Baoshan Xing, and Jason C. White. Identification and Avoidance of Potential Artifacts and Misinterpretations in Nanomaterial Ecotoxicity Measurements. *Environmental Science & Technology*, 48(8):4226–4246, April 2014.

[189] Robert B. Thurman, Charles P. Gerba, and Gabriel Bitton. The molecular mechanisms of copper and silver ion disinfection of bacteria and viruses. *Critical Reviews in Environmental Control*, 18(4):295–315, January 1989.

[190] Zhongying Wang, Annette von dem Bussche, Pranita K. Kabadi, Agnes B. Kane, and Robert H. Hurt. Biological and Environmental Transformations of Copper-Based Nanomaterials. *ACS Nano*, 7(10):8715–8727, October 2013.

[191] Wan-Seob Cho, Rodger Duffin, Craig A. Poland, Albert Duschl, Gertie Janneke Oostingh, William MacNee, Mark Bradley, Ian L. Megson, and Ken Donaldson. Differential pro-inflammatory effects of metal oxide nanoparticles and their soluble ions in vitro and in vivo; zinc and copper nanoparticles, but not their ions, recruit eosinophils to the lungs. *Nanotoxicology*, 6(1):22–35, February 2012.

[192] Margit Heinlaan, Angela Ivask, Irina Blinova, Henri-Charles Dubourguier, and Anne Kahru. Toxicity of nanosized and bulk ZnO, CuO and TiO2 to bacteria Vibrio fischeri and crustaceans Daphnia magna and Thamnocephalus platyurus. *Chemosphere*, 71(7):1308–1316, April 2008.

[193] Margit Heinlaan, Anne Kahru, Kaja Kasemets, Brigitte Arbeille, Grard Prensier, and Henri-Charles Dubourguier. Changes in the Daphnia magna midgut upon ingestion of copper oxide nanoparticles: A transmission electron microscopy study. *Water Research*, 45(1):179–190, January 2011.

[194] I. Blinova, A. Ivask, M. Heinlaan, M. Mortimer, and A. Kahru. Ecotoxicity of nanoparticles of CuO and ZnO in natural water. *Environmental Pollution*, 158(1):41–47, January 2010.

[195] Hanna L. Karlsson, Johanna Gustafsson, Pontus Cronholm, and Lennart Mller. Size-dependent toxicity of metal oxide particlesA comparison between nano- and micrometer size. *Toxicology Letters*, 188(2):112–118, July 2009.

[196] Klara Midander, Pontus Cronholm, Hanna L. Karlsson, Karine Elihn, Lennart Mller, Christofer Leygraf, and Inger Odnevall Wallinder. Surface characteristics, copper release, and toxicity of nano- and micrometer-sized copper and copper(II) oxide particles: a cross-disciplinary study. *Small (Weinheim an Der Bergstrasse, Germany)*, 5(3):389–399, March 2009.

[197] W. Zhang, S. H. Brongersma, Z. Li, D. Li, O. Richard, and K. Maex. Analysis of the size effect in electroplated fine copper wires and a realistic assessment to model copper resistivity. *Journal of Applied Physics*, 101(6):063703, March 2007.

[198] Kai Zhang, J. R. Weertman, and J. A. Eastman. The influence of time, temperature, and grain size on indentation creep in high-purity nanocrystalline and ultrafine grain copper. *Applied Physics Letters*, 85(22):5197–5199, November 2004.

[199] Antony Ananth, Subramanian Dharaneedharan, Moon-Soo Heo, and Young Sun Mok. Copper oxide nanomaterials: Synthesis, characterization and structure-specific antibacterial performance. *Chemical Engineering Journal*, 262:179–188, February 2015.

[200] Franois Perreault, Silvia Pedroso Melegari, Cristina Henning da Costa, Ana Letcia de Oliveira Franco Rossetto, Radovan Popovic, and William Gerson Matias. Genotoxic effects of copper oxide nanoparticles in Neuro 2a cell cultures. *Science of The Total Environment*, 441:117–124, December 2012.

[201] Cyril Saison, Franois Perreault, Jean-Christophe Daigle, Claude Fortin, Jrme Claverie, Mario Morin, and Radovan Popovic. Effect of core shell copper oxide nanoparticles on cell culture morphology and photosynthesis (photosystem II energy distribution) in the green alga, Chlamydomonas reinhardtii. *Aquatic Toxicology*, 96(2):109–114, January 2010.

[202] Franois Perreault, Abdallah Oukarroum, Silvia Pedroso Melegari, William Gerson Matias, and Radovan Popovic. Polymer coating of copper oxide nanoparticles increases nanoparticles uptake and toxicity in the green alga Chlamydomonas reinhardtii. *Chemosphere*, 87(11):1388–1394, June 2012.

[203] Yong-Wook Baek and Youn-Joo An. Microbial toxicity of metal oxide nanoparticles (CuO, NiO, ZnO, and Sb2o3) to Escherichia coli, Bacillus subtilis, and Streptococcus aureus. *Science of The Total Environment*, 409(8):1603–1608, March 2011.

[204] S. J. Stohs and D. Bagchi. Oxidative mechanisms in the toxicity of metal ions. *Free Radical Biology and Medicine*, 18(2):321–336, February 1995.

[205] N. Ercal, H. Gurer-Orhan, and N. Aykin-Burns. Toxic Metals and Oxidative Stress Part I: Mechanisms Involved in Metal-induced Oxidative Damage. *Current Topics in Medicinal Chemistry*, 1(6):529–539, December 2001.

[206] Inmaculada Yruela. Copper in plants. *Brazilian Journal of Plant Physiology*, 17(1):145–156, March 2005.

[207] Olesja Bondarenko, Katre Juganson, Angela Ivask, Kaja Kasemets, Monika Mortimer, and Anne Kahru. Toxicity of Ag, CuO and ZnO nanoparticles to selected environmentally relevant test organisms and mammalian cells in vitro: a critical review. *Archives of Toxicology*, 87(7):1181–1200, June 2013.

[208] Hanna L. Karlsson, Pontus Cronholm, Yolanda Hedberg, Malin Tornberg, Laura De Battice, Sofia Svedhem, and Inger Odnevall Wallinder. Cell membrane damage and protein interaction induced by copper containing nanoparticles Importance of the metal release process. *Toxicology*, 313(1):59–69, November 2013.

[209] Pontus Cronholm, Hanna L. Karlsson, Jonas Hedberg, Troy A. Lowe, Lina Winnberg, Karine Elihn, Inger Odnevall Wallinder, and Lennart Mller. Intracellular uptake and toxicity of Ag and CuO nanoparticles: a comparison between nanoparticles and their corresponding metal ions. *Small (Weinheim an Der Bergstrasse, Germany)*, 9(7):970–982, April 2013.

[210] Jasmina Vidic, Slavica Stankic, Francia Haque, Danica Ciric, Ronan Le Goffic, Aurore Vidy, Jacques Jupille, and Bernard Delmas. Selective antibacterial effects of mixed ZnMgO nanoparticles. *Journal of Nanoparticle Research*, 15(5):1–10, April 2013.

[211] J. F. Xu, W. Ji, Z. X. Shen, S. H. Tang, X. R. Ye, D. Z. Jia, and X. Q. Xin. Preparation and Characterization of CuO Nanocrystals. *Journal of Solid State Chemistry*, 147(2):516–519, November 1999.

[212] Leanne M. Gilbertson, Charlie Corredor, Eva M. Albalghiti, Zachary S. Fishman, Franois Perreault, Jonathan D. Posner, Menachem Elimelech, Lisa D. Pfefferle, and Julie B. Zimmerman. Shape-dependent properties of nano-cupric oxide: Surface reactivity and antimicrobial activity. *ACSnano*, Submitted, November 2015.

[213] Arturo A. Keller, Hongtao Wang, Dongxu Zhou, Hunter S. Lenihan, Gary Cherr, Bradley J. Cardinale, Robert Miller, and Zhaoxia Ji. Stability and Aggregation of Metal Oxide Nanoparticles in Natural Aqueous Matrices. *Environmental Science & Technology*, 44(6):1962–1967, March 2010.

[214] S. Lowell and Joan E. Shields. Langmuir and BET theories. In *Powder Surface Area and Porosity*, pages 14–29. Springer Netherlands, 1984.

[215] Brian J. Kirby and Ernest F. Hasselbrink. Zeta potential of microfluidic substrates: 1. Theory, experimental techniques, and effects on separations. *Electrophoresis*, 25(2):187–202, January 2004.

[216] Patricia A Holden, Joshua P Schimel, and Hilary A Godwin. Five reasons to use bacteria when assessing manufactured nanomaterial environmental hazards and fates. *Current Opinion in Biotechnology*, 27:73–78, June 2014.

[217] Chitrada Kaweeteerawat, Chong Hyun Chang, Kevin R. Roy, Rong Liu, Ruibin Li, Daniel Toso, Heidi Fischer, Angela Ivask, Zhaoxia Ji, Jeffrey I. Zink, Z. Hong Zhou, Guillaume Francois Chanfreau, Donatello Telesca, Yoram Cohen, Patricia Ann Holden,

Andre E. Nel, and Hilary A. Godwin. Cu Nanoparticles Have Different Impacts in Escherichia coli and Lactobacillus brevis than Their Microsized and Ionic Analogues. *ACS Nano*, 9(7):7215–7225, July 2015.

[218] Dean P. Jones. Redox potential of GSH/GSSG couple: assay and biological significance. *Methods in Enzymology*, 348:93–112, 2002.

[219] Leanne M. Gilbertson, David G. Goodwin, Andr D. Taylor, Lisa Pfefferle, and Julie B. Zimmerman. Toward Tailored Functional Design of Multi-Walled Carbon Nanotubes (MWNTs): Electrochemical and Antimicrobial Activity Enhancement via Oxidation and Selective Reduction. *Environmental Science & Technology*, 48(10):5938–5945, May 2014.

[220] Leanne M. Pasquini, Ryan C. Sekol, Andr D. Taylor, Lisa D. Pfefferle, and Julie B. Zimmerman. Realizing Comparable Oxidative and Cytotoxic Potential of Single- and Multiwalled Carbon Nanotubes through Annealing. *Environmental Science & Technology*, 47(15):8775–8783, August 2013.

[221] Guy Applerot, Jonathan Lellouche, Anat Lipovsky, Yeshayahu Nitzan, Rachel Lubart, Aharon Gedanken, and Ehud Banin. Understanding the antibacterial mechanism of CuO nanoparticles: revealing the route of induced oxidative stress. *Small (Weinheim an Der Bergstrasse, Germany)*, 8(21):3326–3337, November 2012.

[222] Cindy Gunawan, Wey Yang Teoh, Christopher P. Marquis, and Rose Amal. Cytotoxic Origin of Copper(II) Oxide Nanoparticles: Comparative Studies with Micron-Sized Particles, Leachate, and Metal Salts. *ACS Nano*, 5:7214–7225, September 2011.

[223] Johannes Rousk, Kathrin Ackermann, Simon F. Curling, and Davey L. Jones. Comparative Toxicity of Nanoparticulate CuO and ZnO to Soil Bacterial Communities. *PLoS ONE*, 7(3):e34197, March 2012.

[224] M. Hull, A. J. Kennedy, C. Detzel, P. Vikesland, and M. A. Chappell. Moving beyond Mass: The Unmet Need to Consider Dose Metrics in Environmental Nanotoxicology Studies. *Environmental Science & Technology*, 46(20):10881–10882, October 2012.

[225] Joel M. Cohen, Justin G. Teeguarden, and Philip Demokritou. An integrated approach for the in vitro dosimetry of engineered nanomaterials. *Particle and Fibre Toxicology*, 11(1):20, May 2014.

[226] Glen DeLoid, Joel M. Cohen, Tom Darrah, Raymond Derk, Liying Rojanasakul, Georgios Pyrgiotakis, Wendel Wohlleben, and Philip Demokritou. Estimating the effective density of engineered nanomaterials for in vitro dosimetry. *Nature Communications*, 5, March 2014.

[227] Pontus Cronholm, Hanna L. Karlsson, Jonas Hedberg, Troy Lowe, Karine Elihn, Inger Odnevall Wallinder, and Lennart Mller. A Trojan Horse type mechanism: Cellular dose and toxicity of Ag and CuO nanoparticles. *Toxicology Letters*, 211:S201, June 2012.

[228] Nadia von Moos, Paul Bowen, and Vera I. Slaveykova. Bioavailability of inorganic nanoparticles to planktonic bacteria and aquatic microalgae in freshwater. *Environmental Science: Nano*, 1(3):214–232, May 2014.

[229] H. Surangi N. Jayawardena, Kalana W. Jayawardana, Xuan Chen, and Mingdi Yan. Maltoheptaose promotes nanoparticle internalization by Escherichia coli. *Chemical Communications*, 49(29):3034–3036, March 2013.

[230] Mickal Lelimousin and Mark S. P. Sansom. Membrane perturbation by carbon nanotube insertion: pathways to internalization. *Small (Weinheim an Der Bergstrasse, Germany)*, 9(21):3639–3646, November 2013.

[231] Jevgenij A. Kovriznych, Ruzena Sotnikova, Dagmar Zeljenkova, Eva Rollerova, Elena Szabova, and Sona Wimmerova. Acute toxicity of 31 different nanoparticles to zebrafish (Danio rerio) tested in adulthood and in early life stages - comparative study. *Interdisciplinary Toxicology*, 6(2):67–73, June 2013.

[232] Biplab Sarkar, Surya Prakash Netam, Arabinda Mahanty, Ashis Saha, Ranadhir Bosu, and K. K. Krishnani. Toxicity Evaluation of Chemically and Plant Derived Silver Nanoparticles on Zebrafish (Danio rerio). *Proceedings of the National Academy of Sciences, India Section B: Biological Sciences*, pages 1–8, January 2014.

[233] Yang Li, Wen Zhang, Junfeng Niu, and Yongsheng Chen. Mechanism of Photogenerated Reactive Oxygen Species and Correlation with the Antibacterial Properties of Engineered Metal-Oxide Nanoparticles. *ACS Nano*, 6(6):5164–5173, June 2012.

[234] Tomasz Puzyn, Bakhtiyor Rasulev, Agnieszka Gajewicz, Xiaoke Hu, Thabitha P. Dasari, Andrea Michalkova, Huey-Min Hwang, Andrey Toropov, Danuta Leszczynska, and Jerzy Leszczynski. Using nano-QSAR to predict the cytotoxicity of metal oxide nanoparticles. *Nature Nanotechnology*, 6(3):175–178, March 2011.

[235] Mark R. Wiesner, Gregory V. Lowry, Kimberly L. Jones, Jr. Hochella, Michael F., Richard T. Di Giulio, Elizabeth Casman, and Emily S. Bernhardt. Decreasing Uncertainties in Assessing Environmental Exposure, Risk, and Ecological Implications of Nanomaterials. *Environmental Science & Technology*, 43(17):6458–6462, September 2009.

[236] A. E. Nel. Implementation of alternative test strategies for the safety assessment of engineered nanomaterials. *Journal of Internal Medicine*, 274(6):561–577, December 2013.

[237] Charlie Corredor, Mark D. Borysiak, Jay Wolfer, Paul Westerhoff, and Jonathan D. Posner. Colorimetric Detection of Catalytic Reactivity of Nanoparticles in Complex Matrices. *Environmental Science & Technology*, 49(6):3611–3618, March 2015.

[238] Mainak Majumder, Nitin Chopra, and Bruce J. Hinds. Effect of Tip Functionalization on Transport through Vertically Oriented Carbon Nanotube Membranes. *Journal of the American Chemical Society*, 127(25):9062–9070, June 2005.

[239] Mihail Barboiu and Arnaud Gilles. From Natural to Bioassisted and Biomimetic Artificial Water Channel Systems. *Accounts of Chemical Research*, 46(12):2814–2823, December 2013.

[240] Matthew Mancuso, Li Jiang, Ethel Cesarman, and David Erickson. Multiplexed colorimetric detection of kaposi's sarcoma associated herpesvirus and bartonella dna using gold and silver nanoparticles. *Nanoscale*, 5(4):1678–1686, 2013.

[241] Seung Ah Lee and Changhuei Yang. A smartphone-based chip-scale microscope using ambient illumination. *Lab on a Chip*, 14(16):3056–3063, 2014.